UNIVERSITY OF THESSALY

SCHOOL OF ENGINEERING

DEPARTMENT OF MECHANICAL ENGINEERING

Doctor of Philosophy Dissertation

STRUCTURAL BEHAVIOR OF STEEL COMPONENTS UNDER STRONG CYCLIC LOADING

by

GIANNOULA CHATZOPOULOU

Diploma of Civil Engineering, University of Thessaly, 2012

Master of Science (M.Sc.), Department of Mechanical Engineering,

University of Thessaly, 2014

Supervisor: Dr. Spyros A. Karamanos, Professor

Submitted in partial fulfillment

of the requirements for the degree

of Doctor of Philosophy

2019

Approval of this doctoral thesis by the Department of Mechanical Engineering, School of Engineering, University of Thessaly, does not constitute in any way an acceptance of the views of the author by the said academic organization (L.5343/32, art. 202, § 2).

Η έγκριση της διδακτορικής διατριβής από το Τμήμα Μηχανολόγων Μηχανικών της Πολυτεχνικής Σχολής του Πανεπιστημίου Θεσσαλίας δεν υποδηλώνει αποδοχή των απόψεων του συγγραφέα (Ν. 5343/32 αρ. 202 παρ. 2).

Examination Committee:

Dr. Spyros A. Karamanos **(Supervisor)**
Professor, Department of Mechanical Engineering, University of Thessaly

Dr. Antonios E. Giannakopoulos **(Member of Advisory Committee)**
Professor, School of Applied Mathematical and Physical Sciences, National Technical University of Athens

Dr. Kyriakos I. Kourousis **(Member of Advisory Committee)**
Associate Professor, School of Engineering, University of Limerick

Dr. Alexis T. Kermanidis
Associate Professor, Department of Mechanical Engineering, University of Thessaly

Dr. Konstantinos V. Spiliopoulos
Professor, School of Civil Engineering, National Technical University of Athens

Dr. Michalis Agoras
Assistant Professor, Department of Mechanical Engineering, University of Thessaly

Dr. Costas Papadimitriou
Professor, Department of Mechanical Engineering, University of Thessaly

Εξεταστική Επιτροπή:

Δρ. Σπύρος Α. Καραμάνος (**Επιβλέπων**)
Καθηγητής, Τμήμα Μηχανολόγων Μηχανικών, Πανεπιστήμιο Θεσσαλίας

Δρ. Αντώνιος Ε. Γιαννακόπουλος (**Μέλος Τριμελούς Συμβουλευτικής Επιτροπής**)
Καθηγητής, Σχολή Εφαρμοσμένων Μαθηματικών και Φυσικών Επιστημών, Εθνικό Μετσόβιο Πολυτεχνείο

Δρ. Κυριάκος Η. Κουρούσης (**Μέλος Τριμελούς Συμβουλευτικής Επιτροπής**)
Αναπληρωτής Καθηγητής, Πανεπιστήμιο Λιμερικ

Δρ. Αλέξης Θ. Κερμανίδης
Αναπληρωτής Καθηγητής, Τμήμα Μηχανολόγων Μηχανικών, Πανεπιστήμιο Θεσσαλίας

Δρ. Κωνσταντίνος Β. Σπηλιόπουλος
Καθηγητής, Σχολή Πολιτικών Μηχανικών, Εθνικό Μετσόβιο Πολυτεχνείο

Δρ. Μιχάλης Αγόρας
Επίκουρος Καθηγητής, Τμήμα Μηχανολόγων Μηχανικών, Πανεπιστήμιο Θεσσαλίας

Δρ. Κώστας Παπαδημητρίου
Καθηγητής, Τμήμα Μηχανολόγων Μηχανικών, Πανεπιστήμιο Θεσσαλίας

Ευχαριστίες

Πρώτα απ' όλα, θέλω να ευχαριστήσω τον επιβλέποντα της διατριβής μου, Καθηγητή κ. Σπυρίδων Καραμάνο, για την πολύτιμη βοήθεια και καθοδήγησή του κατά τη διάρκεια της διδακτορικής μου διατριβής και την υποστήριξή του όλα τα χρόνια της συνεργασίας μας. Επίσης, θα ήθελα να ευχαριστήσω τα υπόλοιπα μέλη της εξεταστικής επιτροπής της διατριβής μου. Ευχαριστώ την ομάδα του κυρίου Καραμάνου (Γιώργο Βαρέλη, Θεοχάρη Παπαθεοχάρη, Δανιήλ Βασιλική, Πατρίτσια Παππά, Αγλαΐα Πουρνάρα, Μαρία Βάθη, Κωσταντίνο Αντωνίου) για την άριστη συνεργασία μας σε πολλά ερευνητικά θέματα. Ευχαριστώ την κα Άννα Ζερβάκη για την βοήθειά της και την άριστη συνεργασία που είχαμε. Ευχαριστώ τους φίλους(ες) μου για την ηθική υποστήριξή τους. Επίσης, ευχαριστώ τον Γρηγόριο Σαρβάνη για την κατανόησή και την υποστήριξη του όλα τα χρόνια της διατριβής, και ιδιαίτερα κατά τη διάρκεια των τελευταίων μηνών της προσπάθειάς μου. Πάνω απ' όλα, είμαι ευγνώμων στην οικογένειά μου για την ολόψυχη αγάπη και υποστήριξή τους όλα αυτά τα χρόνια. Αφιερώνω αυτή την διατριβή σε όλους όσους ήταν δίπλα μου αυτά τα χρόνια.

Γιαννούλα Χατζοπούλου

STRUCTURAL BEHAVIOR OF STEEL COMPONENTS UNDER STRONG CYCLIC LOADING

GIANNOULA CHATZOPOULOU

Department of Mechanical Engineering, University of Thessaly, 2019

Supervisor: Dr. Spyros A. Karamanos, Professor of Mechanical Engineering

Abstract

This study presents an efficient numerical implementation of the bounding-surface cyclic-plasticity model in a finite element environment, suitable for simulating the structural behavior of metal components subjected to strong cyclic loading. The model is based on the Dafalias-Popov "bounding surface" concept, equipped with appropriate enhancements that allow for efficient simulation of repeated, alternate inelastic deformation. In the first part of the present study, the numerical implementation of the "bounding surface" model is presented. The numerical implementation is performed using an efficient elastic-predictor/plastic-corrector method. Special features of the model are examined, focusing on the influence of several material parameters on cyclic material response. The model is also employed for simulating laboratory physical experiments. First, stress-controlled and strain-controlled small scale experiments are simulated, in strip specimens made of regular (mild) steel and high-strength steel. Upon appropriate calibration from the small-scale tests, the model is employed for predicting the mechanical response of a large-scale physical experiment.

In the second part of the present study, the mechanical behavior of steel pipe bends (elbows), subjected to strong cyclic loading conditions, is presented. The elbows are modeled with finite elements, which account for the measured elbow geometry and for the actual properties of steel elbow material. To simulate material response under repeated inelastic deformation, the cyclic-plasticity material model, discussed in the first part of the study, is employed, based on the bounding-surface concept. Very good

comparison has been obtained in terms of global load-displacement response, as well as in terms of local strains and their accumulation over the loading cycles (ratcheting rate) at specific elbow locations. The good comparison between tests and numerical results indicates that the bounding-surface model can be an efficient tool for predicting accurately the mechanical response of piping components under severe cyclic loading conditions. Using the validated numerical models, extensive results are obtained on the effect of internal pressure on strain and deformation accumulation at different locations of the elbow outer surface, for different values of pipe thickness.

In the third part of the present study, the mechanical behavior of fillet-welded steel joints is examined numerically and experimentally. It is motivated by the seismic response of unanchored steel liquid storage tanks that exhibit repeated uplifting of the base plate, leading to low-cycle fatigue failure of the fillet-welded connection of the tank base plate with the tank shell. Low-cycle fatigue experiments on small-scale fillet-welded joints are performed, representing the connection of the base plate with the tank shell. Material tests have been conducted prior to fatigue tests, to identify the mechanical properties of the base plate material, whereas the weld is examined with stereo optical microscopy and micro-hardness measurements. The fatigue experiments aim at determining the relationship between the strain developed at the welded connection and the corresponding number of cycles to failure. Inspection of the failed specimens determined the "zone" size at the upper and the bottom surface in which microcracks occurred. Numerical simulations are also performed, to elucidate special features of joint behavior, complementing the experimental results and observations. The main conclusion is that the fillet-welded connections under consideration are capable of sustaining a substantial strain levels for a significant number of cycles, before low-cycle fatigue failure occurs. Furthermore, a strain-based fatigue curve is developed, which can be used for the seismic design of liquid storage tanks.

ΔΟΜΙΚΗ ΣΥΜΠΕΡΙΦΟΡΑ ΜΕΤΑΛΛΙΚΩΝ ΜΕΛΩΝ ΥΠΟ ΙΣΧΥΡΗ ΚΥΚΛΙΚΗ ΦΟΡΤΙΣΗ

ΓΙΑΝΝΟΥΛΑ ΧΑΤΖΟΠΟΥΛΟΥ

Πανεπιστήμιο Θεσσαλίας, Τμήμα Μηχανολόγων Μηχανικών, 2019

Επιβλέπων Καθηγητής: Δρ. Σπυρίδων Καραμάνος, Καθηγητής Υπολογιστικών Μεθόδων-Πεπερασμένα Στοιχεία των Κατασκευών

Περίληψη

Στην παρούσα εργασία παρουσιάζεται η αριθμητική ολοκλήρωση ενός καταστατικού μοντέλου κυκλικής πλαστικότητας «οριακής επιφάνειας» σε υπολογιστικό περιβάλλον πεπερασμένων στοιχείων, κατάλληλο για την προσομοίωση της δομικής συμπεριφοράς μεταλλικών στοιχείων, που υπόκεινται σε ισχυρή κυκλική φόρτιση. Το μοντέλο βασίζεται στην ιδέα της "οριακής επιφάνειας" προτεινόμενο από τους Dafalias-Popov, και εμπλουτίζεται με τα κατάλληλα χαρακτηριστικά, ώστε να προσομοιώνεται καλύτερα η ελαστοπλαστική συμπεριφορά του υλικού σε κυκλική φόρτιση. Στο πρώτο τμήμα αυτής της διατριβής παρουσιάζεται το καταστατικό μοντέλο και δίνονται λεπτομέρειες για όλα τα εργαλεία που εισήχθησαν στο μοντέλο ώστε να το ενισχύσουν. Επίσης προσομοιώθηκαν πειράματα μικρής κλίμακας υπο κυκλική φόρτιση, ελέγχοντας την επιβαλλόμενη παραμόρφωση και την τάση. Περαιτέρω, με τη χρήση των πειραμάτων μικρής κλίμακας για τη βαθμονόμηση του καταστατικού μοντέλου προσομοιώθηκαν πειράματα μεγάλης κλίμακας.

Στο δεύτερο μέρος της διατριβής, παρουσιάζεται η μηχανική συμπεριφορά μεταλλικών καμπύλων σωληνωτών στοιχείων (elbows), που υποβάλλονται σε ισχυρή κυκλική φόρτιση. Οι καμπύλοι σωλήνες προσομοιώθηκαν με πεπερασμένα στοιχεία λαμβανομένων υπόψιν της γεωμετρίας και των ιδιοτήτων του υλικού. Για την προσομοίωση χρησιμοποιήθηκε το προτεινόμενο καταστατικό μοντέλο και η σύγκριση των αριθμητικών αποτελεσμάτων με τα πειραματικά δεδομένα είναι πολύ καλή τόσο στο «ολικό» επίπεδο δύναμης-μετατόπισης όσο και στο «τοπικό» επίπεδο που αφορά συσσώρευσή πλαστικών παραμορφώσεων. Με τη χρήση των ίδιων αριθμητικών μοντέλων πραγματοποιήθηκε επιπλέον μια παραμετρική μελέτη για την επιρροή της εσωτερικής

πίεσης και του πάχους του καμπύλου μεταλλικού τμήματος στη συσσώρευση πλαστικών παραμορφώσεων.

Στο τρίτο μέρος της παρούσας διατριβής παρουσιάζεται η μηχανική συμπεριφορά συγκολλητών (fillet-welded) μεταλλικών συνδέσεων. Το κίνητρο αυτής της μελέτης είναι η δομική συμπεριφορά μη αγκυρωμένων μεταλλικών δεξαμενών, οι οποίες υποβάλλονται σε επαναλαμβανόμενο ανασήκωμα της βάσης της δεξαμενής, το οποίο οδηγεί σε ολιγο-κυκλική κόπωση λόγω επαναλαμβανόμενων πλαστικών παραμορφώσεων. Πραγματοποιήθηκαν πειράματα υλικού ώστε να προσδιοριστούν οι ιδιότητές του υλικού και πειράματα σε μεταλλικές συγκολλητές συνδέσεις ώστε να προσδιοριστεί η σχέση των αναπτυσσόμενων παραμορφώσεων κοντά στον πόδα της συγκόλλησης λόγω κυκλικής φόρτισης και του αριθμού των κύκλων μέχρι την αστοχία. Μετά το πέρας των πειραμάτων πραγματοποιήθηκε αυτοψία στα δοκίμια, ώστε να προσδιοριστεί η ζώνη των ρωγμών στην πάνω και την κάτω πλευρά της βάσης του δοκιμίου. Πραγματοποιήθηκαν αριθμητικές προσομοιώσεις με σκοπό τον υπολογισμό παραμορφώσεων σε σημεία όπου πειραματικά δεν ήταν δυνατόν να μετρηθούν, αλλά και για την επέκταση των πειραματικών αποτελεσμάτων. Το βασικό συμπέρασμα της μελέτης των μεταλλικών συνδέσεων είναι ότι μπορούν να υποστούν πολλούς κύκλους με μεγάλες παραμορφώσεις. Τέλος με βάση τα αποτελέσματα προτάθηκε μια καμπύλη κόπωσης, η οποία μπορεί να χρησιμοποιηθεί για τον σεισμικό σχεδιασμό μη αγκυρωμένων δεξαμενών.

Table of Contents

Chapter 1 - Introduction

An efficient numerical implementation of the bounding-surface cyclic-plasticity model in a finite element environment, suitable for simulating the structural behavior of metal components subjected to strong cyclic loading, is presented in the present dissertation. The model is based on the Dafalias-Popov "bounding surface" concept, equipped with appropriate enhancements that allow for efficient simulation of repeated, alternate inelastic deformation. In the first part of the present study, the numerical implementation of the "bounding surface" model is presented. In the second part of the present study, the mechanical behavior of steel pipe bends (elbows), subjected to strong cyclic loading conditions, is presented using the present material model. Finally, in the third part of the present study, using the present material model, the mechanical behavior of fillet-welded steel joints is examined numerically and experimentally.

1.1 Constitutive models for cyclic plasticity

Cyclic plasticity constitutive models have been motivated by the need to describe the mechanical behavior of metals in the inelastic range under repeated loading conditions. Metal components of structural and mechanical systems are often subjected to severe cyclic loading, beyond the elastic regime. As a result, the accurate description of metal cyclic behavior in the inelastic range through simple, efficient and computationally robust cyclic plasticity models is necessary. The earthquake response of structural steel members [1], or the mechanical response of process/power piping systems under seismic or shutdown conditions [2], are typical examples of this type of loading. Furthermore, severe cyclic plastic deformation is also induced in steel pipelines during their installation in deep offshore locations using the reeling method [3][4]. Those repeated excursions into the inelastic range of the metal material could lead to excessive accumulation of plastic deformation and, with the combination of other parameters, such as geometrical imperfections, this may lead to structural failure.

Under repeated loading conditions, the mechanical response of the metal material is well within its inelastic regime and it is characterized by several unique features. A first feature refers to cyclic hardening or softening of the metal material, which may occur under strain-controlled loading conditions. Experimental results have shown that carbon

steels exhibit cyclic softening, whereas cyclic hardening characterizes the cyclic response of stainless steels [5]. Furthermore, when a metal is subjected to non-symmetric stress-controlled cycles (non-zero mean stress), it undergoes progressive increase of strain in the direction of mean strain, a phenomenon often referred to as "ratcheting" [6]. In this case, each hysteresis loop is translated with respect to the previous one because there exists a residual deformation and the stress-strain loop does not close. Structural steels are characterized by the presence of a plastic plateau during initial yielding of the material, followed by the Bauschinger effect upon reverse plastic loading, so that plastic deformation begins at a stress level significantly lower than initial yield, associated with a gradual decrease of the plastic modulus of the material [7]. All the above phenomena need to be accounted for towards reliable prediction of the structural response of steel components.

To describe the mechanical behavior of metal materials under cyclic loading, significant research effort has been devoted in formulating phenomenological plasticity models. The existing literature on this subject is boundless and impossible to cover within this brief introduction. Nevertheless, some notable publications are identified and categorized herein, mainly with respect to the definition of the hardening modulus, which has a paramount effect on cyclic material behavior. In the first category, the hardening modulus is defined indirectly, by imposing the consistency condition on the yield surface, which couples the hardening modulus with the kinematic hardening rule. Those models are often referred to as "coupled models" [6], and may be considered as a direct extension of the classical linear kinematic hardening models [8]. The model introduced by Armstrong and Frederick [9], by adding a non-linear term, referred to as "recovery term", in the evolution equation of the back-stress tensor. Guionnet [10] proposed an enhanced version of the Armstrong-Frederick model [9], where the recovery term is a function of both instantaneous and accumulated inelastic strain, reproducing more accurately the experimental ratcheting rate observed in experiments. In a series of publications, Chaboche and his co-workers [11]-[14] enhanced the nonlinear kinematic hardening rule proposed in [9] considering several superimposed hardening rules, for the purpose of representing cyclic material behavior more accurately. The Ohno-Wang model [15] is also a superposition of several kinematic hardening rules, where each hardening rule is a linear up to critical value. Ohno and Wang [15] had also proposed a slight nonlinearity for each rule at the transition from linear hardening to the stabilized critical state. Hassan and

Rahman [16] and Islam and Hassan [17] discussed the effectiveness of the above models and proposed further advancements for better description of the ratcheting response of pipe elbows. Dafalias *et al.* [18] propose a multiplicative Armstrong and Frederick kinematic hardening model and present comparisons of simulations and experimental data in uniaxial cyclic loading which includes also ratcheting. A modification of the aforementioned model was presented by Agius [19] in order to improve the modeling under uniaxial constant and variable amplitude loading. A useful improvement of the nonlinear kinematic hardening model [9] has been proposed by Ucak and Tsopelas [20][21], accounting for the yield plateau in structural steels upon initial yielding, a concept also followed by Chatzopoulou *et al.* [22] for simulating the cold-forming fabrication process of longitudinally-welded pipes. A model which is capable to describe the yield plateau, the cyclic softening and hardening and the Bauschinger effect is also presented by Hu *et al.* [23], and the calibration of the constitutive model and the simulation of members connections and frames made of structural steels with yield plateau is presented in Hu *et al.* [24]. Moreover, there is a great interest to simulate the ratcheting of straight pipes subjected to internal pressure combined with structural loading. Lee *et al.* in [25] present the comparison of experimental with numerical results and present a constitutive model which adopts combined hardening (isotropic/kinematic), and the kinematic part changes between Chaboche/Burlet and Cailletaud [26] rule. The results are adequately but the transition from elastic part to plastic is not smooth enough in stress strain response. Ohno and Wang model has been used in [27] in order to simulate pressurized pipelines subjected to axial loading. The comparison of the simulation with the experimental results for ratcheting rate in both axial and hoop direction is adequate. Foroutan et al. in [28] has simulated pressurized steel elbow pipes under cyclic bending having used the Ahmadzadeh-Varvani model [29] which is a modified Armstrong & Frederick model.

The multi-surface plasticity model, introduced by Mroz [30] and Iwan [31], is another extension of linear kinematic hardening [8], in an attempt to simulate the Bauschinger effect and the smooth transition from elastic to elastic-plastic behavior of metals under reverse loading. This model consists of several nested yield surfaces, where each surface is activated when contact with its corresponding inner surface is established. An appropriate kinematic hardening rule of the back stress has been proposed in [30], to ensure that the inner surface will always remain inside its outer surface. However, the multi-surface plasticity model may not simulate the ratcheting response of metals.

The second category of cyclic plasticity models comprises the so-called "uncoupled" models [32]. The main feature in those models is the direct definition of the plastic modulus through an appropriate function, so that the plastic modulus is influenced only indirectly by the kinematic hardening rule. Major early contributions in "uncoupled" cyclic plasticity modeling have been reported by Dafalias and Popov [33], and independently by Krieg [34], introducing the concept of "bounding-surface" or "two-surface" plasticity, apparently motivated by the multi-surface plasticity models in [30] and [31]. In this concept, in addition to the yield surface, an outer surface called "bounding surface" is considered, which obeys kinematic hardening and the value of the hardening modulus is a function of the distance between two surfaces. Drucker and Palgen [35] also proposed a cyclic plasticity model in which the plastic modulus is assumed to be a function of the second invariant of the deviatoric stress tensor. Furthermore, Tseng and Lee [36] developed a two-surface model, where the outer surface, referred to as "memory surface", remains always centered at the origin and hardens isotropically every time its stress level is exceeded, representing the biggest state of stress developed throughout the loading history. A uniaxial two-surface model which can treat the cyclic behavior of the structural steels within the yield plateau developed by Shen *et al* [37] and it generalized to a multiaxial two-surface model by Shen *et al* [38]. Hassan and Kyriakides [5] and Hassan *et al.* [39] used the above uncoupled models to show the advantages and disadvantages in the state of the modeling of ratcheting phenomena, and compared with experimental data from uni-axially and bi-axially loaded metal specimens. In subsequent publications, Hassan and Kyriakides [40] [41] have presented enhancement of "uncoupled" models for simulating ratcheting in cyclically hardening and softening materials, under uniaxial and multiaxial loading. The concept of bounding surface models has also been adopted in order to simulate geotechnical problems. Indicatively, Andrianopoulos *et al.* [42], and Papadimitriou *et al.* [43] have used the bounding surface concept in order to investigate geotechnical problems.

The numerical implementation of cyclic-plasticity models in a finite element environment for nonlinear elastic-plastic analysis imposes several challenges. Numerical integration schemes for "coupled" models have been reported in previous publications [44] [45], and relevant integration algorithms have been incorporated in commercial finite element packages [46] [47]. Several attempts have also been reported on the numerical implementation of multi-surface plasticity, as reported by Montans [48]-[50] and Khoei

and Jamali [51]. On the other hand, the numerical implementation of "bounding-surface" models has received much less attention. A relevant numerical work was reported by Varelis [52], who presented an implementation of the Tseng-Lee model [36] in ABAQUS, in the form of a material user-subroutine, for simulating steel tubular members and piping components under several cyclic loading. The major advantage of the uncoupled model compared with the coupled is that because of the explicit definition of the hardening modulus, and with an efficient calibration, an uncoupled model can take into account all the features, appeared when the material is well within its inelastic regime, while the coupled models do not have this advantage.

1.2 The mechanical behavior of metal components

In the present study, two applications are under consideration in order to comprehend the aspects of cyclic plasticity which may appear due to cyclic loading. Each application refers to different phenomena of cyclic plasticity.

The first application refers to the steel pipe elbows (also called pipe "bends"), which are essential components of industrial piping systems in chemical, petrochemical, power plants or energy terminals They can accommodate thermal expansions, and absorb other externally-induced loading, and are considered as critical components for the structural integrity of piping systems. In particular, their performance under strong cyclic loading is of paramount importance for the structural integrity of industrial facilities. Pipe elbows are very flexible with respect to straight pipes of the same cross-section, and their response is characterized by higher stresses and strains at critical locations, a feature associated with cross sectional ovalization. Under strong cyclic loading, elbows may exhibit significant accumulation of plastic strain ("ratcheting"), which may accelerate failure due to plastic collapse or low-cycle fatigue.

The second application examined in the present study refers to fillet-welded plate connections, which constitute a quick and efficient method to tie steel plates and are widely used in civil engineering applications, such as buildings or bridges, as well as in marine structural systems such as stiffeners in ships and other floating systems. In several cases, those welded connections are subjected to repeated loading which may lead to fatigue failure. A specific application of fillet welds refers to unanchored liquid storage tanks and, in particular, to the connection of the tank base plate with the tank shell. When this connection is subjected to strong seismic motion, the overturning moment,

caused mainly, by the oscillating liquid containment, and the relevant hydrodynamic pressure on the tank wall may cause repeated uplift of the tank base plate. Under these strong cyclic loading conditions, the connection of the tank base plate with the tank shell is subjected to cyclic plastic strain.

Both aforementioned applications are of paramount importance for the industry. For this reason, an efficient cyclic plasticity model is vital to describe accurately the mechanical behavior of metals in the inelastic range under repeated loading conditions, and to predict accurately the accumulation of plastic strain ("ratcheting") and the plastic strain with constant amplitude.

1.3 Scope of the present dissertation

The present dissertation aims at developing numerical tools for accurate and efficient simulation of the cyclic inelastic response of metal components. The key feature of this study is the numerical implementation of the "two-surface" model, initially proposed by Dafalias-Popov [33] model, with appropriate enhancement of the hardening function, for improving its ratcheting predictions. The constitutive equations are integrated numerically using a simple and efficient method, outlined in Chapter 2, suitable for implementation in a finite element environment, towards performing structural (large-scale) calculations.

The effectiveness of the numerical model is shown in terms of its predicting capabilities of physical experiments. First, stress-control (ratcheting) and strain-controlled tests for regular and high-strength steels are simulated for the purpose of calibrating the model and defining its parameters. Upon calibration, the model is employed to simulate large-scale tests, in an attempt to demonstrate the numerical efficiency of the material model discussed in Chapter 2 and its capability of predicting the structural response of metal components under severe cyclic loading. It should be noticed that the use of uncoupled plasticity models in predicting the structural response of metal components under strong cyclic loading is novel, given that, almost exclusively, such simulations are performed with coupled models. Therefore, the present study is aimed at offering an efficient simulation tool. Its main characteristic refers to the explicit definition of hardening modulus as a function of the distance between the two surfaces. However, monitoring the relative position of the two surfaces, which obey mixed hardening,

throughout the deformation history, imposes several numerical challenges, which are accounted for in the implementation of the model, also described in Chapter 2.

Two engineering applications are considered in order to show the efficiency and accuracy of the numerical model. The first application is presented in Chapter 3, and refers to the structural response of steel pipe bends, also referred to as elbows, examined experimentally in [53][54]. Those metal components are simulated rigorously using finite elements and the "two-surface" plasticity model, calibrated from small scale strain and stress-controlled tests. The numerical results are compared with experimental data in terms of both global response (force-displacement) and local strains at the critical location, which emphasis on ratcheting. In addition, using the validated models, the effects of internal pressure and pipe-wall thickness on local strain at various locations are examined.

The second application is the low-cycle fatigue of L-shape fillet-welded steel plated joints, presented in Chapter 4, motivated by the seismic response of unanchored (uplifting) liquid storage tank. In the course of the present study, both experimental testing and numerical simulations have been performed on fillet-welded L-joints subjected to strong cyclic loading, representing the uplifting base plate of the tank. Furthermore, small-scale tests have been performed, so that the "two-surface" plasticity model is properly calibrated. The experimental data are compared with numerical results for the purpose of demonstrating the effectiveness of the numerical model.

The main contribution of the present study refers to the efficient numerical implementation of the "two-surface plasticity model" in a user material subroutine (UMAT), accounting for all the features (plastic plateau, Bauschinger effect, ratcheting etc.) appeared when the material is well within its inelastic regime, while the coupled models do not have this advantage. The capabilities of the proposed enhanced model, are demonstrated through the accurate simulation of the accumulation of strains (ratcheting) of steel pipe elbows, subjected to strong cyclic loading and the prediction of the level of strains, induced at a L-joint connection subjected to low cyclic fatigue.

Chapter 2 - Numerical Implementation of Bounding-Surface Model

An efficient numerical implementation of the bounding-surface cyclic-plasticity model in a finite element environment, suitable for simulating the structural behavior of metal components subjected to strong cyclic loading presented in this chapter. The model is based on the Dafalias-Popov "bounding surface" concept, equipped with appropriate enhancements that allow for efficient simulation of repeated, alternate inelastic deformation. The numerical implementation is performed using an efficient elastic-predictor/plastic-corrector method. Special features of the model are examined, focusing on the influence of several material parameters on cyclic material response.

2.1 Description of the cyclic plasticity model

The plasticity model is based on the "bounding surface" or "two-surface" concept, initially proposed by Dafalias and Popov [33], enhanced for the purpose of the present study. The main feature of this model is the outer surface, referred to as "Bounding Surface" and denoted as BS, which plays the role of a bound for the yield surface, denoted as YS (**Figure 1**). Both the yield (inner) surface and the bounding (outer) surface can harden by translating and changing size, obeying a mixed hardening rule under the restriction that the entire yield surface must always remain within the bounding surface. Hardening depends on the distance between the two surfaces, to be defined at a later stage in this section.

During initial plastic loading, the flow rule is controlled by the yield surface. Upon reaching the bounding surface, the two surfaces stay together at the specific stress point, and the flow rule is controlled by the bounding surface. The two surfaces lose contact when reverse plastic loading occurs. The expressions describing the yield surface and the bounding surface are

$$F = \frac{1}{2}(\mathbf{s}-\mathbf{a})\cdot(\mathbf{s}-\mathbf{a}) - \frac{k^2}{3} = 0 \tag{1}$$

$$\bar{F} = \frac{1}{2}(\bar{\mathbf{s}}-\mathbf{b})\cdot(\bar{\mathbf{s}}-\mathbf{b}) - \frac{\bar{k}^2}{3} = 0 \tag{2}$$

respectively, where $\mathbf{s}$ is the deviatoric stress tensor defined as $\mathbf{s}=\boldsymbol{\sigma}-p\mathbf{1}$ ($\boldsymbol{\sigma}$ is the stress tensor, p is the mean stress and $\mathbf{1}$ is the identity second-order tensor), $\bar{\mathbf{s}}$ is the deviatoric stress on the bounding surface, $\mathbf{a}$ and $\mathbf{b}$ are the back-stress tensors associated with the yield and the bounding surface respectively, whereas k and $\bar{k}$ are functions of the equivalent plastic strain ε_q, to be defined below, and define the size of the yield and the bounding surface respectively. Additionally, the radii of the yield and the bounding surface in the deviatoric space, denoted as $\bar{R}$ and R (**Figure 1**), are equal to $\sqrt{2/3}\,\bar{k}$ and $\sqrt{2/3}\,k$ respectively. Furthermore, the following exponential function for k is adopted, which describes the change of the size of the yield surface, due to Bauschinger effect:

$$k=\sigma_y+Q(1-e^{-b\varepsilon_q}) \tag{3}$$

where σ_y is the initial yield stress of the material, and Q and b are material parameters. Without being restrictive, a similar function can be also assumed for the size of the outer surface $\bar{k}$.

The flow rule is expressed by the following equation:

$$\dot{\boldsymbol{\varepsilon}}^p=\frac{1}{H}\left(\mathbf{N}\cdot\dot{\boldsymbol{\sigma}}\right)\mathbf{N} \tag{4}$$

where H is the hardening modulus, $\mathbf{N}$ is a tensor normal to the yield surface,

$$\mathbf{N}=\sqrt{\frac{3}{2}}\frac{1}{|\mathbf{s}-\mathbf{a}|}(\mathbf{s}-\mathbf{a}) \tag{5}$$

and $|\cdot|$ is the Euclidian norm of a tensor. Furthermore, the rate of equivalent plastic strain is defined as follows:

$$\dot{\varepsilon}_q=\sqrt{\frac{2}{3}\dot{\boldsymbol{\varepsilon}}^P\cdot\dot{\boldsymbol{\varepsilon}}^P} \tag{6}$$

whereas the hardening modulus H is defined directly through an appropriate function of the "distance" δ in stress space between points A and B shown in **Figure 1**. Point A represents the current stress state on the yield surface “loading” point, while point B is referred to as the “congruent point” of A, on the bounding surface, which has the same outward normal vector $\mathbf{N}$, as shown in **Figure 1** ($\mathbf{N}=\bar{\mathbf{N}}$). Therefore,

$$\frac{1}{\left|\bar{\mathbf{s}}-\mathbf{b}\right|}\left(\bar{\mathbf{s}}-\mathbf{b}\right)=\frac{1}{\left|\mathbf{s}-\mathbf{a}\right|}\left(\mathbf{s}-\mathbf{a}\right) \tag{7}$$

The following expression for function H has been proposed in [33],

$$H(\delta,\delta_{in})=\bar{H}+h\left(\frac{\delta}{\delta_{in}-\delta}\right) \tag{8}$$

where $\bar{H}$ is the modulus of the bounding surface upon the two surfaces establish contact, h is an important parameter to be discussed extensively in the subsequent sections, δ_{in} is the initial distance between the two surfaces and δ is the current distance between the two surfaces:

$$\delta=\sqrt{\left(\bar{\mathbf{s}}-\mathbf{s}\right)\cdot\left(\bar{\mathbf{s}}-\mathbf{s}\right)} \tag{9}$$

A kinematic hardening rule is adopted for the motion of the yield surface during a plastic loading increment. Among several existing rules, in the present study the rule proposed by Mroz [30] is adopted:

$$\dot{\mathbf{a}}=\dot{\mu}\,\mathbf{v} \tag{10}$$

where $\mathbf{v}$ is a unit tensor ($\mathbf{v}\cdot\mathbf{v}=1$) along the direction of segment AB in the deviatoric stress space, as shown in **Figure 1**:

$$\mathbf{v}=\frac{1}{\left|\bar{\mathbf{s}}-\mathbf{s}\right|}\left(\bar{\mathbf{s}}-\mathbf{s}\right) \tag{11}$$

and $\dot{\mu}$ is a scalar quantity evaluated from the consistency condition at the yield surface.

The translational motion of the bounding surface is coupled with the hardening of the yield surface. There exist two possibilities depending on whether two surfaces are in contact or not, which are examined below. One should keep in mind that the development of plastic deformation is always associated with the motion of both surfaces, independent of whether the two surfaces are in contact or not. This feature of the model affects directly the relative distance between the two surfaces and the value of the hardening modulus, as well as the stage at which contact of the two surfaces occurs, imposing a computational challenge to be discussed in detail in section 2.2.

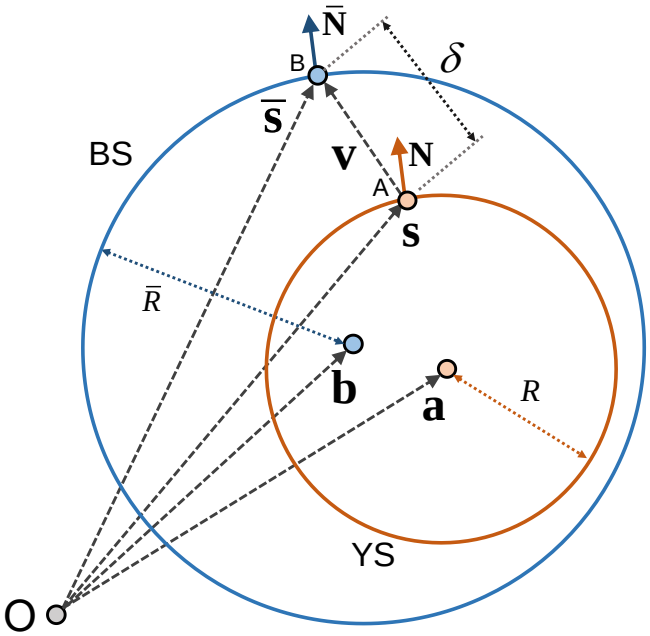

Figure 1. Schematic representation of the two-surface plasticity model in the deviatoric stress plane.

(a) YS and BS are not in contact

In this case, the evolution equation of the back-stress of the bounding surface is

$$\dot{\mathbf{b}} = \dot{\mathbf{a}} - \dot{M}\,\mathbf{v} \tag{12}$$

where $\dot{M}$ is defined by the application of the consistency condition for both yield and bounding surfaces. From eq. (1), the consistency condition gives:

$$\frac{\partial F}{\partial \boldsymbol{\sigma}} \cdot \dot{\boldsymbol{\sigma}} + \frac{\partial F}{\partial \mathbf{a}} \cdot \dot{\mathbf{a}} + \frac{\partial F}{\partial k}\frac{\partial k}{\partial \varepsilon_q}\dot{\varepsilon}_q = 0 \tag{13}$$

Setting $\mathbf{n}$ the unit outward normal tensor to the yield surface and using eq. (4), one readily obtains

$$\dot{\boldsymbol{\sigma}} \cdot \mathbf{n} = \sqrt{\frac{2}{3}} H \dot{\varepsilon}_q \tag{14}$$

Inner multiplication with tensor $\mathbf{v}$, and after some mathematical manipulations, eq. (13) results in

$$\frac{1}{(\mathbf{n}\cdot\mathbf{v})}(\dot{\boldsymbol{\sigma}}\cdot\mathbf{n})\mathbf{v}-\dot{\mathbf{a}}-\sqrt{\frac{2}{3}}\frac{dk}{d\varepsilon_q}\frac{\dot{\varepsilon}_q}{(\mathbf{n}\cdot\mathbf{v})}\mathbf{v}=0 \tag{15}$$

Considering the bounding surface expressed in eq. (2), application of the consistency condition and some mathematical manipulations result in:

$$\frac{1}{(\mathbf{n}\cdot\mathbf{v})}(\dot{\bar{\boldsymbol{\sigma}}}\cdot\mathbf{n})\mathbf{v}-\dot{\mathbf{b}}-\sqrt{\frac{2}{3}}\frac{d\bar{k}}{d\varepsilon_q}\frac{\dot{\varepsilon}_q}{(\mathbf{n}\cdot\mathbf{v})}\mathbf{v}=0 \tag{16}$$

and similar to eq. (14), one readily obtains:

$$\dot{\bar{\boldsymbol{\sigma}}}\cdot\mathbf{n}=\sqrt{\frac{2}{3}}\bar{H}\dot{\varepsilon}_q \tag{17}$$

Combination of eqs. (14) and (17) yields

$$\dot{\bar{\boldsymbol{\sigma}}}\cdot\mathbf{n}=\frac{\bar{H}}{H}(\dot{\boldsymbol{\sigma}}\cdot\mathbf{n}) \tag{18}$$

Furthermore, using eq. (18), eq. (16) can be written in the following form

$$\frac{1}{(\mathbf{n}\cdot\mathbf{v})}\frac{\bar{H}}{H}(\dot{\boldsymbol{\sigma}}\cdot\mathbf{n})\mathbf{v}-\dot{\mathbf{b}}-\sqrt{\frac{2}{3}}\frac{d\bar{k}}{d\varepsilon_q}\frac{\dot{\varepsilon}_q}{(\mathbf{n}\cdot\mathbf{v})}\mathbf{v}=0 \tag{19}$$

and finally, combining eqs. (15) and (19) one obtains

$$\dot{\mathbf{b}}=\dot{\mathbf{a}}-\frac{1}{(\mathbf{n}\cdot\mathbf{v})}(\dot{\boldsymbol{\sigma}}\cdot\mathbf{n})\mathbf{v}+\frac{1}{(\mathbf{n}\cdot\mathbf{v})}\frac{\bar{H}}{H}\dot{\sigma}\mathbf{v}+\sqrt{\frac{2}{3}}\left(\frac{dk}{d\varepsilon_q}\right)\frac{\dot{\varepsilon}_q}{(\mathbf{n}\cdot\mathbf{v})}\mathbf{v}-\sqrt{\frac{2}{3}}\left(\frac{d\bar{k}}{d\varepsilon_q}\right)\frac{\dot{\varepsilon}_q}{(\mathbf{n}\cdot\mathbf{v})}\mathbf{v} \tag{20}$$

From eqs. (20) and (12), one can readily express scalar quantity $\dot{M}$ as follows:

$$\dot{M}=\left[1-\frac{\bar{H}}{H}\right]\frac{(\dot{\boldsymbol{\sigma}}\cdot\mathbf{n})}{(\mathbf{n}\cdot\mathbf{v})}-\sqrt{\frac{2}{3}}\frac{1}{(\mathbf{n}\cdot\mathbf{v})}\left(\frac{dk}{d\varepsilon_q}-\frac{d\bar{k}}{d\varepsilon_q}\right)\dot{\varepsilon}_q \tag{21}$$

(b) YS and BS are in contact

In this case, the evolution of back-stress $\mathbf{b}$ is controlled by the motion of the outer surface

$$\dot{\mathbf{b}} = \dot{\xi}\mathbf{m} \tag{22}$$

where $\mathbf{m}$ is the unit tensor ($\mathbf{m}\cdot\mathbf{m}=1$) normal to the outer surface:

$$\mathbf{m} = \frac{1}{|\bar{\mathbf{s}}-\mathbf{b}|}(\bar{\mathbf{s}}-\mathbf{b}) \tag{23}$$

and $\dot{\xi}$ is a scalar parameter evaluated imposing the consistency condition at the bounding (outer) surface. In this case, $\bar{\mathbf{s}}=\mathbf{s}$ (i.e. the loading point coincides with the congruent point) and the back stress tensor $\mathbf{a}$ can be readily calculated from the following equation, which comes directly from eq. (7):

$$\bar{\mathbf{s}}-\mathbf{b} = \frac{\bar{k}}{k}(\mathbf{s}-\mathbf{a}) \tag{24}$$

Finally, defining $\boldsymbol{\xi}=\mathbf{s}-\mathbf{a}$, the fourth-order elastoplastic rigidity tensor $\mathbf{D}^{ep}$ is written as follows:

$$\mathbf{D}^{ep} = \mathbf{D} - \frac{9G^2}{k^2(H+3G)}(\boldsymbol{\xi}\otimes\boldsymbol{\xi}) \tag{25}$$

where $\otimes$ denotes the fourth-order tensor product of two second-order tensors, and G is the shear modulus.

2.2 Numerical implementation of the constitutive model

The numerical implementation of the model follows an "elastic predictor – plastic corrector" scheme. The incremental problem can be stated as follows: given the stress state, the plastic definition $(\boldsymbol{\sigma}_n, \mathbf{a}_n, \mathbf{b}_n, \varepsilon_{qn})$, the current distance δ_n between the two surfaces, and their initial distance δ_{in} (to be discussed extensively in section 2.3) at stage n, calculate for a given strain increment $\Delta\boldsymbol{\varepsilon}$, the new state parameters $(\boldsymbol{\sigma}_{n+1}, \mathbf{a}_{n+1}, \mathbf{b}_{n+1}, \varepsilon_{qn+1})$, and the new distance δ_{n+1} of the two surfaces at stage $n+1$.

The elastic prediction (trial) stress $\boldsymbol{\sigma}^{(e)}$ is computed first

$$\boldsymbol{\sigma}^{(e)} = \boldsymbol{\sigma}_n + \mathbf{D}\Delta\boldsymbol{\varepsilon} \tag{26}$$

where $\mathbf{D}$ is the fourth-order elastic rigidity tensor. If the deviatoric trial stress tensor $\mathbf{s}^{(e)}$ falls within the yield surface, i.e.

$$F = \frac{1}{2}(\mathbf{s}^{(e)} - \mathbf{a}_n)\cdot(\mathbf{s}^{(e)} - \mathbf{a}_n) - \frac{k^2(\varepsilon_{qn})}{3} \le 0 \tag{27}$$

the elastic stress prediction is valid and the increment is elastic so that the final stress is equal to the trial stress ($\boldsymbol{\sigma}_{n+1} = \boldsymbol{\sigma}^{(e)}$), whereas the other state parameters remain unchanged within this increment ($\mathbf{a}_{n+1} = \mathbf{a}_n$, $\mathbf{b}_{n+1} = \mathbf{b}_n$ and $\varepsilon_{qn+1} = \varepsilon_{qn}$). If not, one should proceed to the plastic-corrector process, described below.

Plastic correction starts with the calculation of factor γ, ($0 \le \gamma \le 1$), defined as the fraction of the total strain increment $\Delta\boldsymbol{\varepsilon}$, so that the yield surface is reached. This strain increment $\gamma\Delta\boldsymbol{\varepsilon}$ is associated with elastic behavior, so that the corresponding stress on the yield surface is

$$\boldsymbol{\sigma}^{YS} = \boldsymbol{\sigma}_n + \mathbf{D}\left(\gamma\Delta\boldsymbol{\varepsilon}\right) \tag{28}$$

Considering that $\mathbf{s}^{YS}$, the deviatoric part of $\boldsymbol{\sigma}^{YS}$, is on the yield surface, the value of γ is readily calculated by inserting eq. (28) into eq. (1):

$$\gamma = \frac{-\left(\boldsymbol{\xi}_n\cdot\Delta\mathbf{s}\right) + \sqrt{\left(\boldsymbol{\xi}_n\cdot\Delta\mathbf{s}\right)^2 + \left(\Delta\mathbf{s}\cdot\Delta\mathbf{s}\right)\cdot\left(\frac{2}{3}k^2 - \left(\boldsymbol{\xi}_n\cdot\boldsymbol{\xi}_n\right)\right)}}{\left(\Delta\mathbf{s}\cdot\Delta\mathbf{s}\right)} \tag{29}$$

where $\boldsymbol{\xi}_n = \mathbf{s}_n - \mathbf{a}_n$ and $\Delta\mathbf{s} = \mathbf{s}^{(e)} - \mathbf{s}_n$. Subsequently the distance between the two surfaces is calculated from $\mathbf{s}^{YS}$ and its congruent point $\bar{\mathbf{s}}_n^{YS}$:

$$\delta = \sqrt{\left[\left(\bar{\mathbf{s}}_n^{YS} - \mathbf{s}_n^{YS}\right)\cdot\left(\bar{\mathbf{s}}_n^{YS} - \mathbf{s}_n^{YS}\right)\right]} \tag{30}$$

Clearly, from eq. (7), $\bar{\mathbf{s}}_n^{YS}$ and $\mathbf{s}^{YS}$ are related as follows:

$$\bar{\mathbf{s}}^{YS} - \mathbf{b}_n = \frac{\bar{k}_n}{k_n}\left(\mathbf{s}^{YS} - \mathbf{a}_n\right) \tag{31}$$

Furthermore, using the value of δ from eq. (30), the value of the hardening modulus H is computed from eq. (8). Subsequently, the remaining part of the strain increment, $\Delta\boldsymbol{\varepsilon}' = \left(1-\gamma\right)\Delta\boldsymbol{\varepsilon}$, is applied in order to complete the increment from $\mathbf{s}^{YS}$ to $\mathbf{s}_{n+1}$. To proceed

with the calculation, it is necessary at this point to identify whether the trial stress state $\mathbf{s}^{(e)}$ falls inside or outside the bounding surface. It is underlined that in the present model when plastic deformation occurs, the outer surface hardens as well, independent of whether it is in contact with the yield surface, and this feature should be taken into account in the numerical implementation.

2.2.1 Case 1: Trial stress state inside the bounding surface

If the trial stress state $\mathbf{s}^{(e)}$ is inside the bounding surface (as shown schematically in **Figure 2**), this is expressed as follows:

$$\bar{F} = \frac{1}{2}(\mathbf{s}^{(e)} - \mathbf{b}_n)\cdot(\mathbf{s}^{(e)} - \mathbf{b}_n) - \frac{\bar{k}^2(\varepsilon_{qn})}{3} \le 0 \tag{32}$$

and implies that the two surfaces will not be in contact in the present increment. In this case, the equations refer to paragraph "YS and BS are not in contact" (section 2.1), and should be considered as follows:

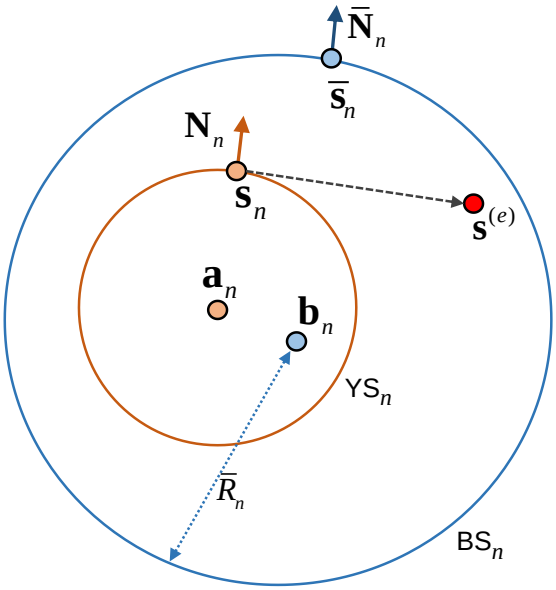

Figure 2. Schematic representation of the two-surface model in the deviatoric stress space for the case of trial stress state $\mathbf{s}^{(e)}$ inside the bounding surface (BS_n)

The final stress can be computed by

$$\mathbf{s}_{n+1} = \mathbf{s}^{(e)} - 2G\,\Delta\boldsymbol{\varepsilon}^p \tag{33}$$

Integrating eq. (4) using an Euler-forward scheme, one obtains

$$\Delta\boldsymbol{\varepsilon}^{p} = \frac{1}{H}\left[\mathbf{N}_{n} \otimes \mathbf{N}_{n}\right]\left(\mathbf{s}_{n+1} - \mathbf{s}^{YS}\right) \tag{34}$$

where in the above equation

$$\mathbf{N}_{n} = \sqrt{\frac{3}{2}}\frac{1}{\left|\mathbf{s}^{YS} - \mathbf{a}_{n}\right|}\left(\mathbf{s}^{YS} - \mathbf{a}_{n}\right) \tag{35}$$

Inserting eq. (34) into eq. (33), one obtains the following expression for the final deviatoric stress $\mathbf{s}_{n+1}$:

$$\mathbf{s}_{n+1} = \mathbf{s}^{(e)} - 2G\frac{1}{H}\left[\mathbf{N}_{n} \otimes \mathbf{N}_{n}\right]\left(\mathbf{s}_{n+1} - \mathbf{s}^{YS}\right) \tag{36}$$

or equivalently

$$\left[\mathbf{I} + 2G\frac{1}{H}\left[\mathbf{N}_{n} \otimes \mathbf{N}_{n}\right]\right]\mathbf{s}_{n+1} = \mathbf{s}^{(e)} + 2G\frac{1}{H}\left[\mathbf{N}_{n} \otimes \mathbf{N}_{n}\right]\mathbf{s}^{YS} \tag{37}$$

where $\mathbf{I}$ is the fourth-order identity tensor.

Therefore, the final stress is calculated as follows:

$$\mathbf{s}_{n+1} = \mathbf{A}^{-1}\,\mathbf{z} \tag{38}$$

where

$$\mathbf{A} = \mathbf{I} + \frac{2G}{H}\left(\mathbf{N}_{n} \otimes \mathbf{N}_{n}\right) \tag{39}$$

and

$$\mathbf{z} = \mathbf{s}^{(e)} + \frac{2G}{H}\left(\mathbf{N}_{n} \otimes \mathbf{N}_{n}\right)\mathbf{s}^{YS} \tag{40}$$

It is possible to obtain the inverse tensor $\mathbf{A}^{-1}$ in a closed form expression which allows for an explicit expression of the final stress in eq. (38). One may write:

$$\mathbf{A} = \mathbf{I} + \mathbf{B} \tag{41}$$

where

$$\mathbf{B} = \frac{2G}{H}\left(\mathbf{N} \otimes \mathbf{N}\right) \tag{42}$$

Equivalently, using the definition of $\mathbf{N}$ in eq. (5), tensor $\mathbf{B}$ can be written as follows

$$\mathbf{B} = \omega\left(\mathbf{n} \otimes \mathbf{n}\right) \tag{43}$$

where $\mathbf{n}$ is the unit tensor outward normal to the yield surface and $\omega = 3G/H$. It is straightforward to show that

$$\mathbf{B}^2 \doteq \mathbf{BB} = \omega\mathbf{B} \tag{44}$$

And, using eq. (44), one can readily verify that

$$\mathbf{A}^{-1} = \mathbf{I} - \frac{1}{1+\omega}\mathbf{B} \tag{45}$$

Using (45), eq. (38) can be written in the following explicit form:

$$\mathbf{s}_{n+1} = \mathbf{s}^{YS} + \left(\mathbf{I} - \frac{1}{1+\omega_n}\mathbf{B}_n\right)\Delta\mathbf{s}_{\Delta\boldsymbol{\varepsilon}'} \tag{46}$$

where $\Delta\mathbf{s}_{\Delta\boldsymbol{\varepsilon}'}$ is the deviatoric part of $\Delta\boldsymbol{\sigma}_{\Delta\varepsilon'}$ and

$$\Delta\boldsymbol{\sigma}_{\Delta\boldsymbol{\varepsilon}'} = \mathbf{D}\Delta\boldsymbol{\varepsilon}' \tag{47}$$

Upon calculation of the final stress at stage $n+1$, the increment of plastic strain is obtained by integrating eq. (6):

$$\Delta\varepsilon_q = \sqrt{\frac{2}{3}\Delta\boldsymbol{\varepsilon}^p \cdot \Delta\boldsymbol{\varepsilon}^p} \tag{48}$$

where $\Delta\boldsymbol{\varepsilon}^p$ is given by eq.(34), and the equivalent plastic strain is updated:

$$\varepsilon_{qn+1} = \varepsilon_{qn} + \Delta\varepsilon_q \tag{49}$$

Furthermore, the back-stress tensor $\mathbf{a}_{n+1}$, defining the position of the yield surface center at stage $n+1$, is obtained by integrating expression (10) with an Euler-forward scheme:

$$\mathbf{a}_{n+1} = \mathbf{a}_n + \Delta\mu\ \mathbf{v}_n \tag{50}$$

where

$$\mathbf{v}_n = \frac{1}{\left|\bar{\mathbf{s}}^{YS} - \mathbf{s}^{YS}\right|}\left(\bar{\mathbf{s}}^{YS} - \mathbf{s}^{YS}\right) \tag{51}$$

In addition, the scalar quantity $\Delta\mu$ is calculated from the consistency condition of the yield surface

$$F = \frac{1}{2}\left(\mathbf{s}_{n+1} - \mathbf{a}_{n+1}\right)\cdot\left(\mathbf{s}_{n+1} - \mathbf{a}_{n+1}\right) - \frac{k_{n+1}^2}{3} = 0 \tag{52}$$

Inserting eq. (50) into eq. (52) one obtains

$$\Delta\mu = \left(\mathbf{s}_{n+1} - \mathbf{a}_n\right)\cdot\mathbf{v}_n - \sqrt{\left[\left(\mathbf{s}_{n+1} - \mathbf{a}_n\right)\cdot\mathbf{v}_n\right]^2 - \left[\left(\mathbf{s}_{n+1} - \mathbf{a}_n\right)\cdot\left(\mathbf{s}_{n+1} - \mathbf{a}_n\right)\right] + \frac{2}{3}k_{n+1}^2} \tag{53}$$

The new back-stress tensor $\mathbf{b}_{n+1}$ of the bounding surface, defining the position of the bounding surface center at stage $n+1$, is obtained by integrating expression (12):

$$\mathbf{b}_{n+1} = \mathbf{b}_n + \Delta\mu\ \mathbf{v}_n - \Delta M\ \mathbf{v}_n \tag{54}$$

where

$$\Delta M = \left(1 - \frac{\bar{H}}{H}\right)\left(\frac{(\mathbf{s}_{n+1} - \mathbf{s}^{YS})\cdot\mathbf{n}^{YS}}{\mathbf{v}_n\cdot\mathbf{n}^{YS}}\right) - \sqrt{\frac{2}{3}}\frac{1}{\left(\mathbf{v}_n\cdot\mathbf{n}^{YS}\right)}\left(\frac{dk}{d\varepsilon_q} - \frac{d\bar{k}}{d\varepsilon_q}\right)\Delta\varepsilon_q \tag{55}$$

Finally, following eq.(7) the stress at the new congruent point $\bar{\mathbf{s}}_{n+1}$ on the bounding surface is computed as follows:

$$\bar{\mathbf{s}}_{n+1} = \mathbf{b}_{n+1} + \frac{\bar{k}_{n+1}}{k_{n+1}}\left(\mathbf{s}_{n+1} - \mathbf{a}_{n+1}\right) \tag{56}$$

and the new distance between the two surfaces in the deviatoric stress space is

$$\delta_{n+1} = \sqrt{\left(\bar{\mathbf{s}}_{n+1} - \mathbf{s}_{n+1}\right)\cdot\left(\bar{\mathbf{s}}_{n+1} - \mathbf{s}_{n+1}\right)} \tag{57}$$

2.2.2 Case 2: Trial stress state outside the bounding surface

If the trial stress state $\mathbf{s}^{(e)}$ falls outside the bounding surface, it may not be possible to conclude a priori whether the two surfaces will establish contact during this increment or not. This depends mainly on the hardening of the outer surface. Therefore, the following procedure is adopted: the calculation starts with the integration process exactly as described in Case 1 above, and a "hypothetical" state of stress at $n+1$ is computed using eq. (38). At the end of this calculation, the following check should be performed:

$$\left|\mathbf{s}_{n+1}-\mathbf{a}_{n+1}\right| < \left|\bar{\mathbf{s}}_{n+1}-\mathbf{a}_{n+1}\right| \tag{58}$$

If the above inequality is satisfied, there is no overlapping of the two surfaces. This implies that the two surfaces remain at a distance during the entire increment and, hence, the calculation process is completed.

On the other hand, if inequality (58) is not satisfied, this means that the two surfaces establish contact during the increment under consideration. In such a case, the increment should be divided in two sub increments, an idea also employed in [48] for the case of "nested" yield surfaces. The main difference of the present formulation with [48] refers to the hardening of the outer surface, which should be accounted for to compute the stage at which the two surfaces get together. More specifically, it is necessary to calculate the value factor ψ, which defines the fraction of the total strain increment necessary for the yield surface to reach the bounding surface. Therefore, the total strain increment $\Delta\boldsymbol{\varepsilon}'$ is divided in two parts: the first part is $\psi\,\Delta\boldsymbol{\varepsilon}'$ until contact of the two surfaces is established (first sub-increment), and $(1-\psi)\Delta\boldsymbol{\varepsilon}'$ is the remaining part, where the two surfaces move together (second sub- increment).

First sub-increment

The deviatoric stress $\mathbf{s}^{con}$, at which contact with the bounding surface is achieved, can be expressed as follows (**Figure 3**).

$$\mathbf{s}^{con} = \mathbf{s}^{YS} + \psi\Delta\mathbf{s}_{\Delta\varepsilon'} - 2G\,\Delta\boldsymbol{\varepsilon}^{p} \tag{59}$$

where $\Delta\mathbf{s}_{\Delta\varepsilon'}$ is the deviatoric part of $\Delta\boldsymbol{\sigma}_{\Delta\varepsilon'}$ given by eq.(47). From the flow rule of eq. (4), eq. (59) is written

$$\mathbf{s}^{con} = \mathbf{s}^{YS} + \psi \Delta \mathbf{s}_{\Delta\varepsilon'} - 2G \frac{1}{H} \left[\mathbf{N}_n \otimes \mathbf{N}_n \right] \left(\mathbf{s}^{con} - \mathbf{s}^{YS} \right) \tag{60}$$

Rearranging, (60) one obtains :

$$\left[\mathbf{I} + 2G \frac{1}{H} \left[\mathbf{N}_n \otimes \mathbf{N}_n \right] \right] \mathbf{s}^{con} = \left[\mathbf{I} + 2G \frac{1}{H} \left[\mathbf{N}_n \otimes \mathbf{N}_n \right] \right] \mathbf{s}^{YS} + \psi \Delta \mathbf{s}_{\Delta\varepsilon'} \tag{61}$$

Setting

$$\mathbf{A} = \mathbf{I} + 2G \frac{1}{H} \left[\mathbf{N}_n \otimes \mathbf{N}_n \right] \tag{62}$$

and

$$\mathbf{x} = \mathbf{A}^{-1} \Delta \mathbf{s}_{\Delta\varepsilon'} \tag{63}$$

the stress $\mathbf{s}^{con}$ at the contact point is expressed as follows

$$\mathbf{s}^{con} = \mathbf{s}^{YS} + \psi \mathbf{x} \tag{64}$$

Equivalently, using eqs. (41)–(45), eq. (64) can be written in the following form:

$$\mathbf{s}^{con} = \mathbf{s}^{YS} + \left(\mathbf{I} - \frac{1}{1 + \omega_n} \mathbf{B}_n \right) \psi \Delta \mathbf{s}_{\Delta\varepsilon'} \tag{65}$$

Therefore, the value of ψ should be determined. Towards this purpose, the flow rule of eq. (4), can be written in the following form:

$$\Delta \boldsymbol{\varepsilon}^p = \frac{1}{H} \psi \left(\mathbf{N}_n \otimes \mathbf{N}_n \right) \mathbf{x} \tag{66}$$

and the equivalent plastic strain, using eq. (48), is expressed as follows:

$$\Delta \varepsilon_q = \frac{1}{H} \psi \sqrt{\frac{2}{3} \left[\left(\mathbf{N_n} \otimes \mathbf{N_n} \right) \mathbf{x} \right] \cdot \left[\left(\mathbf{N_n} \otimes \mathbf{N_n} \right) \mathbf{x} \right]} \tag{67}$$

The back-stress tensor $\mathbf{a}^{con}$, corresponding to the yield surface at the stage where the two surfaces establish contact, is given by integrating eq. (10):

$$\mathbf{a}^{con} = \mathbf{a}_n + \Delta\mu \, \mathbf{v}_n \tag{68}$$

where

$$\mathbf{v}_n = \frac{1}{\left|\bar{\mathbf{s}}^{YS} - \mathbf{s}^{YS}\right|}\left(\bar{\mathbf{s}}^{YS} - \mathbf{s}^{YS}\right) \tag{69}$$

$\bar{\mathbf{s}}^{YS}$ and $\mathbf{s}^{YS}$ are computed by eqs. (28) and (31) respectively, and the scalar quantity $\Delta\mu$ is calculated using the consistency condition at the final stage of the sub-increment:

$$F = \frac{1}{2}\left(\mathbf{s}^{con} - \mathbf{a}^{con}\right)\cdot\left(\mathbf{s}^{con} - \mathbf{a}^{con}\right) - \frac{k_{con}^2}{3} = 0 \tag{70}$$

Inserting eq. (68) into eq. (70) one obtains

$$\Delta\mu = \left(\mathbf{s}^{con} - \mathbf{a}_n\right)\cdot\mathbf{v}_n - \sqrt{\left[\left(\mathbf{s}^{con} - \mathbf{a}_n\right)\cdot\mathbf{v}_n\right]^2 - \left[\left(\mathbf{s}^{con} - \mathbf{a}_n\right)\cdot\left(\mathbf{s}^{con} - \mathbf{a}_n\right)\right] + \frac{2}{3}k_{con}^2} \tag{71}$$

Furthermore, the back-stress tensor $\mathbf{b}^{con}$, which expresses the position of the bounding surface center at the contact point, is given by the following equation:

$$\mathbf{b}^{con} = \mathbf{a}^{con} - \sqrt{\frac{2}{3}}(\bar{k}_{con} - k_{con})\,\mathbf{n}^{con} \tag{72}$$

where

$$\mathbf{n}^{con} = \frac{1}{\left|\mathbf{s}^{con} - \mathbf{a}^{con}\right|}(\mathbf{s}^{con} - \mathbf{a}^{con}) \tag{73}$$

Finally, the value of the unknown parameter ψ can be determined by applying the consistency condition on the bounding surface

$$\bar{F} = \frac{1}{2}\left(\mathbf{s}^{con} - \mathbf{b}^{con}\right)\cdot\left(\mathbf{s}^{con} - \mathbf{b}^{con}\right) - \frac{\bar{k}_{con}^2}{3} = 0 \tag{74}$$

In equation (74), the unknown parameter ψ which is included in tensors $\mathbf{s}^{con}$, $\mathbf{b}^{con}$ and in $\bar{k}_{con}$. Its solution can be performed using iterative (local) Newton – Raphson scheme:

$$\psi_{(i+1)} = \psi_{(i)} - \bar{F}(\psi_{(i)})\left(\frac{d\bar{F}}{d\psi}\right)^{-1}_{\psi=\psi_{(i)}} \tag{75}$$

The expressions for $\bar{F}(\psi)$ and for its derivative $\frac{d\bar{F}}{d\psi}$ are offered in Box 1. Upon computation of ψ, the stress $\mathbf{s}^{con}$ at which contact is established between the yield and the bounding surface can be readily calculated from eq.(65).

Second sub-increment

Upon completion of the first sub-increment, the two surfaces are in contact and for the remaining part of strain increment, which is equal to $(1-\psi)\Delta\boldsymbol{\varepsilon}'$, they move together as shown in **Figure 4**. In this remaining part of the strain increment, the final deviatoric stress $\mathbf{s}_{n+1}$ is given by the following expression:

$$\mathbf{s}_{n+1} = \mathbf{s}^{con} + (1-\psi)\Delta\mathbf{s}_{\Delta\varepsilon'} - 2G\,\frac{1}{H}\left[\mathbf{N}^{con} \otimes \mathbf{N}^{con}\right]\left(\mathbf{s}_{n+1} - \mathbf{s}^{con}\right) \tag{76}$$

Setting

$$\mathbf{A} = \mathbf{I} + 2G\,\frac{1}{H}\left[\mathbf{N}^{con} \otimes \mathbf{N}^{con}\right] \tag{77}$$

and

$$\mathbf{w} = \mathbf{s}^{con} + (1-\psi)\mathbf{s}_{\Delta\varepsilon'} + 2G\,\frac{1}{H}\left[\mathbf{N}^{con} \otimes \mathbf{N}^{con}\right]\mathbf{s}^{con} \tag{78}$$

one readily obtains

$$\mathbf{s}_{n+1} = \mathbf{A}^{-1}\mathbf{w} \tag{79}$$

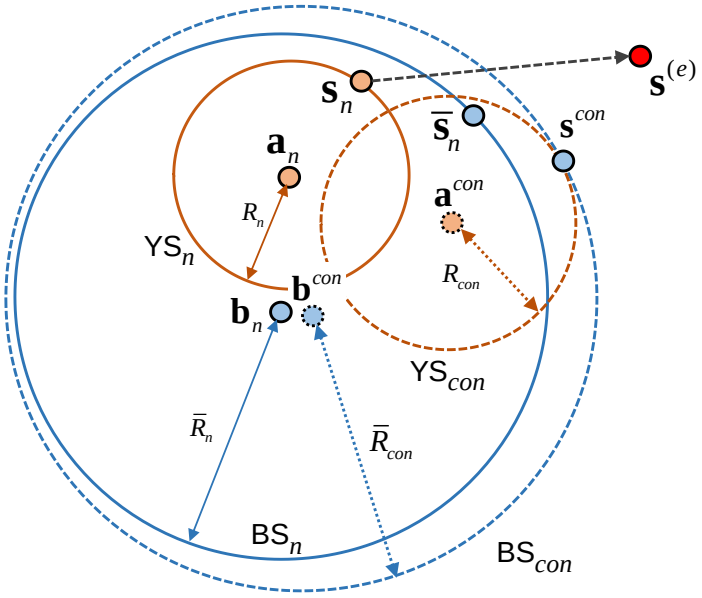

Figure 3. Schematic representation of the two-surface model in the case where the trial stress state falls outside the bounding surface, before the two surfaces get together.

Equivalently, eq. (79) can also be written as follows:

$$\mathbf{s}_{n+1} = \mathbf{s}^{con} + (1-\psi)\left(\mathbf{I} - \frac{1}{1+\omega_{con}}\mathbf{B}_{con}\right)\Delta\mathbf{s}_{\Delta\varepsilon'} \tag{80}$$

Combining eqs.(80) and (65), an explicit expression for the final stress is obtained in terms of the initial stress at plastic loading, for the case where the two surfaces get in contact within the increment under consideration:

$$\mathbf{s}_{n+1} = \mathbf{s}^{YS} + \Delta\mathbf{s}_{\Delta\varepsilon'} + \left(\frac{\psi}{1+\omega_n}\mathbf{B}_n + \frac{1-\psi}{1+\omega_{con}}\mathbf{B}_{con}\right)\Delta\mathbf{s}_{\Delta\varepsilon'} \tag{81}$$

The total increment of equivalent plastic strain $\Delta\varepsilon_q$, from stage n to stage $n+1$, is the sum of the relevant quantities calculated in the two sub- increments: (a) during the first sub- increment, the yield surface reaches the bounding surface and (b) during the second sub- increment, the two surfaces remain in contact and move together.

From eq. (22), the back stress tensor $\mathbf{b}_{n+1}$ of the bounding surface at the final state $n+1$ is calculated from the following equation:

$$\mathbf{b}_{n+1} = \mathbf{b}_n + \Delta\xi\,\mathbf{m}_{n+1} \tag{82}$$

where

$$\mathbf{m}_{n+1} = \frac{1}{\left|\mathbf{s}^{con} - \mathbf{b}^{con}\right|}\left(\mathbf{s}^{con} - \mathbf{b}^{con}\right) \tag{83}$$

and $\Delta\xi$ is calculated by imposing the consistency condition at the bounding surface:

$$\bar{F} = \frac{1}{2}\left(\mathbf{s}_{n+1} - \mathbf{b}_{n+1}\right)\cdot\left(\mathbf{s}_{n+1} - \mathbf{b}_{n+1}\right) - \frac{\bar{k}^2}{3} = 0 \tag{84}$$

In this case, $\bar{\mathbf{s}}_{n+1} = \mathbf{s}_{n+1}$, so that the back stress tensor $\mathbf{a}_{n+1}$ of the yield surface is calculated from the following expression, which comes directly from eq. (7):

$$\mathbf{a}_{n+1} = \mathbf{s}_{n+1} - \frac{k_{n+1}}{\bar{k}_{n+1}}\left(\bar{\mathbf{s}}_{n+1} - \mathbf{b}_{n+1}\right) \tag{85}$$

2.2.3 Elastoplastic rigidity

Defining $\boldsymbol{\xi}_{n+1} = \mathbf{s}_{n+1} - \mathbf{a}_{n+1}$, and using eq.(25), the tangent fourth-order elastoplastic rigidity tensor $\mathbf{D}^{ep}$ is written as follows:

$$\mathbf{D}^{ep} = \mathbf{D} - \frac{9G^2}{k_{n+1}^2\left(H + 3G\right)}\left(\boldsymbol{\xi}_{n+1} \otimes \boldsymbol{\xi}_{n+1}\right) \tag{86}$$

The consistent tangent fourth-order elastoplastic rigidity tensor $\hat{\mathbf{D}}^{ep}$ can be obtained by differentiation of eqs. (46) or (81), depending on whether contact between the yield and the bounding surface has occurred within the increment under consideration or not. For the non-contact case, the final stress $\boldsymbol{\sigma}_{n+1}$ is obtained by adding the hydrostatic part of stress tensor at the end of the increment to the deviatoric part, which expressed in eq. (46):

$$\begin{aligned}\boldsymbol{\sigma}_{n+1} = {} & \lambda\left(\mathbf{1}\otimes\mathbf{1}\right)\Delta\boldsymbol{\varepsilon} + 2G\,\mathbf{I}\Delta\boldsymbol{\varepsilon} + \mathbf{s}^{YS} \\ & - 2G\left(\frac{1}{1+\omega_n}\mathbf{B}_n\right)\left(\Delta\boldsymbol{\varepsilon} - \frac{1}{3}\left(\mathbf{1}\otimes\mathbf{1}\right)\Delta\boldsymbol{\varepsilon}\right)\end{aligned} \tag{87}$$

where λ is the first Lamé constant. Differentiation of (87) gives:

$$\hat{\mathbf{D}}^{ep} = \frac{\partial\boldsymbol{\sigma}_{n+1}}{\partial\Delta\boldsymbol{\varepsilon}} = \mathbf{D} - \left(\frac{2G}{1+\omega_n}\mathbf{B}_n\right) \tag{88}$$

where $\mathbf{B}_n = \omega_n \left(\mathbf{n}_n \otimes \mathbf{n}_n \right)$, or equivalently

$$\hat{\mathbf{D}}^{ep} = \mathbf{D} - \frac{9G^2}{k_n^2 \left(H + 3G \right)} \left(\xi_n \otimes \xi_n \right) \tag{89}$$

For the case where contact of the two surfaces occurs adding the hydrostatic part to the deviatoric final stress in eq. (81) results in

$$\boldsymbol{\sigma}_{n+1} = \lambda \left(\mathbf{1} \otimes \mathbf{1} \right) \Delta\boldsymbol{\varepsilon} + 2G\, \mathbf{I} \Delta\boldsymbol{\varepsilon} + \mathbf{s}^{YS} + \left(\frac{\psi}{1+\omega_n} \mathbf{B}_n + \frac{1-\psi}{1+\omega_{con}} \mathbf{B}_{con} \right) \Delta\boldsymbol{\varepsilon} \tag{90}$$

Differentiation of the above equation gives

$$\hat{\mathbf{D}}^{ep} = \frac{\partial \boldsymbol{\sigma}_{n+1}}{\partial \Delta\boldsymbol{\varepsilon}} = \mathrm{D} - \left(\frac{\psi}{1+\omega_n} \mathbf{B}_n + \frac{1-\psi}{1+\omega_{con}} \mathbf{B}_{con} \right) \tag{91}$$

where $\mathbf{B}_n = \omega_n \left(\mathbf{n}_n \otimes \mathbf{n}_n \right)$ and $\mathbf{B}_{con} = \omega_{con} \left(\mathbf{n}_{con} \otimes \mathbf{n}_{con} \right)$.Eequivalently,

$$\hat{\mathbf{D}}^{ep} = \mathbf{D} - \psi \frac{9G^2}{k_n^2 \left(H + 3G \right)} \left(\xi_n \otimes \xi_n \right) - \left(1 - \psi \right) \frac{9G^2}{k_{con}^2 \left(\bar{H} + 3G \right)} \left(\xi_{con} \otimes \xi_{con} \right) \tag{92}$$

where $\xi_n = \mathbf{s}_n - \mathbf{a}_n$ and $\xi_{con} = \mathbf{s}_{con} - \mathbf{a}_{con}$. A summary of the algorithm is offered in Box 2.

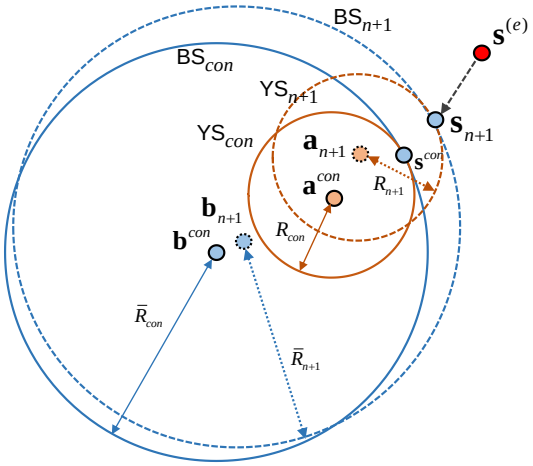

Figure 4. Schematic representation of the two-surface model in the case where the trial stress state falls outside the bounding surface, after the two surfaces establish contact.

Box 1. Equations for $\bar{F}$ and $\frac{d\bar{F}}{d\psi}$ in eq. (74)

(a) Function $\bar{F}$:

$$\bar{F} = C_1\psi + C_2\psi^2 - C_3\psi\Delta\mu + C_4\Delta\mu + C_5\Delta\mu^2 + C_6 = 0$$

$$C_1 = \left(\frac{(2\bar{k}_{con} - k_{con})}{k_{con}} \left(\mathbf{s}^{YS} \cdot \mathbf{x}\right) - \frac{(2\bar{k}_{con} - k_{con})}{k_{con}} \left(\mathbf{x} \cdot \mathbf{a}_n\right) \right)$$

$$C_2 = \left(\frac{(2\bar{k}_{con} - k_{con})}{2k_{con}} \left(\mathbf{x} \cdot \mathbf{x}\right) \right)$$

$$C_3 = \left(\mathbf{x} \cdot \mathbf{v}_n\right) \frac{(2\bar{k}_{con} - k_{con})}{k_{con}}$$

$$C_4 = -\left(\mathbf{s}^{YS} \cdot \mathbf{v}_n\right) \frac{(2\bar{k}_{con} - k_{con})}{k_{con}} + \left(\mathbf{v}_n \cdot \mathbf{a}_n\right) \frac{(2\bar{k}_{con} - k_{con})}{k_{con}}$$

$$C_5 = \frac{(2\bar{k}_{con} - k_{con})}{2k_{con}}$$

$$C_6 = \frac{(2\bar{k}_{con} - k_{con})}{2k_{con}} \left(\left(\mathbf{s}^{YS} \cdot \mathbf{s}^{YS}\right) + \left(\mathbf{a}_n \cdot \mathbf{a}_n\right) \right) - \frac{(2\bar{k}_{con} - k_{con})}{k_{con}} \left(\mathbf{s}^{YS} \cdot \mathbf{a}_n\right) - \frac{1}{3}\bar{k}_{con}\bar{k}_{con} + \frac{1}{3}k_{con}^2$$

where

$$k_{con} = \sigma_y + Q(1 - e^{-b\left(\varepsilon_{qn} + A\psi\right)})$$

$$A = \frac{1}{H}\sqrt{\frac{2}{3}\left[\left(\mathbf{N_n} \otimes \mathbf{N_n}\right)\mathbf{x}\right] \cdot \left[\left(\mathbf{N_n} \otimes \mathbf{N_n}\right)\mathbf{x}\right]}$$

$$\Delta\mu = \left(\left(\mathbf{s}^{YS} - \mathbf{a}_n\right) \cdot \mathbf{v}_n\right) + \psi\left(\mathbf{x} \cdot \mathbf{v}_n\right) - C_7$$

$$C_7 = \sqrt{\left\{\left[\left(\mathbf{s}^{YS} - \mathbf{a}_n\right) \cdot \mathbf{v}_n\right] + \psi\left(\mathbf{x} \cdot \mathbf{v}_n\right)\right\}^2 - \left(\mathbf{s}^{YS} - \mathbf{a}_n\right) \cdot \left(\mathbf{s}^{YS} - \mathbf{a}_n\right) - 2\psi\left[\left(\mathbf{s}^{YS} - \mathbf{a}_n\right) \cdot \mathbf{x}\right] - \psi^2\left(\mathbf{x} \cdot \mathbf{x}\right)^2 + \frac{2k_{con}^2}{3}}$$

(b) Derivative $\frac{d\bar{F}}{d\psi}$:

$$\frac{d\bar{F}}{d\psi} = C_1 + 2C_2\psi - C_3\Delta\mu - C_3\psi\frac{d\Delta\mu}{d\psi} + \frac{d\Delta\mu}{d\psi}C_4 + 2C_5\Delta\mu\frac{d\Delta\mu}{d\psi} + \\ + \frac{dC_6}{d\psi} + \frac{dC_1}{d\psi}\psi + \frac{dC_2}{d\psi}\psi^2 - \frac{dC_3}{d\psi}\psi\Delta\mu + \Delta\mu\frac{dC_4}{d\psi} + \frac{dC_5}{d\psi}\Delta\mu^2$$

$$\frac{dC_1}{d\psi} = 2\frac{\bar{k}'_{con}k_{con} - \bar{k}_{con}k'_{con}}{k^2_{con}}\left(\mathbf{s}^{YS}\cdot\mathbf{x}\right) - 2\frac{\bar{k}'_{con}k_{con} - \bar{k}_{con}k'_{con}}{k^2_{con}}\left(\mathbf{x}\cdot\mathbf{a}_n\right)$$

$$\frac{dC_2}{d\psi} = \frac{\bar{k}'_{con}k_{con} - \bar{k}_{con}k'_{con}}{k^2_{con}}\left(\mathbf{x}\cdot\mathbf{x}\right)$$

$$\frac{dC_3}{d\psi} = 2\left(\mathbf{x}\cdot\mathbf{v}_n\right)\frac{\bar{k}'_{con}k_{con} - \bar{k}_{con}k'_{con}}{k^2_{con}}$$

$$\frac{dC_4}{d\psi} = -2\left(\mathbf{s}^{YS}\cdot\mathbf{v}_n\right)\frac{\bar{k}'_{con}k_{con} - \bar{k}_{con}k'_{con}}{k^2_{con}} + 2\left(\mathbf{v}_n\cdot\mathbf{a}_n\right)\frac{\bar{k}'_{con}k_{con} - \bar{k}_{con}k'_{con}}{k^2_{con}}$$

$$\frac{dC_5}{d\psi} = \frac{\bar{k}'_{con}k_{con} - \bar{k}_{con}k'_{con}}{k^2_{con}}$$

$$\frac{dC_6}{d\psi} = \frac{\bar{k}'_{con}k_{con} - \bar{k}_{con}k'_{con}}{k^2_{con}}\left[\left(\mathbf{s}^{YS}\cdot\mathbf{s}^{YS}\right) - 2\left(\mathbf{s}^{YS}\cdot\mathbf{a}_n\right) + \left(\mathbf{a}_n\cdot\mathbf{a}_n\right)\right] + \\ + \left(-\frac{2}{3}\bar{k}'_{con}k_{con} - \frac{2}{3}\bar{k}_{con}k'_{con} + \frac{2}{3}k_{con}k'_{con}\right)$$

and

$$\frac{d\Delta\mu}{d\psi} = \left(\mathbf{x}\cdot\mathbf{v}_n\right) - \frac{dC_7}{d\psi}$$

$$\frac{dC_7}{d\psi} = \frac{1}{2}\frac{\left\{\left[\left(\mathbf{s}^{YS} - \mathbf{a}_n\right)\cdot\mathbf{v}_n\right] + \psi\left(\mathbf{x}\cdot\mathbf{v}_n\right)\right\}^2\left(\mathbf{x}\cdot\mathbf{v}_n\right) - 2\left[\left(\mathbf{s}^{YS} - \mathbf{a}_n\right)\cdot\mathbf{x}\right] - 2\psi\left(\mathbf{x}\cdot\mathbf{x}\right)^2 + \frac{4}{3}k_{con}k'_{con}}{\sqrt{C_7}}$$

$$k'_{con} = \frac{dk_{con}}{d\psi} = QbA(e^{-b\varepsilon_{qn}}e^{-bA\psi})$$

Box 2. Integration algorithm of the constitutive model

Material parameters: E, σ_y, Q, b, $\bar{H}$, a, d, n, m, σ_b, Q_b, b_b, c.

Input at stage n: $\boldsymbol{\sigma}_n, \mathbf{a}_n, \mathbf{b}_n, \varepsilon_{qn}, \delta_n$, δ_{in}, and $\Delta\boldsymbol{\varepsilon}$.

1: compute the trial stress state $\boldsymbol{\sigma}^{(e)}$ from eqs.(26) and (27).

2: check $\boldsymbol{\sigma}^{(e)}$ for yielding:

- if yes, the elastic prediction is valid, update $\boldsymbol{\sigma}_{n+1} = \boldsymbol{\sigma}^{(e)}$, **EXIT**
- if no, GOTO 3.

3: calculate:

γ [eq.(29)], δ [eq.(30)],

check if δ_{in} needs update:

for the 1st plastic loading increment $\mathbf{n}_{in} = \mathbf{n}^{YS}$ and $\delta_{in} = \delta$

for the subsequent increments Check :

if $\mathbf{n}_{in} \cdot \mathbf{n}^{YS} > 0 \rightarrow \mathbf{n}_{in} = \mathbf{n}_{in}$ and $\delta_{in} = \delta_{in}$

if $\mathbf{n}_{in} \cdot \mathbf{n}^{YS} < 0 \rightarrow \mathbf{n}_{in} = \mathbf{n}^{YS}$ and $\delta_{in} = \delta$

then calculate: $H(\delta, \delta_{in})$ [eq (8)]; $\mathbf{s}^{YS}$ [eq.(28)] $\bar{\mathbf{s}}^{YS}$ and [eq.(31)];

$\mathbf{N}_n$ [eq.(35)], $\Delta\boldsymbol{\sigma}_{\Delta\boldsymbol{\varepsilon}'}$ [eq.(47)], $\mathbf{B}$ [eq.(42)], $\boldsymbol{\nu}_n$ [eq.(51)].

4: calculate:

$\mathbf{s}_{n+1}$[eq.(46)], $\Delta\boldsymbol{\varepsilon}^p$ [eq.(34)], $\Delta\varepsilon_q$ [eq.(48)] and update $\varepsilon_{qn+1} = \varepsilon_{qn} + \Delta\varepsilon_q$.

Then calculate:

$\Delta\mu$ [eq.(53)], $\mathbf{a}_{n+1}$ [eq.(50)], ΔM [eq.(55)], $\mathbf{b}_{n+1}$[eq.(54)]

$\bar{\mathbf{s}}_{n+1}$ [eq.(56)]

5: examine whether trial stress $\boldsymbol{\sigma}^{(e)}$ falls inside or outside the bounding surface from inequality eq (32)

- if trial stress state $\boldsymbol{\sigma}^{(e)}$ is inside the bounding surface, GOTO 8
- if trial stress state is outside the bounding surface, check eq. (58),
  - if eq. (58) is satisfied, GOTO 8
  - else two sub-increments are necessary, proceed to 6

6: First sub-increment

calculate:

$\mathbf{A}$ [eq.(62)]; $\mathbf{x}$ [eq.(63)];

calculate ψ [solution of eq. (74), see Box 1]

calculate:

$\mathbf{s}^{con}$ [eq.(64) or eq.(65)]; $\Delta\boldsymbol{\varepsilon}^{p}$ [eq.(66)]; $\Delta\varepsilon_{q}$ [eq.(67)]

7: Second sub- increment

Calculate:

$\mathbf{A}$ [eq.(77)]; $\mathbf{w}$ [eq.(78)];

$\mathbf{s}_{n+1}$ [eq. (79) or eq. (81)]; $\mathbf{b}_{n+1}$ [eq.(82)];

$\mathbf{m}_{n+1}$ [eq. (83)]; $\Delta\xi$ [eq.(84)]; $\mathbf{a}_{n+1}$ [eq.(85)]

8: update the variables :

$$\boldsymbol{\sigma}_{n+1} = \mathbf{s}_{n+1} + p\mathbf{1}$$

update the state variables $\mathbf{a}_{n+1}, \mathbf{b}_{n+1}, \varepsilon_{qn+1}, \delta_{in}$

calculate the elastoplastic rigidity tensor $\mathbf{D}^{ep}$ [eq.(86)]; tangent or eqs.[(89),(90)]; consistent.

EXIT

2.3 Special features on the implementation of the model

In this section, some special features of the constitutive model are discussed, in terms of numerical implementation and simulation capabilities. These features can be very helpful for the purpose of describing accurately metal material behavior, and in particular for calibrating the model, towards predicting the mechanical response of metal components, to be discussed in the next section for the case of a physical experiment.

A first issue refers to the proper definition of the initial distance δ_{in} between the yield surface and the bounding surface at every "plastic loading process". During a cyclic loading with alternate excursions into the inelastic range, a "plastic loading process" starts when inelastic deformation initiates after elastic behavior and ends when the stress path is reversed and elastic behavior occurs again. In the beginning of this "plastic loading process", an update of δ_{in} and the corresponding unit normal to the yield surface $\mathbf{n}_{in}$ should be performed, using the current distance δ and the corresponding outward normal tensor $\mathbf{n}^{YS}$ respectively. In general, those values should remain constant until the end of the plastic loading process. Nevertheless, to account for a possible abrupt change of a loading direction in the stress space, in the present model, at every increment, the inner product between $\mathbf{n}_{in}$ and the current $\mathbf{n}^{YS}$ is monitored; if this product is positive, the values of δ_{in} and $\mathbf{n}_{in}$ remain unaltered, whereas if the inner product is negative, this implies that an abrupt change of direction of the stress path has occurred, and the values of δ_{in} and $\mathbf{n}_{in}$ are updated with current values of δ and $\mathbf{n}^{YS}$. Such an abrupt change of a loading direction in the stress space may occur at the onset of structural instability (buckling) or another type of bifurcation.

Another interesting feature of the model refers to the hardening rule of the outer (bounding) surface, as expressed in eq. (21). In order to improve the capabilities of the model to describe accurately the accumulation of plastic deformation in a stress-controlled loading scheme, the bounding surface hardening modulus $\bar{H}$ in the first bracket of eq. (21) is replaced by the modified modulus $\hat{H}$, expressed as follows

$$\hat{H} = \bar{H} + c\left[(\mathbf{b}\cdot\mathbf{b})^{1/2} - \mathbf{b}\cdot\mathbf{n}\right] \tag{93}$$

where c is the so-called ratcheting parameter, to be defined by stress-controlled material experiments. The modification has been suggested initially by Seyed-Ranjbari [55], and subsequently by Hassan & Kyriakides [40] [41].

Carbon steels are characterized by an abrupt change of slope in the stress–strain curve after initial yielding, associated with very low hardening, referred to as "plastic plateau", shown in **Figure 5a**. To model the "plastic plateau", the initial size of the YS is assumed the same as the size of the BS, and a low hardening modulus is employed for the BS. Therefore, during the first plastic loading (stages 1 → 2 in **Figure 5b**), the plastic deformation makes the YS shrink, according to eq. (3), while the B.S. hardens by a very small amount. During reverse plastic loading (stages 3 → 4 in **Figure 5b**), the two surfaces have a distance δ, the hardening function of eq. (8) is activated, and the Bauschinger effect is modelled.

A final issue, refers to the hardening modulus function, which is expressed by eq. (8) in the original version of the model [33]. A key constituent of the hardening modulus function is parameter h, which may have an important role in material cyclic response, affecting both the shape of the inelastic loop and, most importantly, the ratcheting rate. In the original version of the model [33], parameter h was proposed to be as a function of the ratio of the initial distance δ_{in} between the yield and the bounding surfaces at the current "plastic loading step" and the size of the bounding surface $\bar{k}$, expressed by the following equation:

$$h = \frac{a}{1 + d\left(\dfrac{\delta_{in}}{\left(2\sqrt{2/3}\right)\bar{k}}\right)^{m}} \tag{94}$$

where a , d, m are material parameters calibrated from cyclic stress-strain response obtained from material testing.

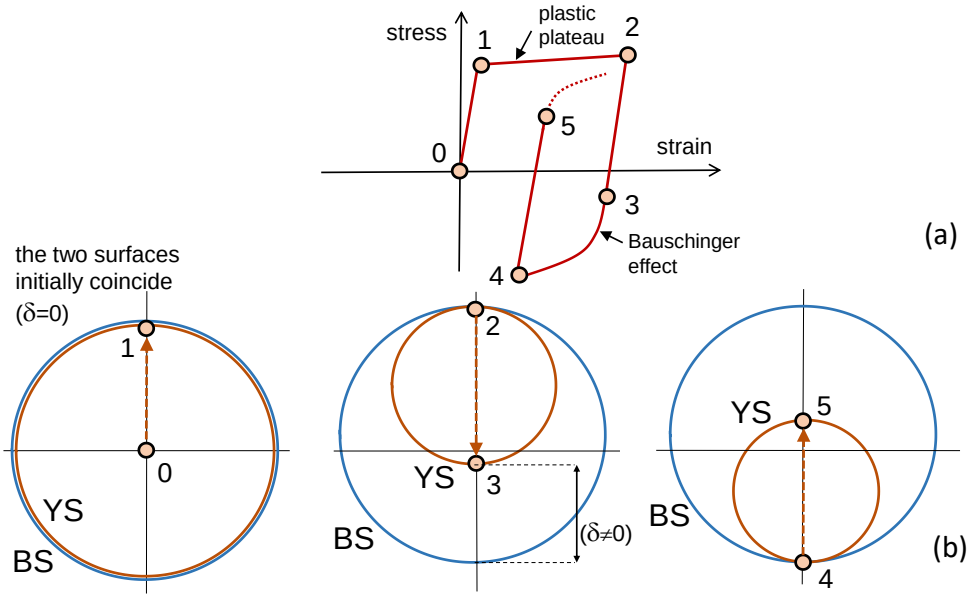

Figure 5. Schematic representation of the two-surface model implementation for modelling the "plastic plateau" of structural steels at initial yielding and the subsequent Bauschinger effect; initially (at stage 0) the yield surface YS coincides with the bounding surface BS.

In the present study, for improving the simulation capabilities of the present model, especially for stress-controlled loading schemes, a new expression is proposed for h, as follows:

$$h = \frac{a}{\left(\frac{\delta}{\left(2\sqrt{2/3}\right)k}\right)^{n} + d\left(\frac{\delta_{in}}{\left(2\sqrt{2/3}\right)\bar{k}}\right)^{m}} \tag{95}$$

In eq.(95) the above expression the value of h also depends on the ratio of the initial distance δ_{in} between the yield and bounding surfaces (as the previous case) at the current stress state, but also on the current distance δ between the two surfaces, and the size of the yield surface. Parameters a, d, m, *and* n in eq.(95) are material constants, which should be calibrated on the basis of experimental stress-strain cyclic response. In an attempt to show the effect of h on cyclic inelastic behavior of a typical steel material, and the sensitivity of parameters a, d, m, n, a short parametric study is conducted focusing mainly on the ratcheting rate. In **Table 1**, material parameters corresponding to a 355 grade steel are presented. Figure 6 depicts the influence of the four hardening parameters on stress-strain response. The results show that increasing the value of a, n, and m, the

"steepness" of the hardening modulus function increases, while an increase of the value of d has opposite effects on the hardening modulus.

Furthermore, the value of hardening modulus affects the ratcheting rate. **Figure 7** illustrates the effect of parameter a on ratcheting; an increase of the ratcheting rate of strain accumulation occurs as the value of a increases, while the value of d has opposite effect. Finally, the influence of the relaxation parameter c, introduced in eq.(93), on the ratcheting rate is also shown in **Figure 8**.

Table 1. Summary of basic set of material parameters used in the analyses presented in section 2.3.

Isotropic hardening parameters [yield surface]	σ_y (MPa)	280
	Q (MPa)	-30
	b	80
Isotropic hardening parameters [bounding surface]	σ_b (MPa)	400
	Q_b (MPa)	70
	b_b	30
Hardening function parameters	$\bar{H}$ (MPa)	2,000
	a (MPa)	56,000
	d	4
	n	0.4
	m	2
relaxation coefficient parameter	c	10

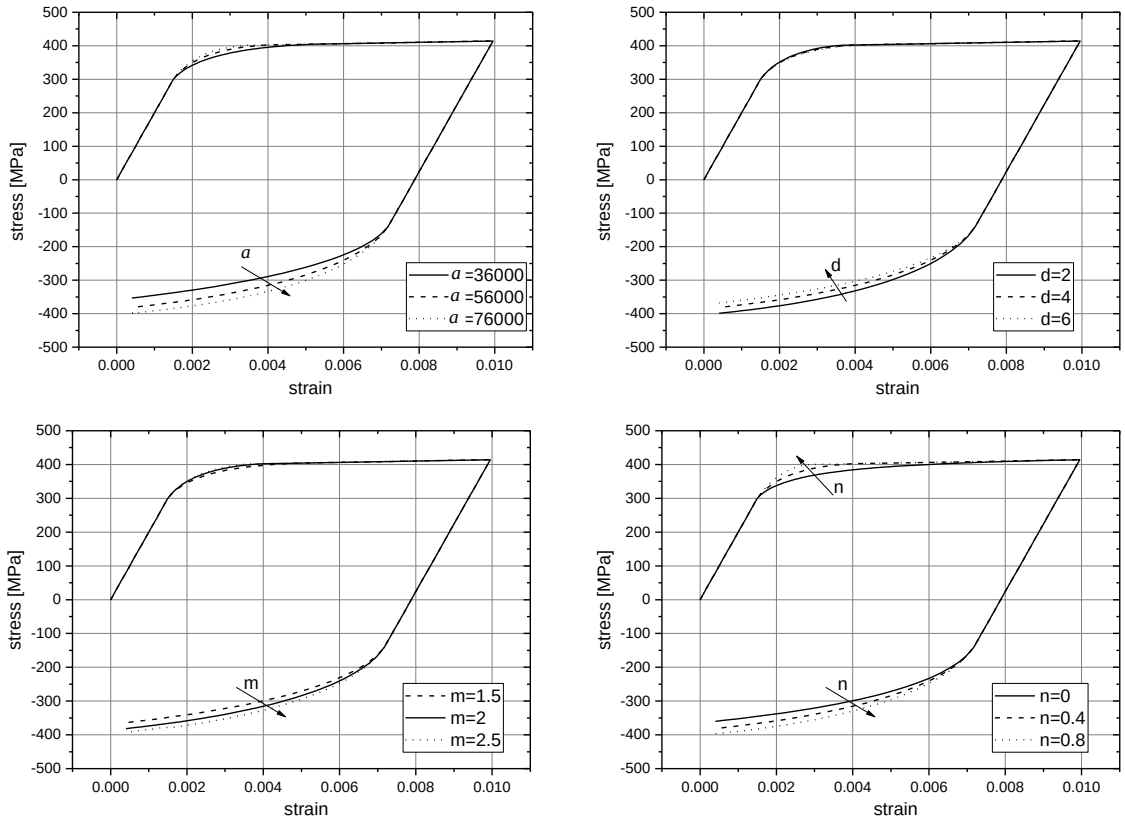

Figure 6. Influence of material parameters a, d, m, and n in eq. (95) on material hardening.

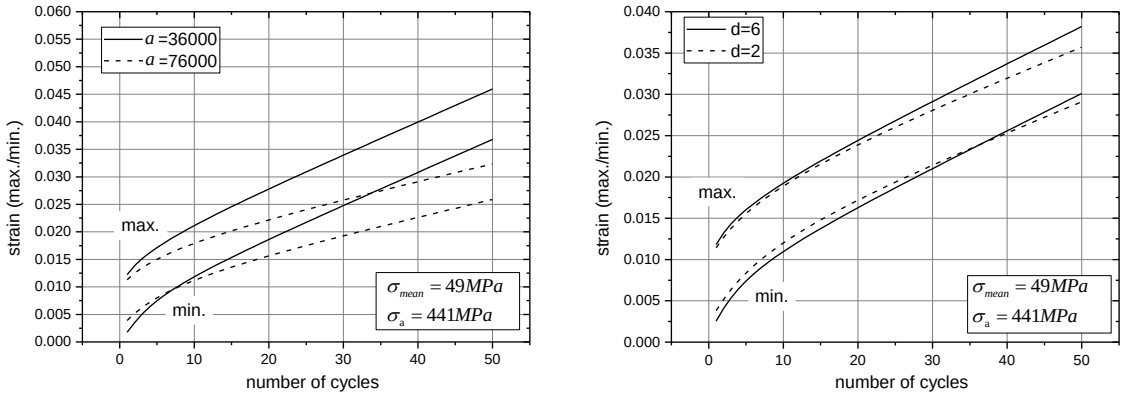

Figure 7. Influence of material parameters a and d in eq. (95) on ratcheting rate.

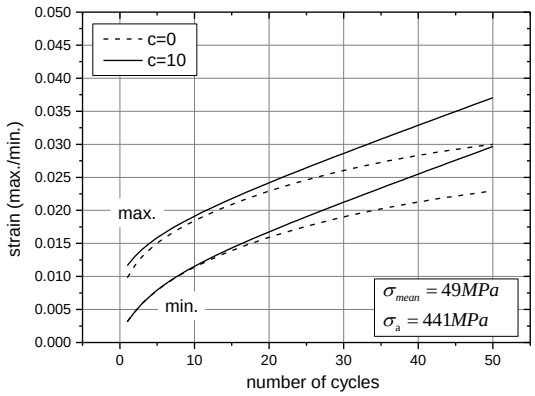

Figure 8. Influence of relaxation parameter c in eq. (93) on ratcheting rate.

2.4 Numerical simulation of small-scale experiments

Cyclic tests on small-scale steel strips from of two types of carbon steel (a high-strength steel and a mild steel) are simulated using the present model. The first material test data set considered in the present study refers to TS590 high-strength steel grade specimens, tested by Centro Sviluppo Materiali, (now RINA), Rome, Italy, in the course of a European research program on the structural behavior of tubular structural members [56]. The material yield and ultimate stress were measured equal to 735 MPa and 812 MPa respectively. Three strip specimens from this material are considered, one cyclic stress-controlled test with nonzero mean stress ($\sigma_{\text{mean}} = 74$ MPa) and stress amplitude ($\sigma_{\text{a}} =$ 660.8 MPa) and two strain-controlled tests at strain amplitude $\pm$ 0.96% and $\pm$ 1.128% respectively. The main target of this analysis is the simulation of both stress-controlled and strain-controlled controlled tests, using the same material parameters.

Accurate description of these small-scale tests also requires that the "plastic plateau" is taken into consideration, following the procedure described in detail in Section 2.3. Different approaches for defining parameter h have been considered. In the first approach, equation (94) is adopted as proposed by Dafalias and Popov [33]; the second approach employs the value of h defined by eq. (95) as proposed by the author; finally, in the third approach a constant value of h, equal to a in eq. (94), is used (in that case b equal to zero). It is important to emphasize that the values of the other material parameters are the same for all these cases, and equal to those presented in **Table 2**.

The results show that the value of h has a decisive role in simulating stress-controlled tests, whereas the simulation of strain-controlled tests is less sensitive to the value of h.

The graphs in **Figure 9** to **Figure 11** show that, for the strain-controlled tests, all three expressions for the value of h can predict rather satisfactory the stress-strain response, while the value of h has significant effect on stress-controlled test as shown in **Figure 12**. Using eq. (94) it was not possible to describe adequately both the stress-controlled tests and the strain-controlled tests, despite the fact that numerous attempts were conducted over a wide range of values for the material parameters. On the other hand, the use of eq. (95) improves significantly the simulation capabilities of the model, with respect to the small-scale tests allowing for more accurate description of both stress-controlled and strain controlled tests. Finally, the third approach, which uses a constant value for h, shows a poor performance.

The second set of material test data refers to strips from P355N steel (mild steel of grade 355, according to EN 10216), widely used in industrial piping components. The tests have also been performed by CSM, Rome, Italy in the course of INDUSE project [57]. The material yield stress and ultimate stress were measured equal to 409 MPa and 576 Mpa respectively These strip specimens have been extracted from 8-inch-diameter pipe elbows, in order to characterize the elbow material. One cyclic stress-controlled test with nonzero mean stress (σ_{mean} = 40 MPa) and amplitude (σ_{a} = 392 MPa) has been performed, together with three strain-controlled tests with strain amplitudes $\pm$0.75%, $\pm$1.25%, and $\pm$2.25% respectively. The material parameters used in these calculations are shown **Table 2**.

The experimental stress-strain curve and the corresponding numerical simulation are presented for the three strain-controlled tests in **Figure 13a**. Furthermore, **Figure 13b** depicts the accumulation of plastic deformation over the loading cycles as measured in the stress-controlled test and the corresponding numerical simulation. It should be underlined that the same values of material parameters are employed for both the stress-controlled and strain-controlled tests. Moreover, in those calculations, the expression of eq. (95) is also used for defining the parameter h due to its better performance in describing the cyclic material behavior, as discussed in the case of high-strength steel.

The results in **Figure 9** to **Figure 13** show a very good agreement between test measurements and numerical simulations, indicating that the present model, of properly implemented and calibrated, is capable of describing accurately cyclic response of carbon steel material, subjected to both stress-controlled and strain-controlled loading schemes.

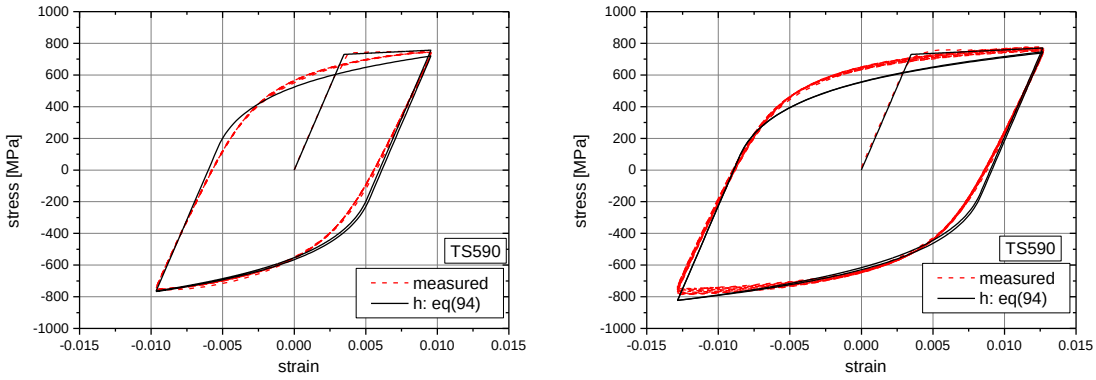

Figure 9. Strain-controlled material curves for the TS590 material; in the simulation value of h is computed according to eq. (94).

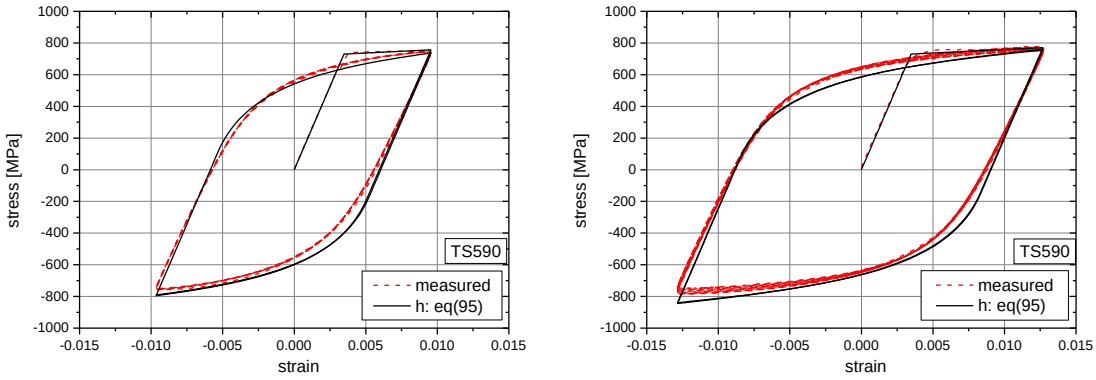

Figure 10. Strain-controlled material curves for the TS590 material; simulations using the value of h from eq. (95).

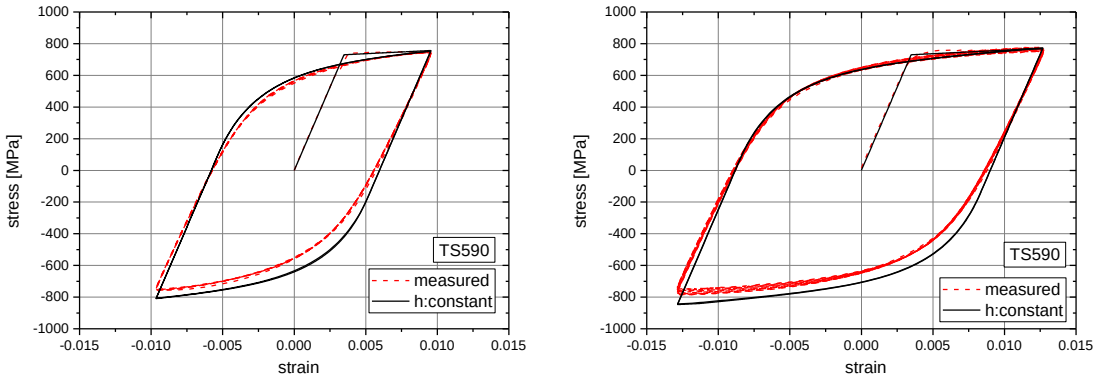

Figure 11. Strain-controlled material curves for the TS590 material; simulations with constant h.

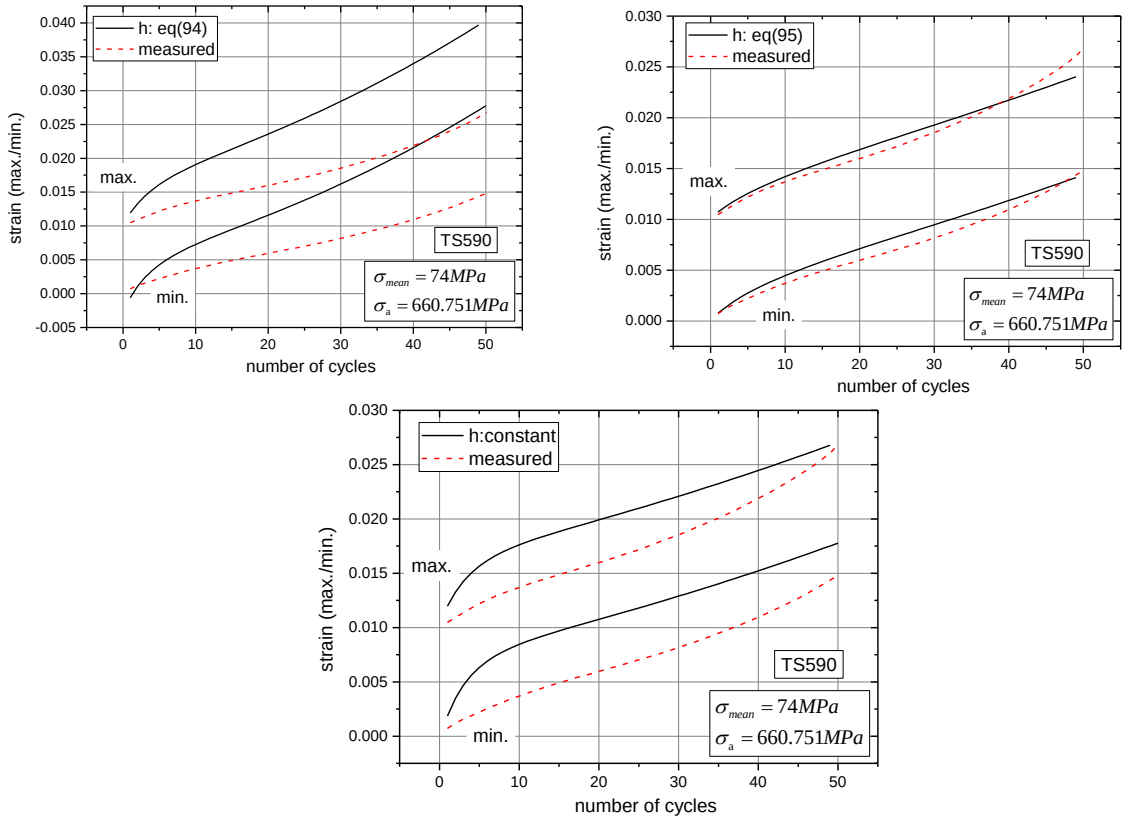

Figure 12. Cyclic stress-controlled material test for TS590 material; evolution of maximum strain.

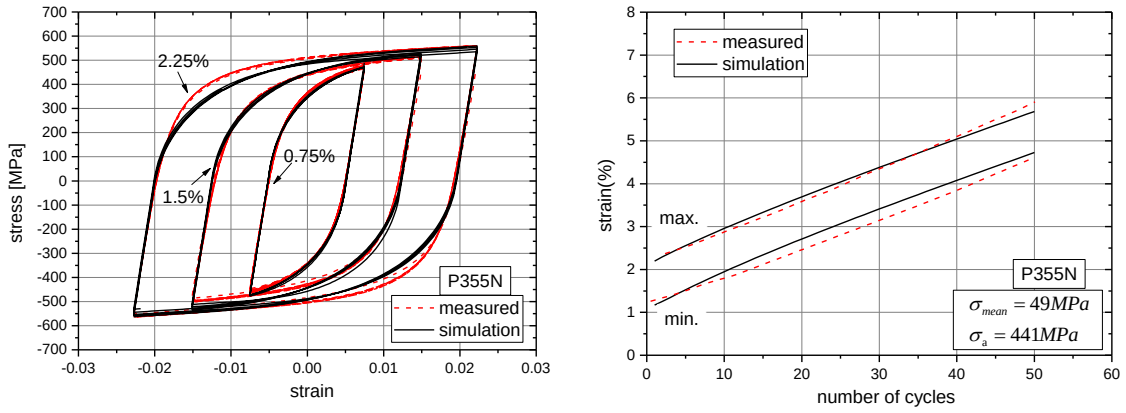

(a) (b)

Figure 13. Material test for P355N material (a) strain-controlled test. (b) Cyclic stress-controlled test and; evolution of maximum-minimum strain.

Table 2. Summary of material parameter values for TS590 high-strength steel and P355N steel material.

		TS590	P355N
Isotropic hardening parameters [yield surface]	σ_y (MPa)	730	280
	Q (MPa)	-275	-30
	b	500	80
Isotropic hardening parameters [bounding surface]	σ_b (MPa)	730	480
	Q_b (MPa)	10	50
	b_b	100	5
Hardening function parameters	$\bar{H}$ (MPa)	9,000	2,000
	a (MPa)	160,000	56,000
	d	20	4
	n	2.5	0.4
	m	4	3.55
relaxation coefficient parameter	c	5	10

2.5 Conclusions

The present chapter describes an efficient numerical implementation of a bounding-surface (two-surface) model for cyclic plasticity, suitable for simulating the mechanical response of metal structural members and components, subjected to strong cyclic loading. The model is implemented in a finite element environment and its integration follows an elastic-predictor/plastic-corrector scheme. All steps of the numerical integration algorithm are presented in detail allowing for its implementation in a material-user subroutine for a finite element software. Some special features of the model are addressed and discussed to elucidate its capabilities in simulating accurately steel material response. An important issue refers to the relative position of the two surfaces, and their possible contact within the increment under consideration. This constitutes an essential issue for defining the hardening modulus and it is taken into account in a rigorous manner. Furthermore, the sensitivity of cyclic response on some key material parameters is presented. In particular, a modification on the hardening modulus is proposed, which improves the model

capabilities in predicting strain accumulation under non-symmetric stress-controlled conditions.

Simulations of small-scale tests from mild steel and high-strength steel have been performed, which demonstrate the capability of the model to describe both stress-controlled and strain-controlled tests using the same set of material parameters.

Chapter 3 - Numerical Simulation of Mechanical Behaviour of Steel Bends Under Strong Cyclic Loading

In this chapter the mechanical behavior of steel pipe bends (elbows), subjected to strong cyclic loading conditions, associated with repeated plastic deformations of alternate sign is examined. The elbows are modeled with finite elements, which account for the measured elbow geometry and for the actual properties of steel elbow material. To simulate material response under repeated inelastic deformation, the cyclic-plasticity material model presented in Chapter 2 is employed, based on the bounding-surface concept, implemented through an in-house material subroutine. Upon appropriate calibration with small-scale tests in strip specimens, extracted from the bends under consideration, the constitutive model is employed for predicting the mechanical response of large-scale physical laboratory experiments. Very good comparison has been obtained in terms of global load-displacement response, as well as in terms of local strains and their accumulation over the loading cycles (ratcheting rate) at specific elbow locations, indicating that the bounding-surface model can be an efficient tool for predicting accurately the mechanical response of piping components under severe cyclic loading conditions. In the final part of this chapter, using the validated numerical models, extensive results are obtained on the effect of internal pressure on strain and deformation accumulation at different locations of the elbow outer surface, for different values of pipe thickness.

3.1 Introduction

Steel pipe elbows, also referred to as pipe "bends", are essential components of industrial piping systems in chemical, petrochemical, power plants or energy terminals, and their performance is of paramount importance for the structural integrity of the industrial facility. They can accommodate thermal expansions, and absorb other externally-induced loading, and are considered as critical components for the structural integrity of piping systems. Pipe elbows are very flexible with respect to straight pipes of the same cross-section, and their response is characterized by higher stresses and strains at critical locations, a feature associated with cross sectional ovalization. The pioneering paper by Rodabauch and George [58] presented an analytical solution for elbow flexibility

and stress in curved pipes, which has been the basis for the relevant flexibility and stress indices [59], adopted by ASME standards [60][61] for the design of piping systems. In the case of extreme loading conditions [62][63], such as strong earthquakes or shutdown/restart operations, high local stresses and strains are induced at critical locations, both in the longitudinal and the hoop direction, which may lead to pipe elbow failure, in a mode quite different than the failure mode observed in straight pipes [64].

There has been a substantial amount of experimental and numerical research effort on the structural performance of elbows subjected to in-plane bending moments, which demonstrated the development of excessive cross-sectional ovalization and significant stresses and strains at critical elbow locations, mainly at the elbow flanks [65][66]. These works have also shown that the response under closing bending moments is substantially different than the response under opening bending moments, due to the different sign of cross-sectional ovalization [67]. In addition, it has been well documented that the elbow stiffness, the ultimate moment and the corresponding deformation capacity are affected significantly by the level of internal pressure. For an extensive literature review of static strength of pipe bends, the reader is referred to the review paper by Karamanos [64].

In addition to the aforementioned works on ultimate strength, the structural performance of elbows under severe cyclic loading has attracted significant research attention, motivated by the need of safeguarding integrity of the piping system under shutdown or seismic conditions. Under strong cyclic loading, elbows may exhibit significant accumulation of plastic strain ("ratcheting"), which may accelerate failure due to plastic collapse or low-cycle fatigue. The accumulation rate has been more pronounced in pressurized elbows, where the biaxial state of stress is characterized by a high mean stress in the hoop direction [68].

Experimental results showing the ratcheting response of pressurized carbon and stainless steel pipe elbows have been reported by Beany [69][70] and later by Yahiaoui *et al.* [71] and Moreton *et al.* [72], summarizing in a large-scale UK experimental program on piping component integrity subjected to cyclic loading, leading to pipe failure due to low-cycle fatigue. Significant research results on carbon/stainless steel pipe bends have also been performed by EPRI/NRC [73][74], motivated by the response of piping systems to seismic loading, using a shaking-table apparatus for testing piping components and systems. The test results indicated the development of strain ratcheting, leading to elbow failure primarily in the form of "fatigue-ratcheting". Extensive experimental works on the

seismic response of elbows and piping systems have also been performed in Japan, for the purpose of safeguarding the integrity of nuclear power plants under severe earthquake action. Notable experimental results on the seismic response of piping systems have been reported in the early paper by Fujita *et al.* [75], whereas the experiments by Fujiwata *et al.* [76] and Yoshino *et al.* [77] verified the "fatigue-ratcheting" mode of failure for seismically-loaded piping components and systems. An interesting work has been published by DeGrassi *et al.* [78], in an attempt to simulate the testing program of the Japanese Nuclear Power Engineering Corporation (NUPEC) [79], with emphasis on inelastic pipe response and ratcheting. Chen *et al.* [80] investigated experimentally and numerically the gradual evolution of hoop strain in pressurized elbows subjected to cyclic in-plane bending at the elbow flank. A series of tests on 2-inch pipe elbows, subjected to severe cyclic loading, have been performed by Hassan *et al.* [81], and reported measurements on strain accumulation at various locations, focusing on the effect of internal pressure on elbow ratcheting. In a more recent publication, Nakamura and Kasahara [82] studied the response of piping systems under excessive seismic load by means of shaking table excitation tests on steel pipe elbows, and concluded that piping systems fail under fatigue cracking, accompanied by ratcheting deformation. More recently, Ravi Kiran *et al.* [83] [84] presented shaking-table test results on carbon steel pipe bends and piping systems respectively, subjected to seismic loading, and reported significant hoop strain accumulation measurements at flank location of the elbow; on the other hand, the axial strain accumulation at that location has been found less pronounced. Moreover, Labbé *et al.* in [85] and Sollogoub in [86] in the contents of project (MECOS) present experimental results of piping system and elbow subjected to strong cyclic loading with target to propose and improve design criteria. Finally, it is worth mentioning the cyclic loading tests on 8-inch-diameter specimens performed in the course of INDUSE project [57]; those tests are considered in the present study for validation of the numerical model, and will be described in more detail in section 3.2.

The numerical simulation of ratcheting in steel piping components, and in particular in pipe elbows, has been a computational challenge, mainly because of the strong bi-axial state of stress at the critical areas. It is noted that, even for low levels of internal pressure, elbows exhibit a substantial amount of biaxial plastic deformation, due to cross-sectional ovalization. The key issue for a successful simulation of ratcheting is the choice of an appropriate constitutive model. The recent paper by Hassan and Rahman [16], following

an extensive literature review, offers an evaluation of seven constitutive models with respect to their ability in simulating elbow ratcheting in comparison with the experimental results reported in [81]. Towards this purpose, Hassan and Rahman employed several constitutive models, including Chaboche-type [11][87], and Ohno–type models [15] [88][89], and discussed the model effectiveness in predicting elbow ratcheting. In a more recent paper, Islam *et al.* [17] presented a modified Chaboche model [87], proposing a more elaborate evolution law for the backstress tensor, for improved simulations of elbow ratcheting.

All the aforementioned constitutive models belong to the category of the so-called "coupled" models, employing the terminology suggested by Bari and Hassan [6], and constitute extensions of the classical nonlinear kinematic-hardening model [9]. On the other hand, the use of constitutive models based on "bounding surface" concept [33], has been quite limited in the simulation of elbow cyclic response. Analytical calculations on material ratcheting have indicated that these models, upon proper calibration, may offer an efficient tool for simulating ratcheting [32]. Nevertheless, to the author' knowledge, the only attempt to simulate the cyclic behavior of piping components using an "uncoupled" plasticity model has been reported by Varelis *et al.* [53][54], who implemented the Tseng-Lee model [36], a simplified version of the original "bounding surface" concept.

3.2 Outline of full-scale of experimental testing

Table 3 summarizes the elbow experiments considered in the present study. The experiments under consideration have been conducted at Delft University of Technology (TU Delft) and at Centro Sviluppo Materiali SPA (CSM) in the framework of INDUSE project [57], a large European project on the seismic safety of industrial facilities, and have been presented in detail in previous publications of the senior author [53][54]. In the present section, an outline of the experiments is presented. The specimens, shown in **Figure 14**, are typical 8-inch SCH40 long-radius induction bends, manufactured according to ASME B16.9 [90], with nominal diameter and thickness equal to D=219.1 mm and t=8.18 mm respectively, widely used in industrial piping applications. The steel material is P355N, according to European EN 10216 standard, equivalent to X52 steel grade in API 5L

Table 3. Summary of strain range Δε measured in experiments and numerical predictions.

Test/No.	Average measured thickness (mm)	Imposed displacement ΔL	Pressure (bar)	Δε(%) numerical	Δε(%) experimental
E070-0	9.99	± 70mm	0	0.89	1.23
E150-0	9.99	± 150mm	0	2.25	2.61
E200-0	9.92	± 200mm	0	3.33	-
E250-0	10.105	± 250mm	0	3.74	3.84
E200-032	9.72	± 200mm	32	2.95	3.01
E200-070	9.88	± 200mm	70	2.49	2.45
E200-120	10.09	± 200mm	120	1.91	2.28

In particular, the second column of **Table 3** reports the average measured thicknesses of the elbow in the cross sections presented in **Figure 15**. The bend radius R is equal to 1.5 times the pipe diameter (R/D=1.5), and it is but-welded to two straight pipe segments with the same nominal diameter and thickness. **Figure 14** shows the experimental set-up; a hinged support was used at the one end of the specimen, while the other end was free to slide horizontally and rotate, allowing for in-plane bending of the elbow under an imposed displacement in the horizontal direction. Displacement-controlled tests of the elbows have been performed considering two different parameters: (a) the applied displacement (ΔL) and (b) the level of internal pressure (P) in the elbow. Non-pressurized tests were conducted by TU Delft, while cyclic tests in the presence of internal pressure were conducted by CSM. The change of vertical diameter of elbow (flattening) has been monitored with the use of special-purpose frame devices, attached on each specimen and equipped with displacement transducers, as shown in **Figure 14**. In the non-pressurized tests (TU Delft), flattening measurements referred to the change of the vertical diameter were obtained at the middle cross-section (**Figure 14**a). In the pressurized tests (CSM), flattening measurements have been obtained in a cross-section slightly away from the central section as depicted in **Figure 14**b. Strain-gauges were also placed at the flank region, somewhat lower than the middle line (**Figure 15**), in order to account for the critical location of the elbow as indicated by preliminary numerical simulation.

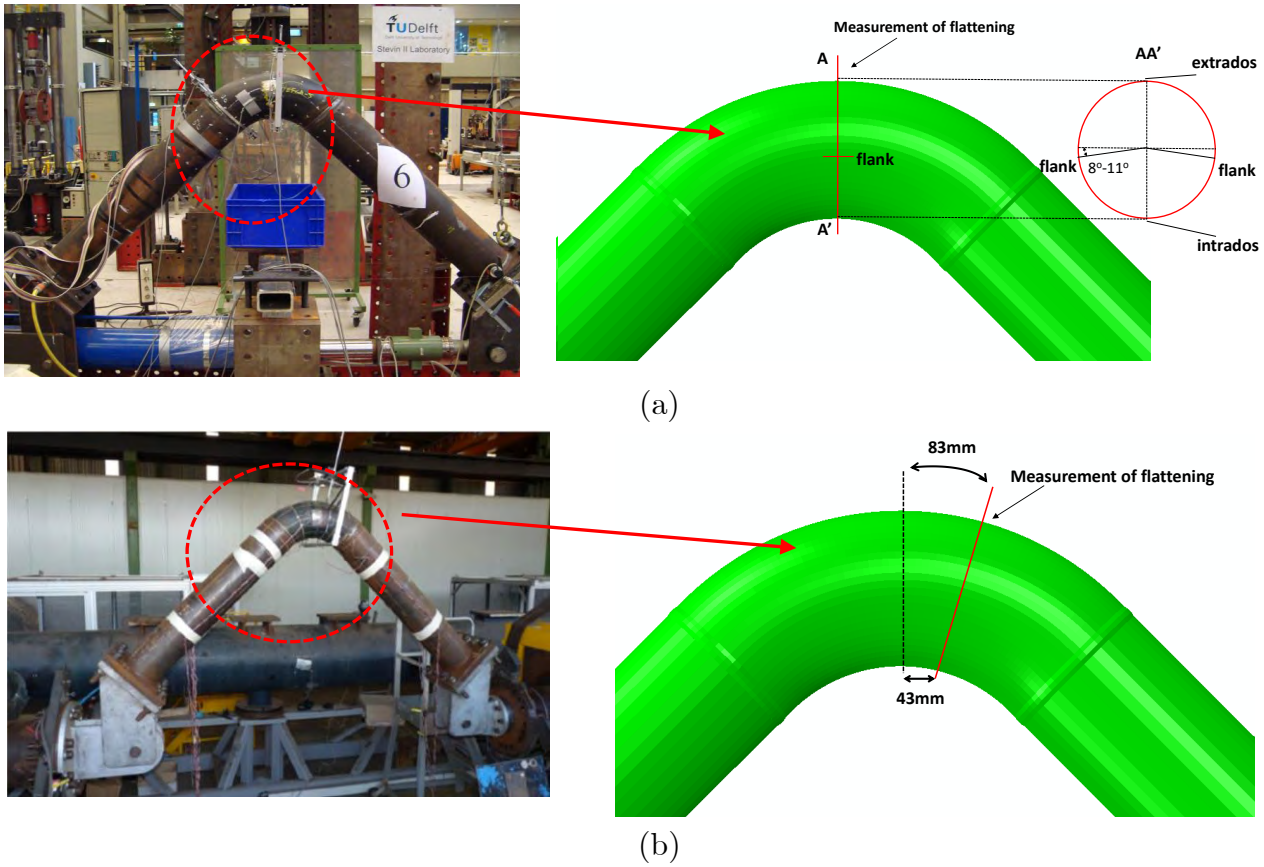

Figure 14. Experimental set-up and locations of measurement of flattening [57]; (a) non-pressurized tests [TU Delft], Delft, The Netherlands, (b) pressurized tests [CSM], Sardinia, Italy.

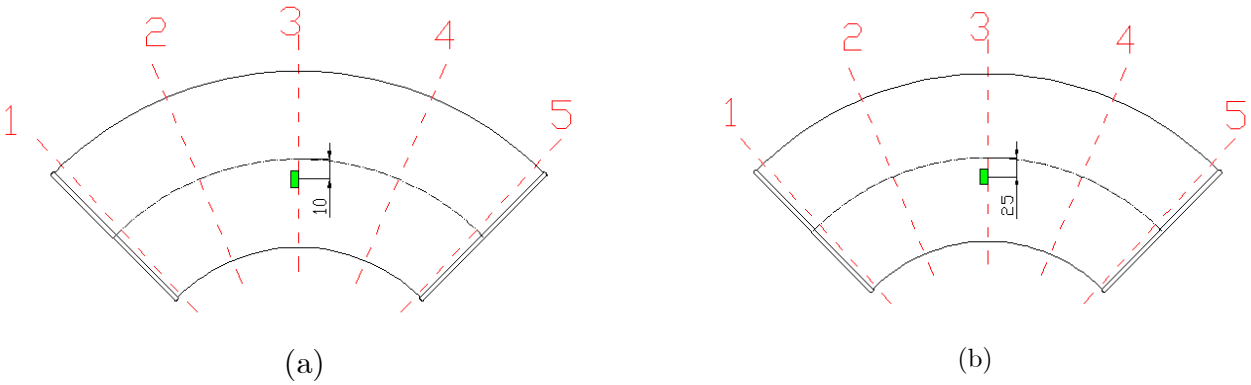

Figure 15. Thickness and strain measurement locations in (a) non-pressurized tests [TU Delft], (b) pressurized tests [CSM].

3.3 Finite element modeling

Finite element models (**Figure 16**) have been developed in order to simulate the elbow experiments, presented in section 3.2, using the general-purpose software ABAQUS. The models employ the geometry of the specimen based on measurements conducted prior to the execution of the experiments. The elbow and the two straight pipe segments have been modeled as three separate parts connected through appropriate "tie" connections in ABAQUS. The support conditions have been imposed in the numerical model exactly as in the experimental set-up, using appropriate kinematic constraints at the two ends of the straight parts: a hinged support is imposed at the left end, while the right end is free to slide horizontally and rotate in the plane of bending, as in the experimental.

In order to calibrate the material model described in detail in Chapter 2, tests on strip specimens have been used. The strips have been extracted from elbows fabricated from the same heat as those tested in the experiments (P355N steel material). The tests for material characterization were performed by CSM, Rome, Italy, in the course of the INDUSE project [57]. More specifically, one stress-controlled cyclic test had been performed with mean stress $\sigma_{mean} = 40$MPa and amplitude $\sigma_a = 392$MPa, together with three strain-control cyclic tests, with strain amplitudes $\pm$ 0.75%, $\pm$ 1.25%, and $\pm$ 2.25%. The calibration of the material presented in detail in Chapter 2. In **Figure 13**a, the stress-strain experimental curve and the numerical fitting from three strain-controlled tests are presented. Furthermore, **Figure** 13b depicts the evolution of ratcheting as measured in the stress-controlled test and the corresponding numerical simulation. **Table 2** summarizes the material parameters. It should be underlined that (a) the same set of values for material parameters have been employed for simulating both stress-controlled and strain-controlled tests, (b) this set of parameters has been used for predicting the response of elbows in the physical experiments so that a fair comparison with the full-scale tests is conducted, as described in section 3.4.

A preliminary analysis has also been conducted for determining the optimum number of elements through the pipe thickness, as well as the type of element to be used in the simulations. For the number of elements through the pipe thickness three cases have been examined with; three, six, eight elements. The numerical results considering those three cases indicated that six elements is the optimum number of elements through the pipe thickness. In addition, this preliminary study indicated that the type of element employed

in the analysis has a minor effect on the global response of the elbow, i.e. on the force-displacement diagram. However, there exists a small influence of the element type on the computed value of strain at the critical location. Among other options, element C3D8R has been chosen because of its very good comparison with experiments in terms of local strains at the measurement locations and its computational efficiency.

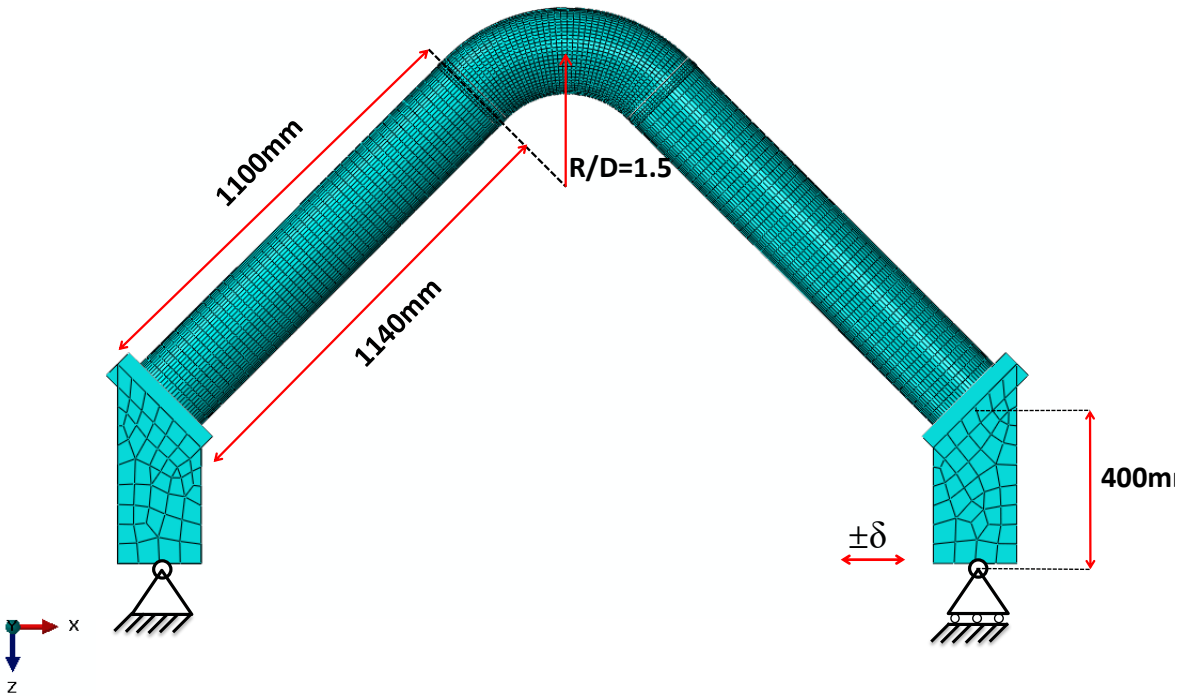

Figure 16. Numerical finite element model, simulating the experimental procedure.

3.4 Numerical simulation of experiments

The numerical models described in section 3.3, incorporating the constitutive model presented in Chapter 2, are employed to simulate the laboratory experiments outlined in section 3.2. The main purpose in this task is to present the capability of the finite element model and the constitutive model under consideration to predict accurately the mechanical response of steel pipe elbows subjected to strong fully-reversed cyclic loading. The computation of cross-sectional flattening and local strains is performed at the locations where the corresponding experimental measurements were obtained, as described in section 3.2.

In **Figure 17**, contour plots for the distribution of Von Mises stress and the equivalent plastic strain in the elbow at maximum closing displacement are depicted for specimen

E150-0. The contour plots show that the critical area is located at the elbow flank, which is in agreement with the corresponding experimental observations; in particular the fatigue crack occurs at the flank region as shown in **Figure 17**c and has the same configuration as the high-strain pattern shown in **Figure 17**b. The ovalization of middle cross-section under opening and closing bending is shown **Figure 18**(a) and (b) respectively. It is interesting note that the numerical results show that the equivalent plastic strain is higher at the inner surface, and this implies that the fatigue crack begins at the inner surface of the elbows, an observation also reported in recently published experimental results [91].

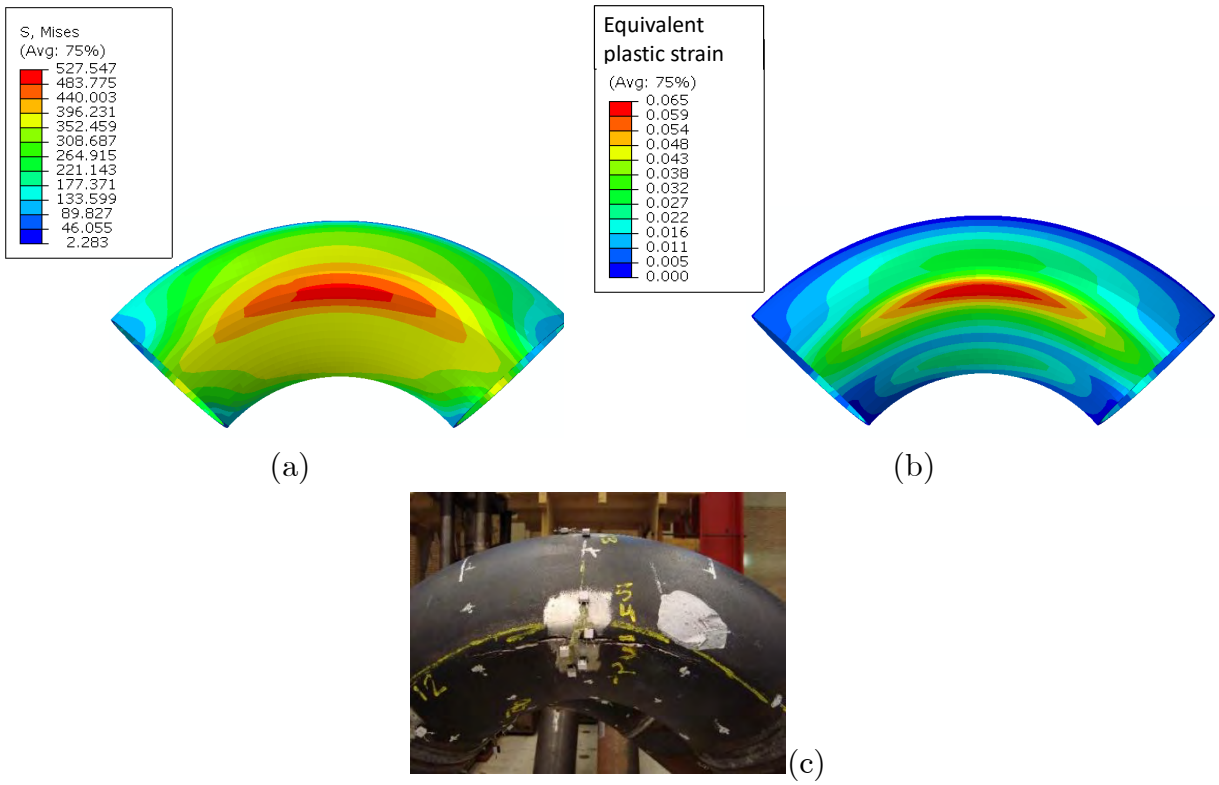

Figure 17. Elbow stress and deformation under in-plane bending; (a) distribution of Von Mises stress; (b) distribution of equivalent plastic strain; (c) failed (cracked) specimen [57] .

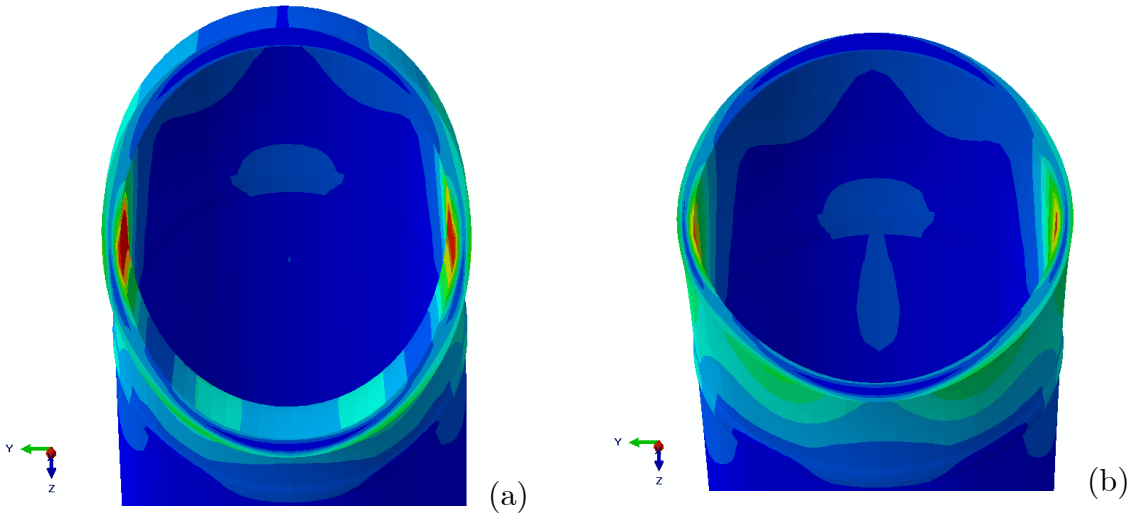

Figure 18. Distribution of equivalent plastic strain at the middle cross section for (a) opening bending; and (b) closing bending.

In **Figure 19** to **Figure 26** comparisons between the experimental data and the numerical predictions using the finite element model are offered in terms of: (a) load-displacement "global response" of the elbow, (b) elbow flattening at specific cross-sections and (c) strain evolution at the critical location (flank) with respect to the number of cycles. Initially, **Figure 19** to **Figure 22** depict the comparison between experiments and numerical simulations for the non-pressurized tests, for four values of applied cyclic displacement amplitude, namely ± 70 mm, ± 150 mm, ± 200 mm and ± 250 mm. In all cases, the load-displacement diagrams and the flattening of the middle section are in very good agreement with the experimental measurements. Furthermore, the evolution of strain at the critical location ("flank") with respect to the number of cycles is also presented in **Figure 19**c and **Figure 20**c. Both numerical and experimental results indicate that strain ratcheting occurrs in specimens E070-0 and E150-0. Furthermore, as the amplitude of applied displacement increases, the ratcheting rate increases. Unfortunately, strain measurements at the critical locations may not be available for specimens E200-0 and E250-0. This due to the large imposed displacements, so that the corresponding strain gauges did not record.

In **Figure 23**, a summary of force-displacement diagrams (loops) for the first loading cycle in each test is presented, as measured during the experiments (**Figure 23**a) and calculated in the corresponding numerical simulations (**Figure 23**b). The comparison of

the diagrams in **Figure 23**a and **Figure 23**b shows a remarkable agreement between experimental data and numerical predictions.

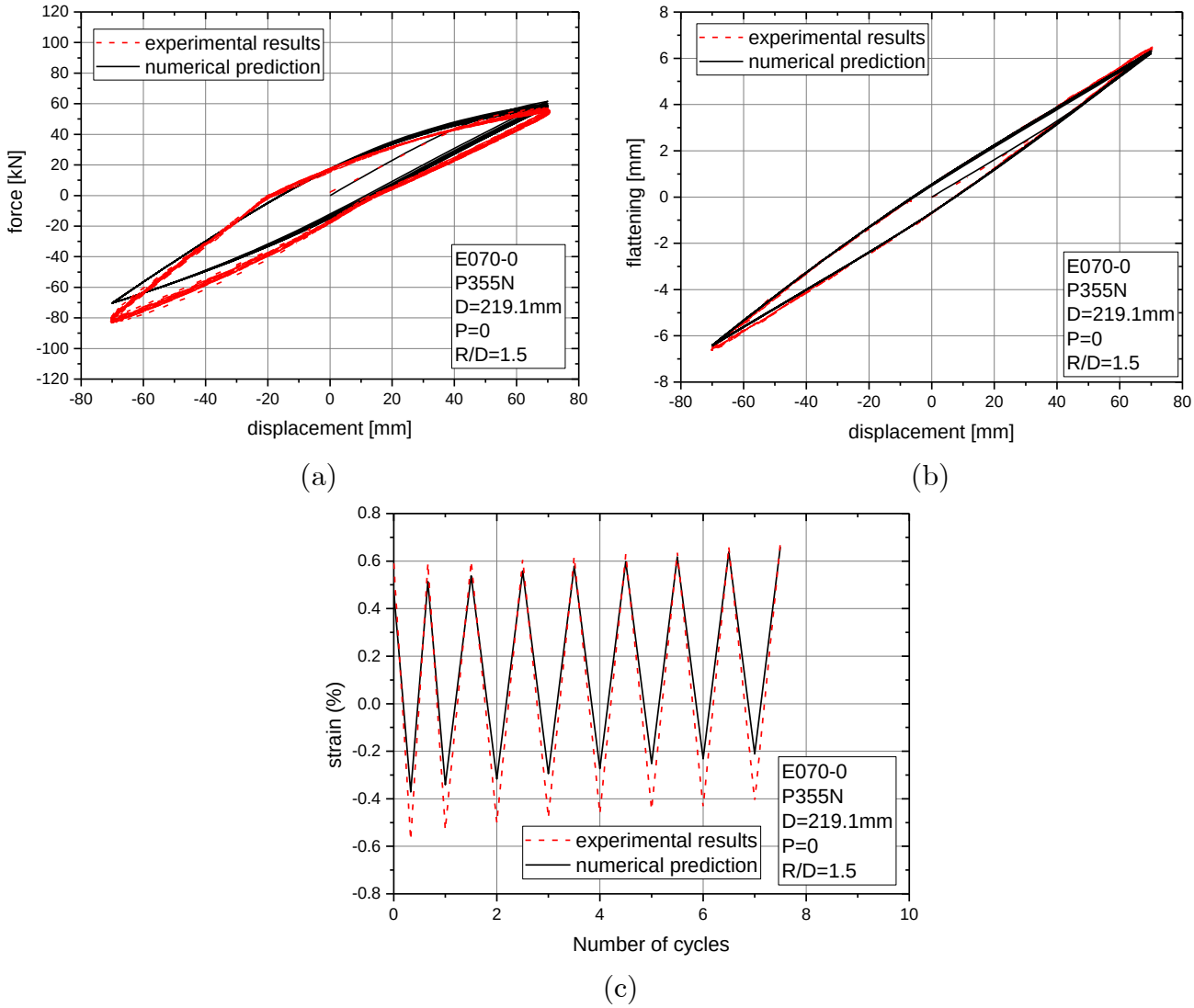

Figure 19. Comparison between experimental and numerical results [E070-0 specimen]; (a) load-displacement response; (b) elbow flattening; (c) evolution of hoop strain at critical location (elbow flank).

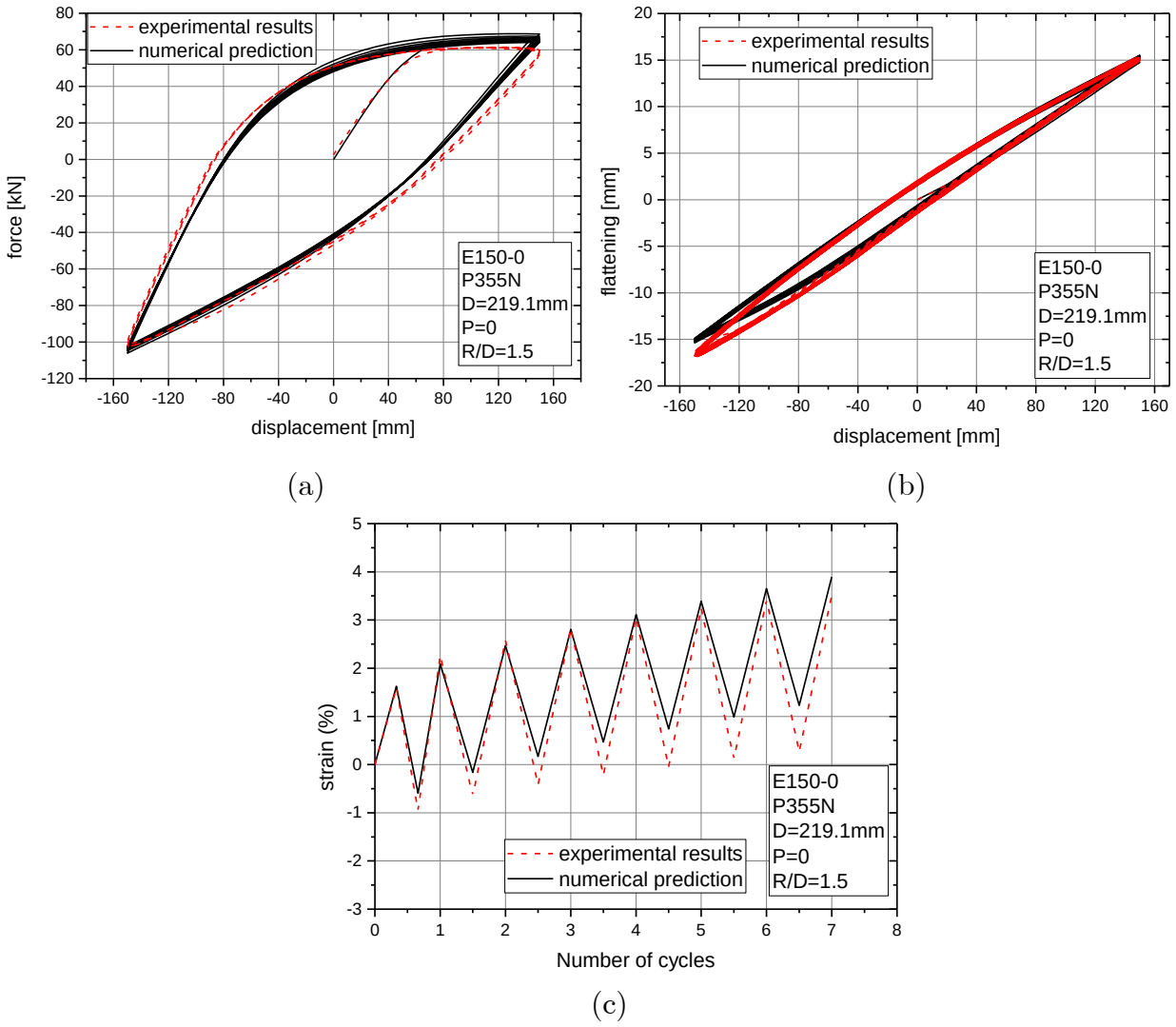

Figure 20. Comparison between experimental and numerical results [E150-0 specimen]; (a) load-displacement response; (b) elbow flattening; (c) evolution of hoop strain at critical location (elbow flank).

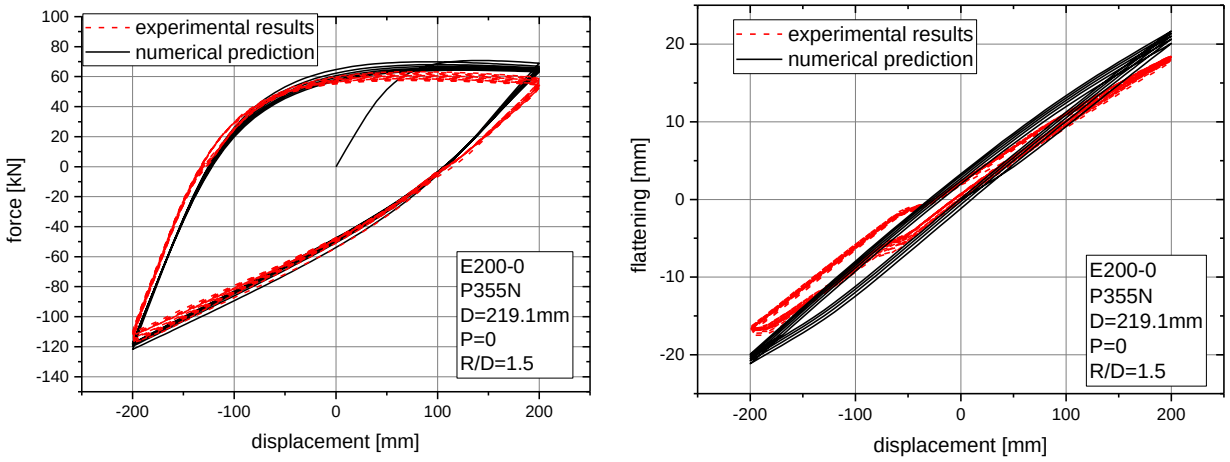

(a) (b)

Figure 21. Comparison between experimental and numerical results [E200-0 specimen]; (a) load-displacement response; (b) elbow flattening.

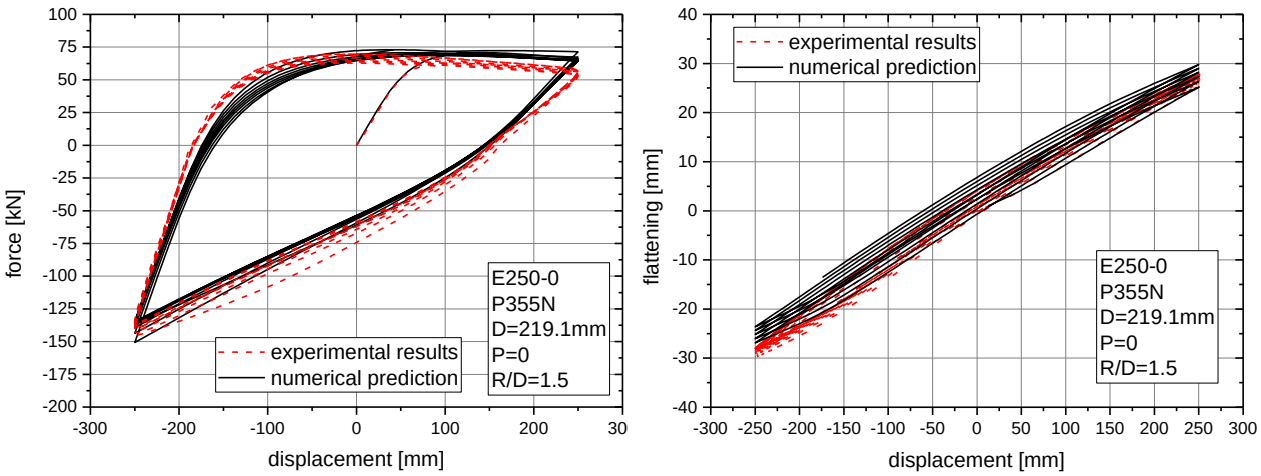

(a) (b)

Figure 22. Comparison between experimental and numerical results [E250-0 specimen]; (a) load-displacement response; (b) elbow flattening.

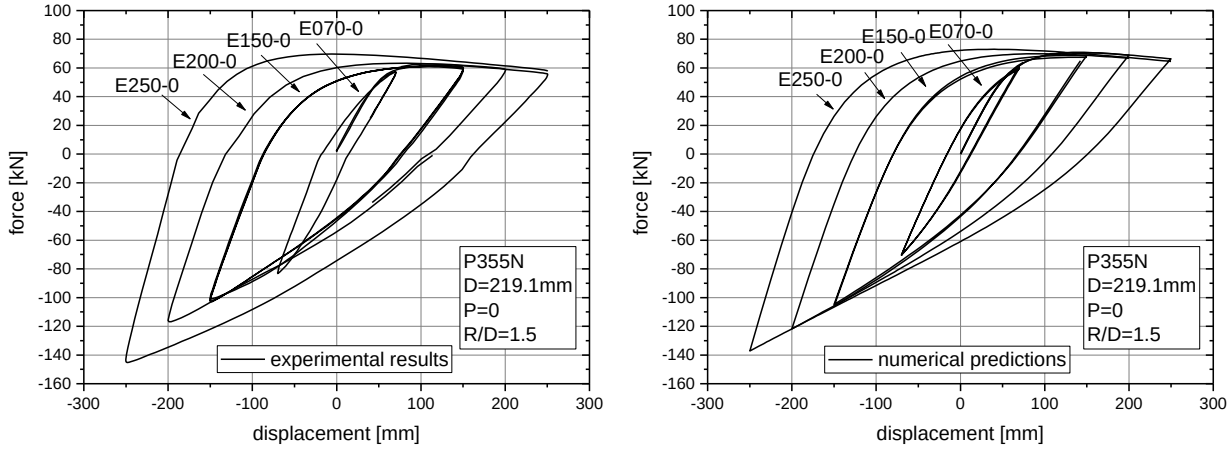

Figure 23. Force-displacement response for non-pressurized elbows during the first loading cycle; (a) experimental results, (b) numerical predictions.

In **Figure 24** to **Figure 26**, numerical predictions are depicted for internally pressurized elbow specimens. The imposed displacement amplitude in all those specimens is equal to ± 200 mm and the pressure level is equal to 32 bar, 70 bar and 120 bar respectively. The ratio of these pressure levels with respect to the nominal yield pressure of the corresponding straight pipe, defined as $P_y = 2\sigma_y t/D$, are equal to 12%, 26% and 45% respectively. The numerical predictions refer to the load-displacement response and to the flattening in the vertical direction, for direct comparison with the test data. The main conclusion from this comparison is that the numerical model can provide accurate predictions of the experimental results. For comparison purposes, the evolution of strain at the critical location of specimen E200-070 is also presented in **Figure 25**c, with respect to the number of cycles.

The effect of internal pressure on the force-displacement response is depicted in **Figure 27**a,b as measured in the experiments and predicted with the finite element model. The results show that internal pressure influences significantly the stiffness of the elbow. This is attributed to the reduction of pipe ovalization caused by the presence of internal pressure, so that the elbow becomes less flexible, exhibiting a "stiffening effect". Finally, the last two columns of **Table 3** summarize the values of strain amplitude $\Delta\varepsilon$ measured experimentally, together with the corresponding numerical predictions. Overall, a very good comparison between test data and numerical predictions is obtained, indicating that the numerical model is capable of representing accurately, not only the overall structural behavior of the elbow (load-displacement response) and the corresponding cross-sectional

ovalization, but also and most importantly, the magnitude of local strain at critical locations and evolution (strain ratcheting) over the loading cycles for both non-pressurized and pressurized elbow.

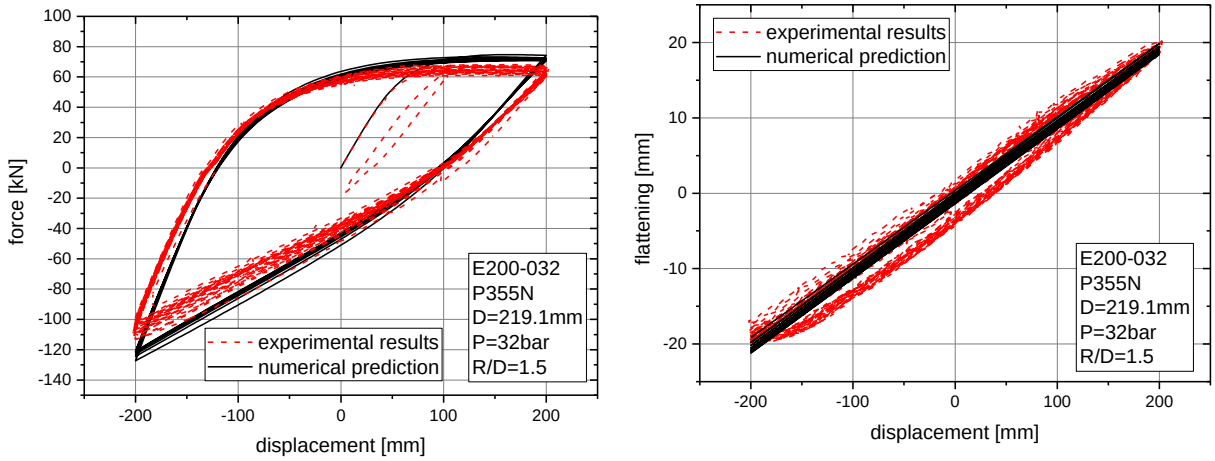

(a) (b)

Figure 24. Comparison between experimental and numerical results [E200-032 specimen]; (a) load-displacement response; (b) elbow flattening.

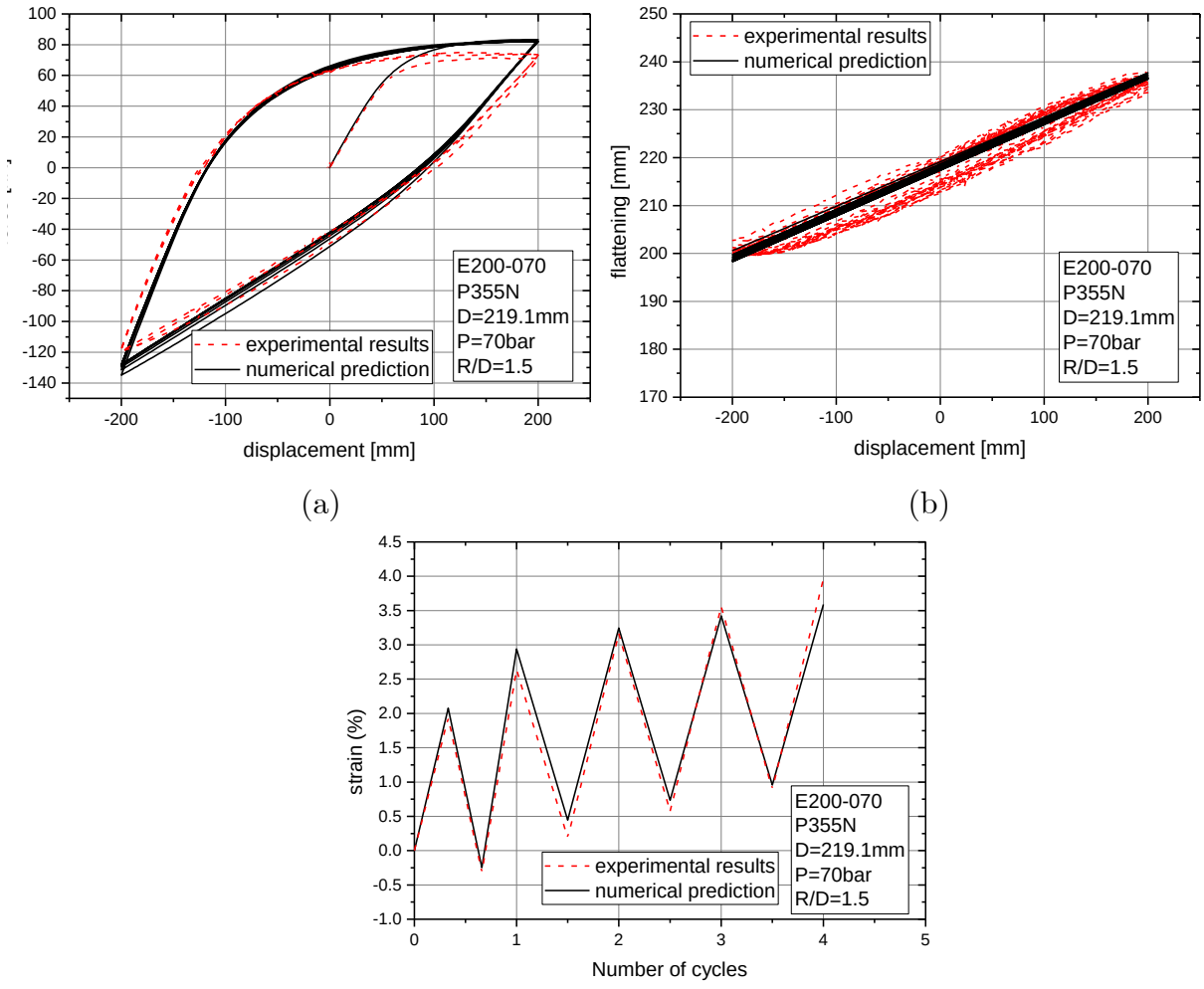

Figure 25. Comparison between experimental and numerical results [E200-070 specimen]; (a) load-displacement response; (b) elbow flattening; (c) evolution of hoop strain at critical elbow location (flank).

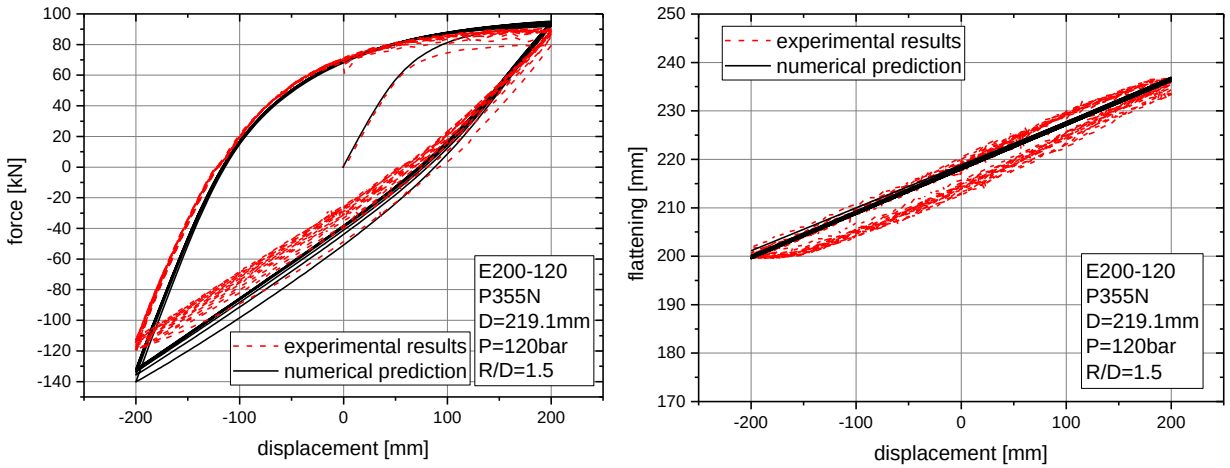

(a) (b)

Figure 26. Comparison between experimental and numerical results [E200-120 specimen]; (a) load-displacement response; (b) elbow flattening.

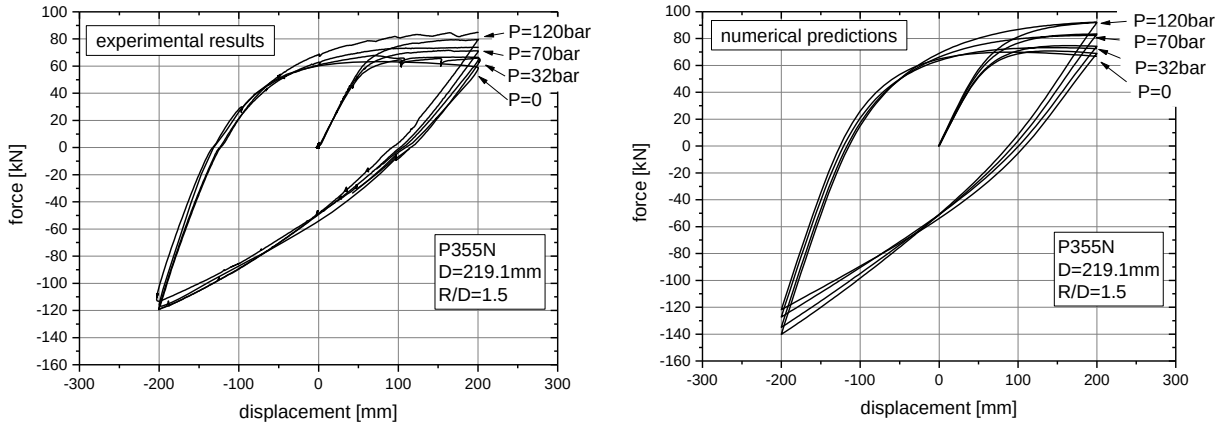

(a) (b)

Figure 27. Effect of internal pressure on force-displacement response during the first loading cycle; (a) experimental results, (b) numerical predictions.

3.5 Influence of internal pressure on elbow response

This section examines the influence of internal pressure on elbow response, using the numerical model validated in section 3.4 against full-scale experimental results. The elbows under consideration in this analysis are 90-degree 8-inch-diameter elbows with R/D equal to 1.5, connected to straight pipe segments in a geometry as presented in **Figure 16**. In the first part of the analysis, a parametric study is presented on the influence of internal pressure on strain evolution for two different amplitude values of imposed

displacement (120mm and 200mm). The finite element model, presented in section 3.4, with elbow thickness equal to 9.88mm is used. In the second part of the study, a parametric analysis considering three different pipe schedules (SCH20, SCH40, SCH60) is presented, so that the effects of the D/t ratio on the mechanical response is identified for different levels of internal pressure. The evolution of strain is examined at three different locations (flank, intrados and extrados of the elbow). In the following, f is defined as the ratio of the applied internal pressure over the nominal yield pressure P_y of each pipe.

The results in **Figure 28** to **Figure 31** refer to the 9.88-mm-thick elbow and show the accumulation of strain at three different locations around the middle cross section of the elbow (flank, intrados and extrados of the elbow) and the evolution of flattening with respect of the number of cycles. The levels of internal pressure under consideration are up to 45% of the P_y value, which is a level very close to the maximum allowable design pressure of the pipe elbow according to ASME B31.3 [61], and the applied displacement amplitude is equal to 200mm. **Figure 28**a shows the hoop strain accumulation at the elbow flank for five levels of pressure, indicating that the maximum and minimum values of hoop strain at this location increase with respect to the number of loading cycles, with increasing level of internal pressure. This is attributed to biaxial ratcheting due to the presence of internal pressure. In **Figure 28**b, the evolution of axial strain at the flack location is depicted. The rate of axial strain accumulation is affected by the level of internal pressure, but the amplitude of axial strain appears to be independent of the pressure level. Comparison between the hoop and the axial strains developed at the flank location shows that the hoop strains are quite higher, justifying the experimental observations that the crack extends along the axial direction of the pipe elbow. In **Figure 29**a the evolution of hoop strain at the elbow extrados is depicted for five levels of internal pressure up to 45% of P_y. The numerical results show that for increasing level of internal pressure, the ratcheting rate also somewhat increases, but the value of strain amplitude is not affected by the level of internal pressure as noted in the previous cases. **Figure 29**b, depicts the axial strain evolution at the elbow extrados. The results indicate that the ratcheting rate may not be affected by the level of internal pressure, while the axial strain amplitude increases with increasing internal pressure. The results in **Figure 30**a show the evolution of strain in the hoop direction at the elbow intrados for the five levels of internal pressure under consideration. These results show that, higher levels of internal pressure increase the ratcheting rate, whereas the corresponding strain range remains unaffected.

In **Figure 30**b, the evolution of axial strain at the same location (intrados) are shown, indicating that the ratcheting rate is unaffected by the level of pressure, and that the effect of pressure level on axial strain range is not significant.

Comparing the value of strain and its evolution at different locations of the elbow it can be concluded that at the flank location the maximum hoop strain, the strain amplitude $\Delta\varepsilon$, and the corresponding ratcheting rate are quite higher than at the other locations. The results also show that the magnitude of axial strains at the flank and at the intrados is similar, but they are smaller than the hoop strain at the flank. Furthermore, the level of strain at the elbow extrados is significantly lower. It is important to notice that the hoop strain amplitude is closely connected to the flattening of cross section. The significant local bending at the flank as shown in **Figure 18** is responsible for the high strain levels at those locations. The presence of internal pressure reduces pipe ovalization and the elbow becomes less flexible, exhibiting a "stiffening effect". **Figure 31**a shows the maximum and minimum values of middle section flattening with respect to the horizontal diameter (**Figure 31**b) in terms of the number of cycles, for different levels of internal pressure. The results indicate that the internal pressure level influences the rate of diameter change, which is consistent with the evolution of strain at flank locations of pressurized elbows. Moreover, the flattening amplitude decreases with increasing internal pressure, which is also consistent with the decrease of strain amplitude observed when the internal pressure increases, as shown in **Figure 28** and **Figure 32**. **Figure 33**a depicts the maximum and minimum values of cross-sectional flattening ΔD_y in the vertical diameter at the middle section of the elbow with respect to the number of cycles, for different levels of internal pressure. The results show that the value of flattening ΔD_y remains nearly constant over the loading cycles. Furthermore, **Figure 34** shows the ovalization of middle cross section at closing bending moment with respect of the number of cycles for internal pressure level equal to zero and to 45% of the yield pressure. The response is reminiscent of the hoop strain evolution at the elbow flank and at the elbow intrados.

The 9.88-mm-thick elbow is also subjected to cyclic displacement equal to $\pm$ 120mm in the presence of three pressure levels (zero, 26%, 45% of P_y). The results in **Figure 35** to **Figure 37** show the evolution of strain at the three different locations under consideration (flank, intrados, extrados) with respect of the loading cycles. The response is analogous to the one observed in the case of ΔL equal to $\pm$ 200mm; in this case though the level of strains is lower lower. **Figure 38** shows the evolution of maximum and minimum hoop

strain with respect of the number of cycles for the two amplitudes of applied displacement examined. The results show that as the applied displacement increases, the level of the corresponding hoop strain increases.

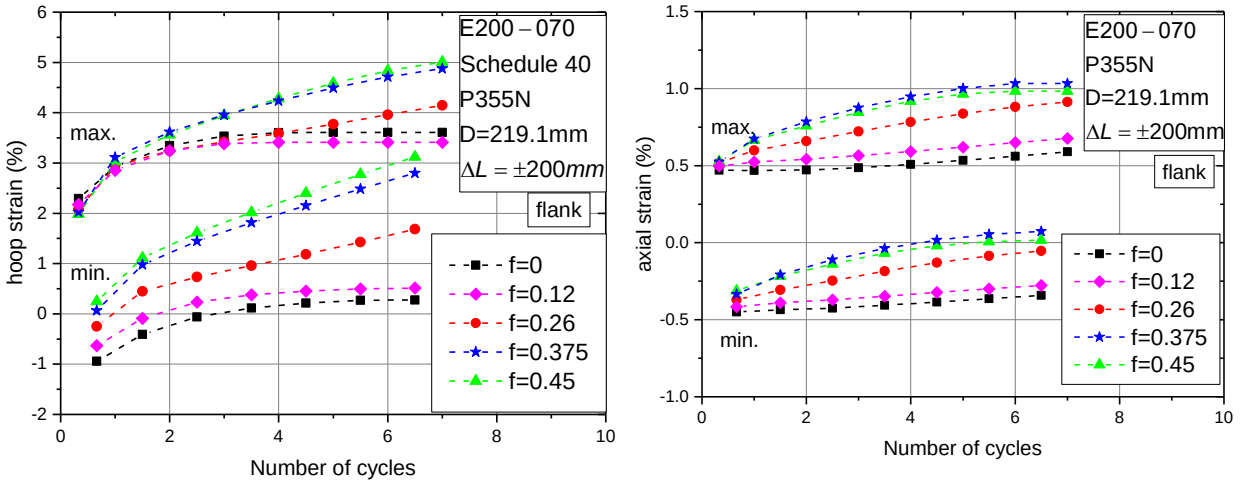

(a) (b)

Figure 28. Evolution of maximum and minimum strain at the elbow flank [SCH 40]; (a) hoop strain, (b) axial strain.

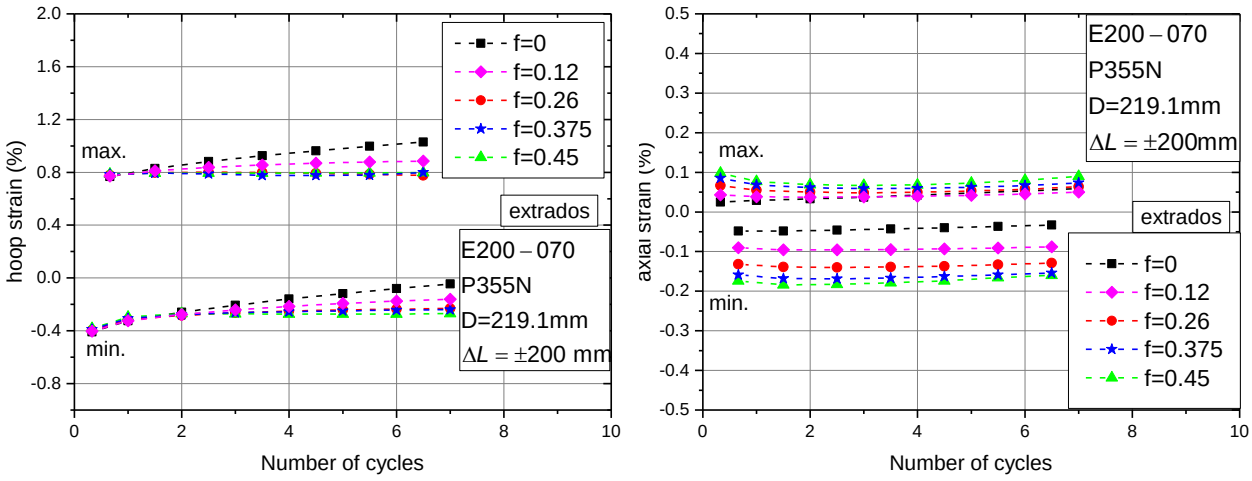

(a) (b)

Figure 29. Evolution of maximum and minimum strain at the elbow extrados [SCH 40]; (a) hoop strain, (b) axial strain.

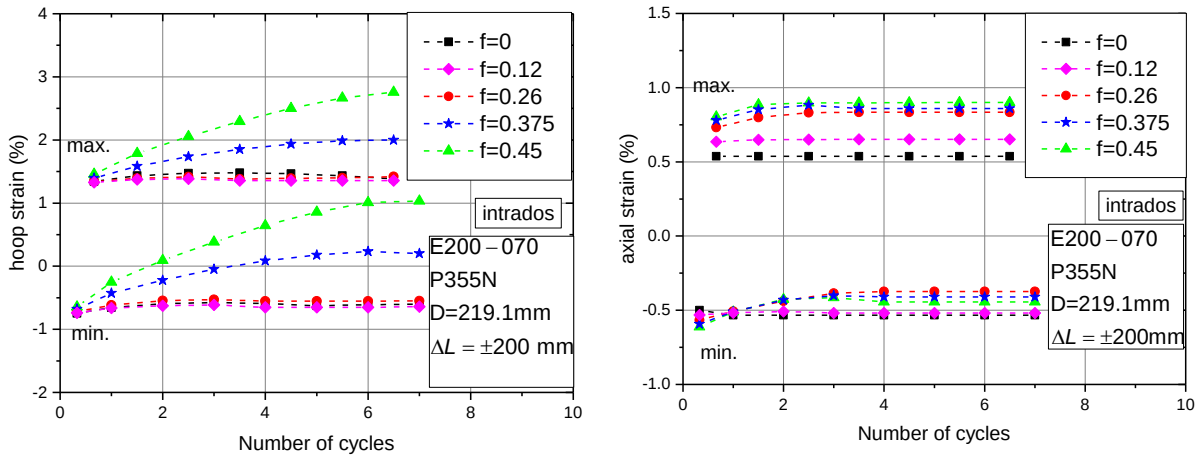

(a) (b)

Figure 30. Evolution of maximum and minimum strain at elbow intrados [SCH 40]; (a) hoop strain, (b) axial strain.

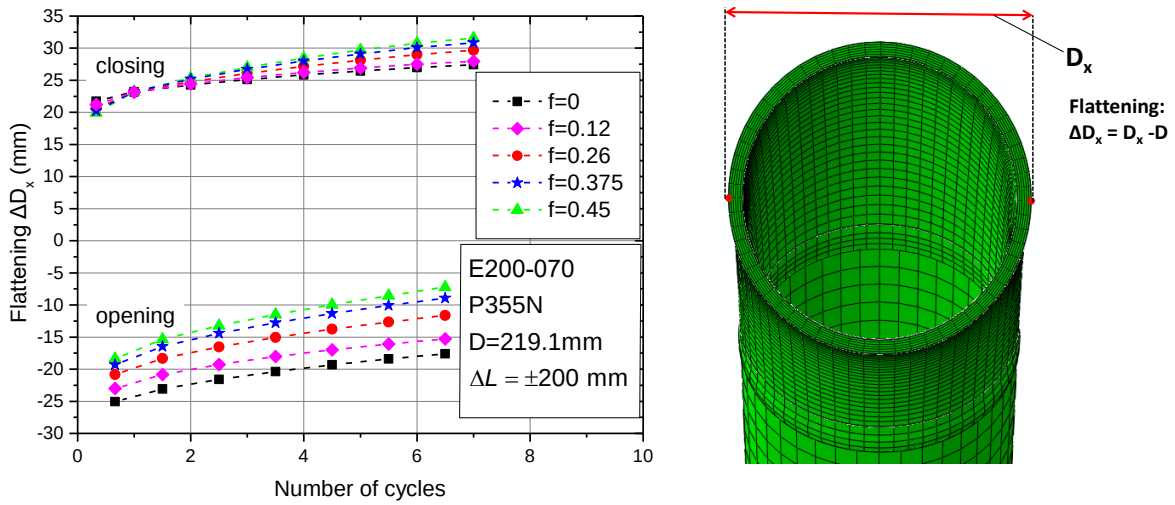

(a) (b)

Figure 31. (a) Evolution of maximum and minimum flattening ΔD_x for different pressure levels [SCH 40 elbow]; (b) flattening definition ΔD_x.

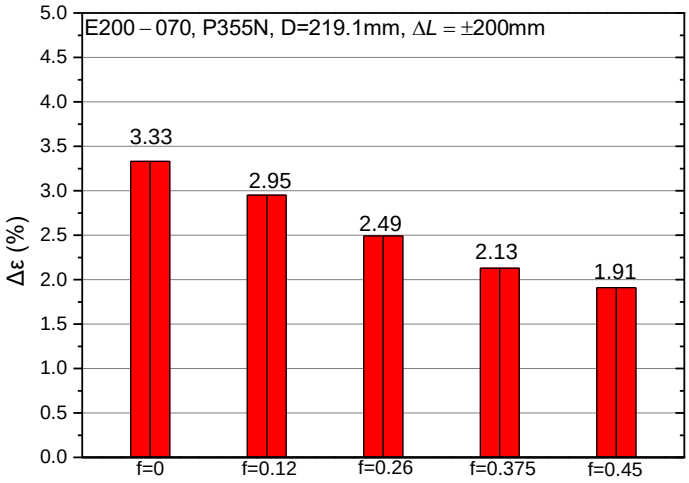

Figure 32. Hoop strain amplitude for different levels of pressure [SCH 40].

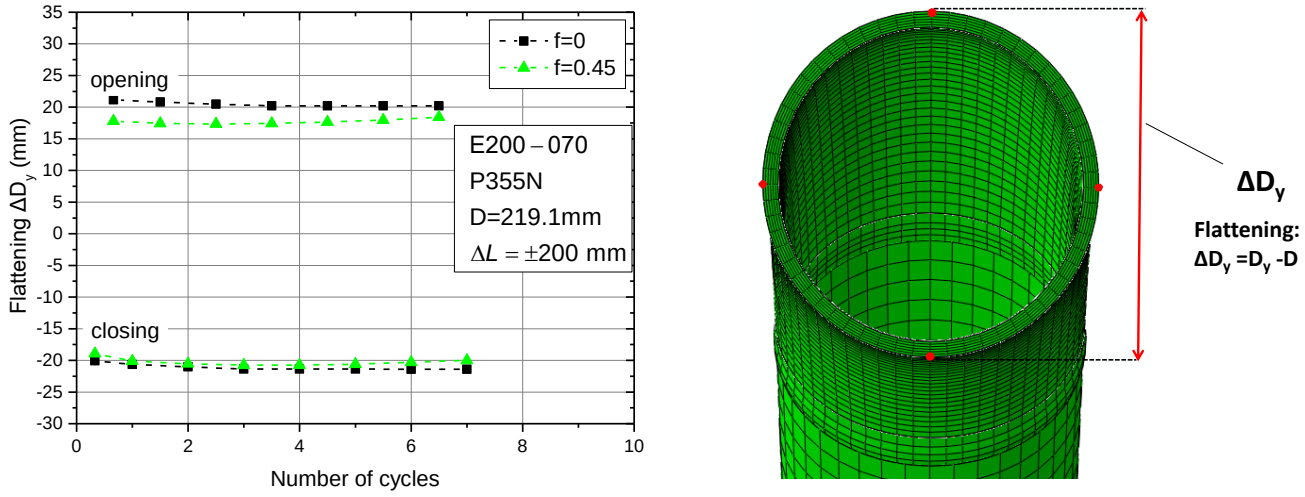

(a) (b)

Figure 33. (a) Evolution of maximum and minimum flattening ΔD_y for different pressure levels [SCH 40]; (b) flattening definition ΔD_y.

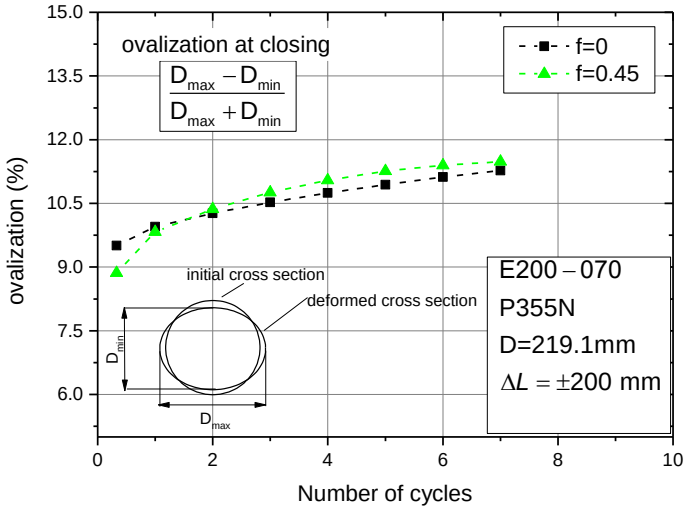

Figure 34. Evolution of cross-sectional ovalization for different pressure levels [SCH 40].

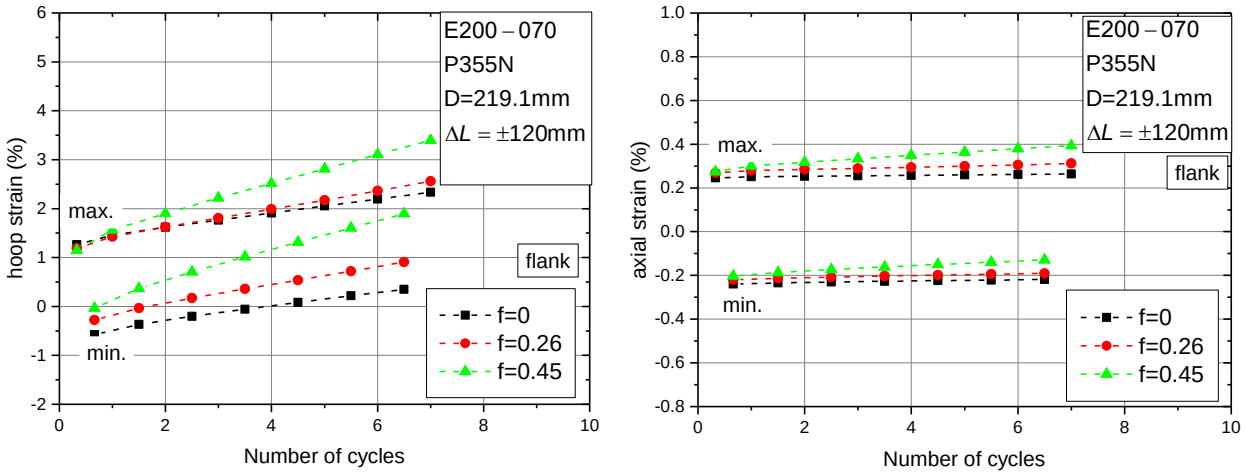

(a) (b)

Figure 35. Evolution of maximum and minimum strain at the elbow flank [SCH 40]; (a) hoop strain, (b) axial strain.

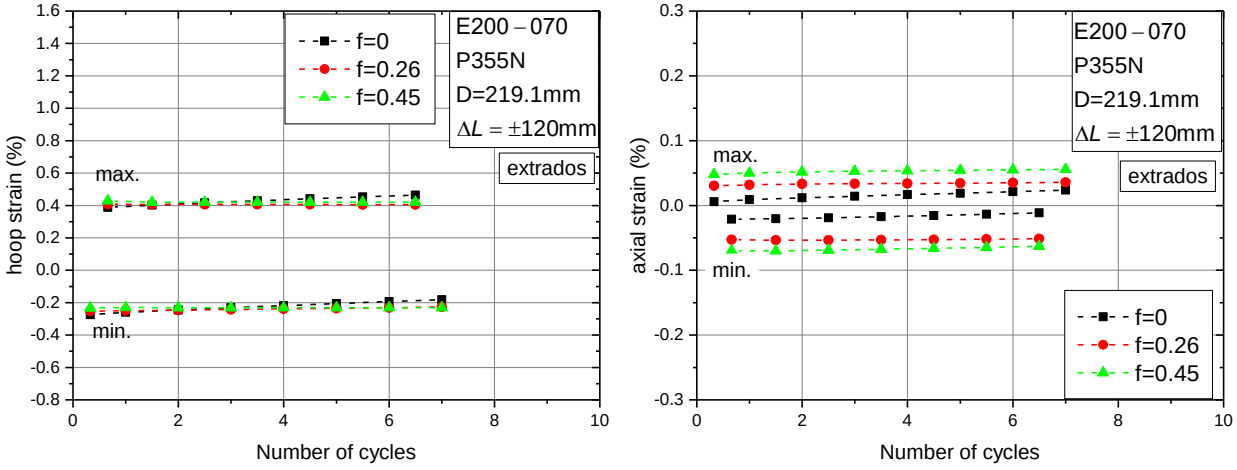

(a) (b)

Figure 36. Evolution of maximum and minimum strain at the elbow extrados [SCH 40]; (a) hoop strain, (b) axial strain.

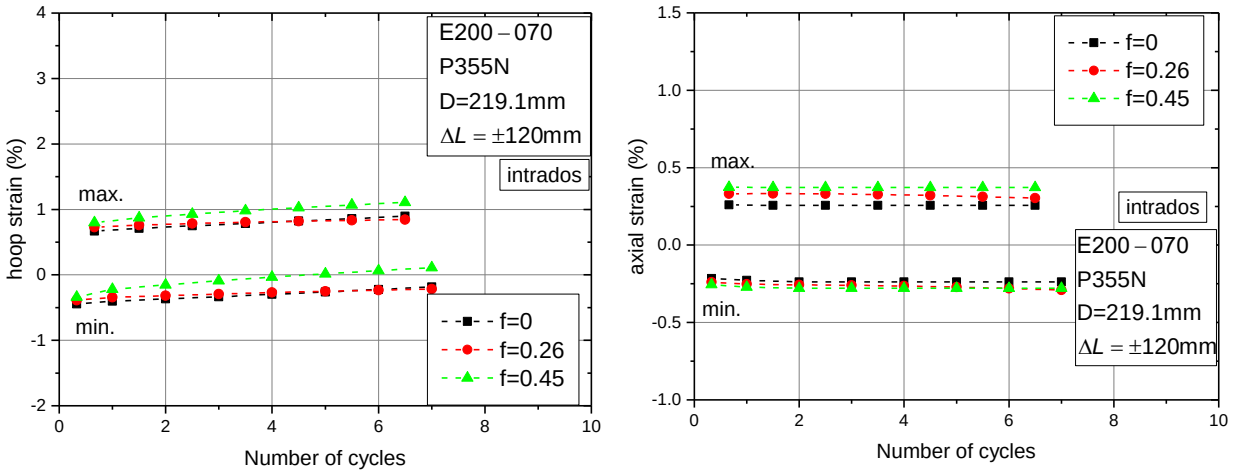

(a) (b)

Figure 37. Evolution of maximum and minimum strain at the elbow intrados [SCH 40]; (a) hoop strain, (b) axial strain.

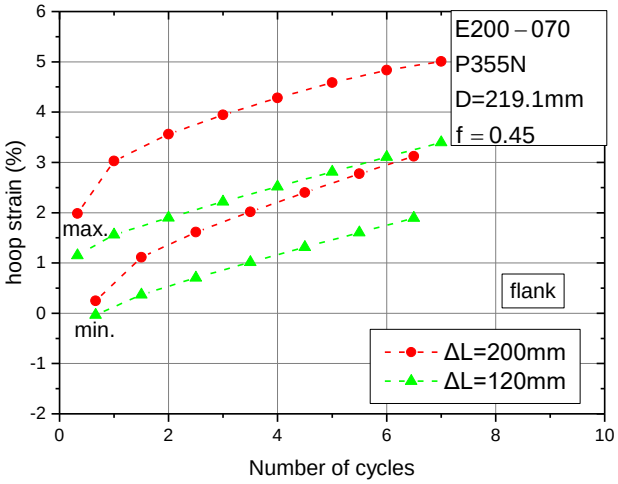

Figure 38. Evolution of maximum and minimum hoop strain at the elbow flank [SCH 40]; imposed displacement ΔL equal to ± 120 and ± 200.

In the second part of this section, the effect of pipe thickness on the elbow response is examined, considering three different pipe schedules. More specifically, the 8-inch-diameter assembly of **Figure 16** is considered with the nominal thickness of SCH60, SCH40, SCH20 according to ASME/ANSI B36.10M. For the SCH60, thickness is equal to 10.31mm, for SCH40 is equal to 8.18mm and for SCH20 the thickness is equal to 6.35mm. All other geometric and material parameters of the numerical model are the same. The applied displacement is equal to ± 120mm, and the level of internal pressure is considered equal to zero, 22.5%, and 45% of the yield pressure. The results for local strains developed at the three characteristic locations show similar trends observed in the corresponding results for the SCH40 pipe presented before. The strain results at the flank are depicted in **Figure 39**-**Figure 41**, which is the critical location of all three elbows. The results show that the hoop strains at the flank and their ratcheting rate are higher than the corresponding axial strains.

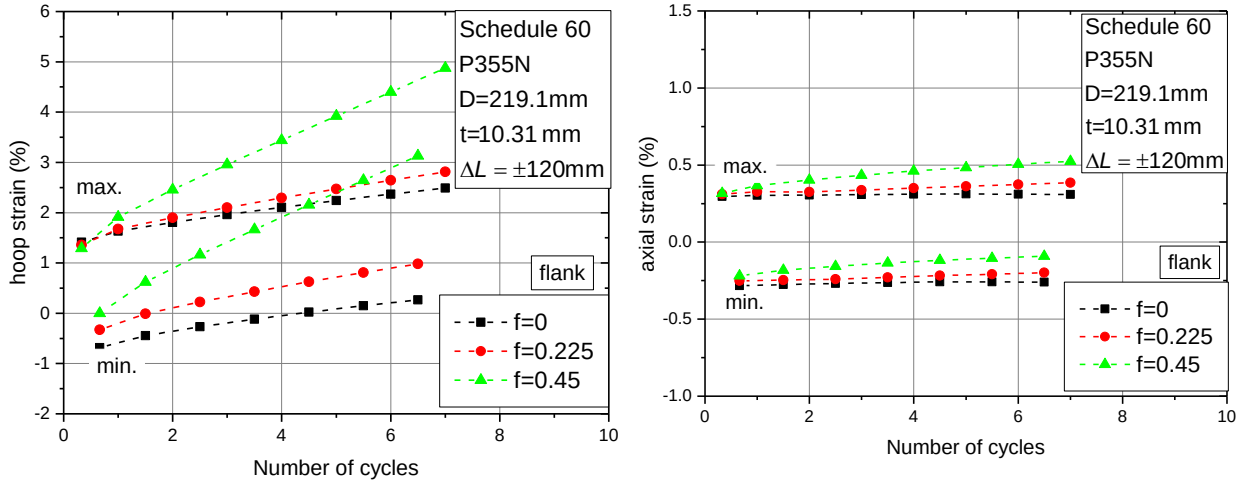

(a) (b)

Figure 39. Evolution of maximum and minimum strain at the elbow flank [SCH 60]; (a) hoop strain, (b) axial strain.

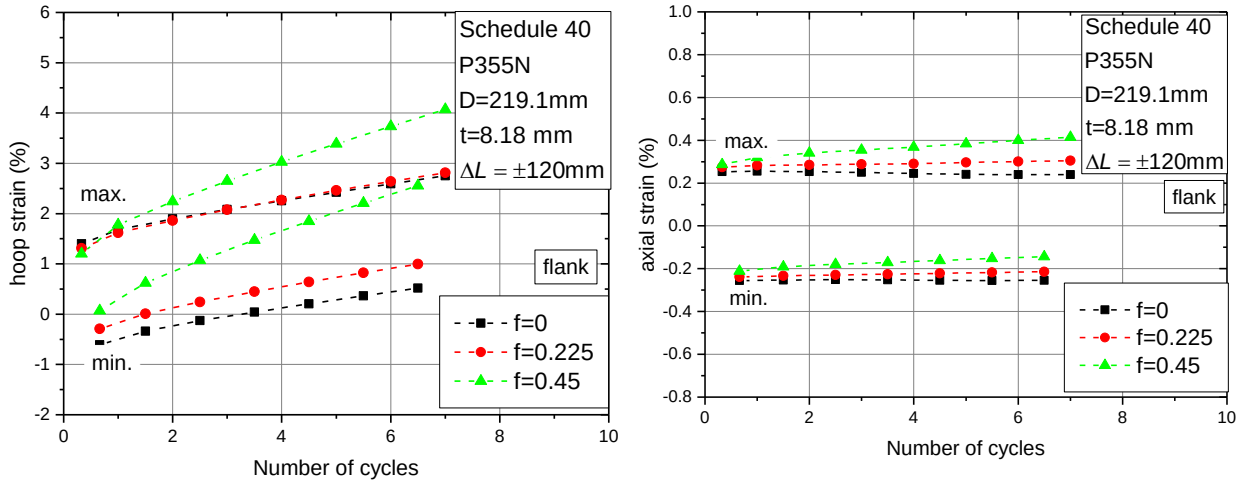

(a) (b)

Figure 40. Evolution of maximum and minimum strain at the elbow flank [SCH 40]; (a) hoop strain, (b) axial strain.

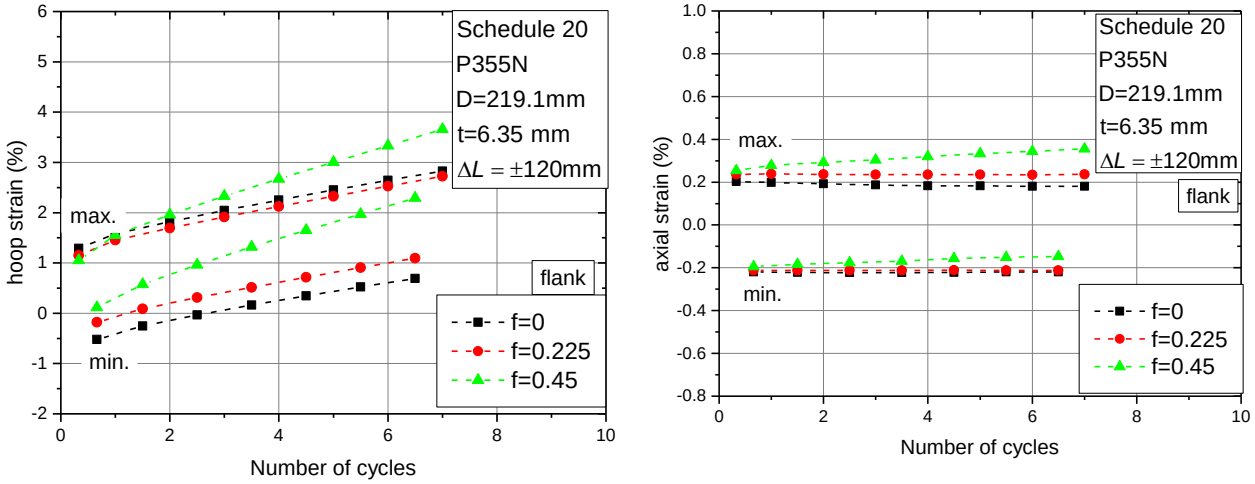

Figure 41. Evolution of maximum and minimum strain at the elbow flank [SCH 20]; (a) hoop strain, (b) axial strain.

Comparison of hoop strain amplitude and evolution at the flank location for the three schedules is performed for three pressure levels: (a) zero internal pressure [case A]; (b) internal pressure equal to 90 bar same for all schedules [case B], (c) internal pressure equal to 45% of the yield pressure P_y of each schedule [case C]. In case B, expressing the pressure in normalized form, the ratio of 90 bar with respect to the yield pressure P_y of each pipe schedule is equal to 44%, 34% and 27% for SCH20, SCH40, SCH60 respectively. The results for all cases are presented in **Figure 42** and **Figure 43**. In the absence of internal pressure, the amplitude of strain ($\Delta\varepsilon$) and the maximum strain somewhat increase with decreasing elbow thickness. For case B the results show that value of f influences elbow response. In this case the amplitude of hoop strain decreases as the elbow thickness decreases, and this is attributed to the increase of f when the thickness increases. Furthermore, in case B the maximum strain increases with decreasing thickness. On the other hand, in case C both the amplitude of strain ($\Delta\varepsilon$) and the maximum strain increases with increasing pipe thickness.

The numerical results presented above are consistent with the main observations presented in the recent paper by Hassan *et al.* [16], despite the fact that the results in that study refer to elbows of different size. In particular, there is a good agreement on the trend of strain evolution at the three elbow locations under consideration, i.e. flank, intrados and extrados.

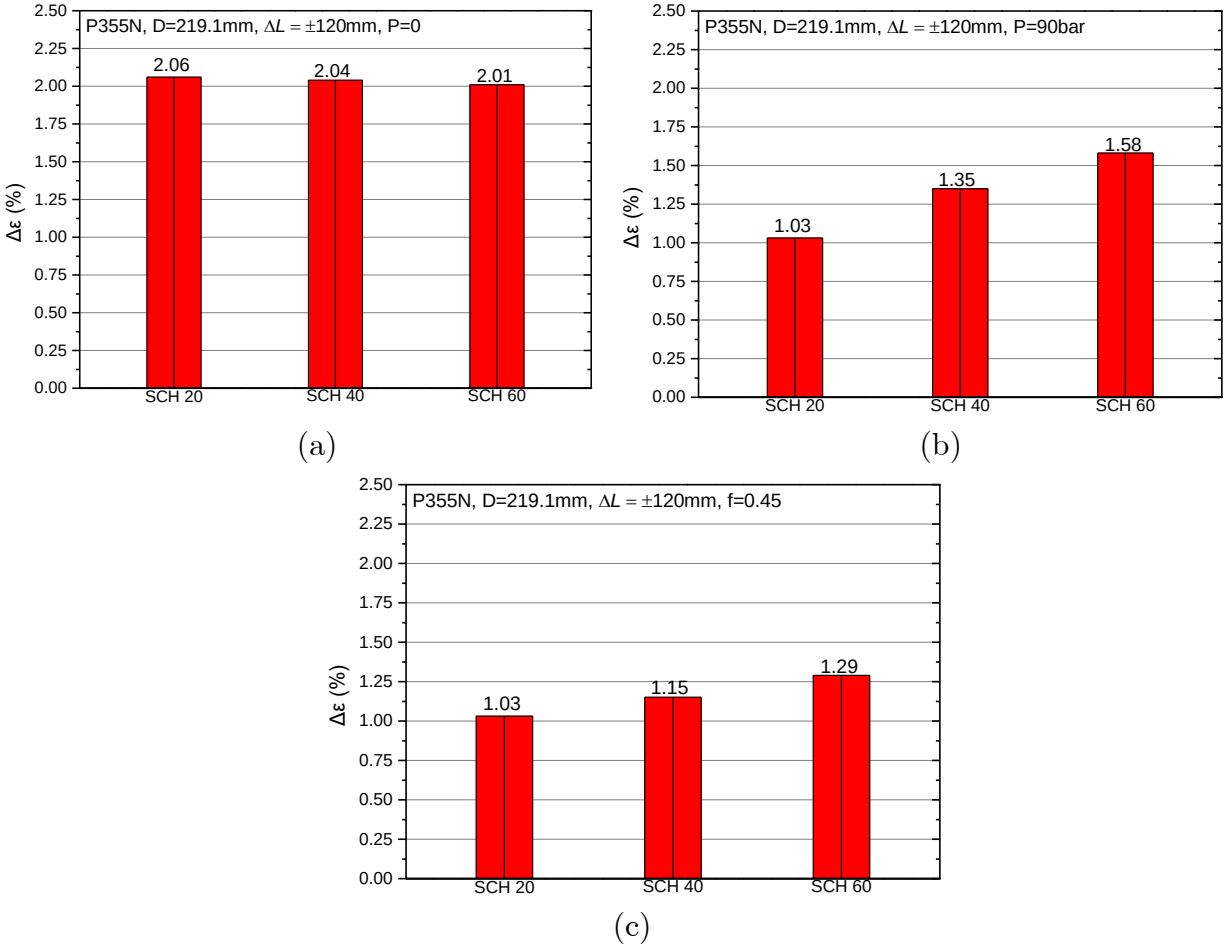

Figure 42. Hoop strain amplitude for different schedules for ΔL=120mm; (a) zero pressure, (b) pressure P=90bar.

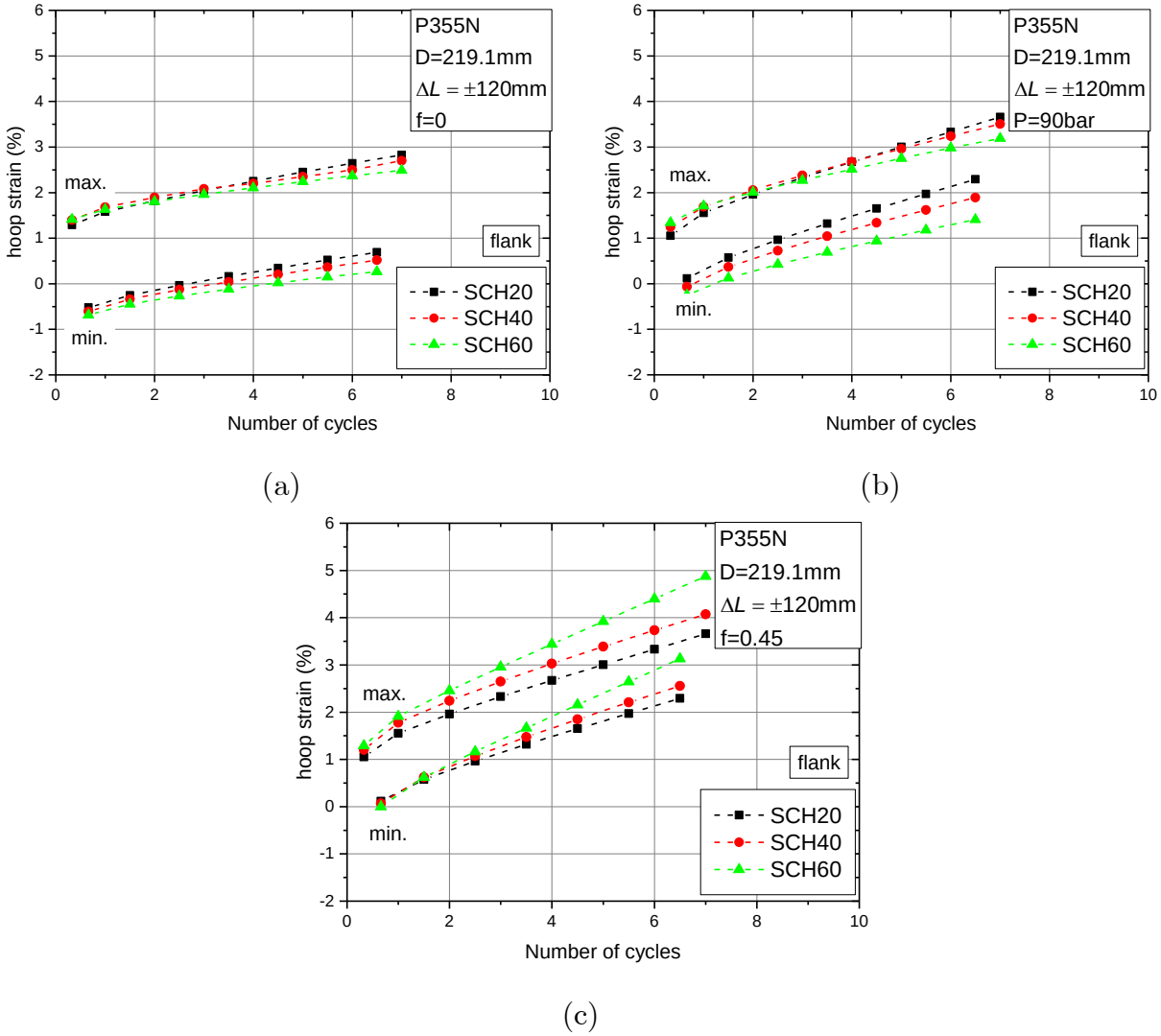

Figure 43. Evolution of hoop strain at elbow flank for SCH20, SCH40, SCH60.

3.6 Conclusions

A numerical simulation of steel piping elbow performance, subjected to strong cyclic loading conditions, has been presented in this Chapter 3. The elbows have been modeled rigorously using nonlinear finite elements and the cyclic-plasticity material model based on the bounding-surface concept presented in Chapter 2. The work is supported by experimental data on elbow specimens subjected to in-plane cyclic bending, under several levels of internal pressure. The constitutive model has been calibrated using small-scale strain-controlled and stress-controlled material tests from strip specimens extracted from elbows fabricated from the same heat. Using the calibrated material parameters, the experimental results of large-scale laboratory tests have been simulated accurately and very good predictions on the value of local strain and its accumulation over the loading cycles at the critical elbow location were obtained. This very good comparison between experimental and numerical results demonstrates the capability of the constitutive model under consideration in predicting the inelastic response of steel piping components under strong cyclic loading and the rate of strain ratcheting, as well as its suitability for large-scale computations.

In the second part of the chapter, an extensive analysis is performed in order to elucidate the effect of internal pressure on elbow response with emphasis on local strain accumulation at different elbow locations. It was concluded that for all cases examined the flank location is critical in terms of maximum strain value and its evolution rate. Furthermore, at the flank position, the hoop strain range is higher than the corresponding axial strain range and the ratcheting rate at hoop direction is also higher than ratcheting rate in axial direction, which is consistent with the location and orientation of failure pattern observed experimentally. The results also indicate that the amplitude of axial strain at the flank and the intrados is similar, while the strain level at the elbow extrados is significantly lower. Moreover, the results show that as the level of internal pressure increases the ratcheting rate increases and the strain amplitude decreases. The trend of the results from the present study compares very well with numerical results, reported in other publications, in particular, there is a good agreement on the observations for strain evolution at the three elbow locations under consideration (flank, intrados and extrados). Finally, considering three different pipe schedules, the effect of elbow thickness on the ratcheting rate and on strain amplitude has been investigated. The results indicate that

for the case with zero internal pressure the effect of thickness on the ratcheting rate is negligible, while for the case of internally-pressurized elbows this effect is more pronounced.

Chapter 4 - Low-Cycle Fatigue of Fillet-Welded Steel Plate Connections

The mechanical behavior of fillet-welded steel joints is examined in this chapter. It is motivated by the seismic response of unanchored steel tanks that exhibit repeated uplifting of the base plate, leading to low-cycle fatigue failure of the fillet-welded connection of the tank base plate with the tank shell, due to repeated inelastic deformation. Low-cycle fatigue experiments on small-scale fillet-welded joints are performed, representing the connection of the base plate with the tank shell. Material tests have been conducted prior to fatigue tests, to identify the mechanical properties of the base plate material, whereas the weld is examined with stereo optical microscopy and micro-hardness measurements. The fatigue experiments aim at determining the relationship between the strain developed at the welded connection and the corresponding number of cycles to failure. Inspection of the failed specimens has determined the "zone" size at the upper/bottom surface in which microcracks occurred. Numerical simulations are also performed, to elucidate special features of joint behavior, complementing the experimental results and observations. The main conclusion is that the fillet-welded connections under consideration are capable of sustaining substantial strain levels for a significant number of cycles, before low-cycle fatigue failure occurs. Furthermore, a strain-based fatigue curve is developed, which can be used for the seismic design of liquid storage tanks.

4.1 Introduction

Fillet-welded plate connections constitute a quick and efficient method to tie steel plates and are widely used in civil engineering applications, such as buildings or bridges, as well as in marine structural systems such as stiffeners in ships and other floating systemes. In several cases, those welded connections are subjected to repeated, loading which may lead to fatigue failure. Most fatigue failures have been documented in the high-cycle fatigue regime, associated with a large number of cycles, as documented in the review paper by Maddox [92]. However, under extreme loading conditions, large elastic–plastic strains may develop, characterized by repeated excursions in the inelastic range of the material, causing low-cycle fatigue, under a relatively low number of load cycles. Schjødt-

Thomsen and Andreasen [93] have investigated the low-cycle fatigue of fillet welds made of high-strength weldable steel and concluded that the ultimate tensile strength may be used as the basis for developing fatigue curves from static material data. Corigliano *et al.* [94] reported experimental and numerical investigation of fillet-welded joints under low-cycle fatigue loading, providing information for the development of models, and according to experimental observations they have noticed that the region with critical strains extends at the base-material surface. In a subsequent publication, Corigliano *et al.* [95] employed a notch-strain approach to predict the low-cycle fatigue life of fillet welded joints used in ship structures.

Another, more specific application of fillet welds refers to unanchored liquid storage tanks and, in particular, to the connection of the tank base plate with the tank shell. When an unanchored tank is subjected to strong seismic motion, the overturning moment, caused mainly, by the oscillating liquid containment, and the relevant hydrodynamic pressure on the tank wall may cause repeated uplift of the tank base plate [96] [97]. The base plate is significantly thinner than the tank shell, and this repeated uplifting may lead to low-cycle fatigue. The early publication by Wozniak and Mitchell [98] proposed a beam-strip model that describes the uplifting mechanism, with emphasis on the plastic deformation of the base plate. A more elaborate analytical uplifting model has been proposed by Leon and Kausel [99], whereas Fischer *et al.* [100], motivated by tank uplifting, has revisited the uplifting behavior of an elastic beam subjected to the simultaneous action of an end-upward force and a uniformly-distributed load. In more recent publications, Malhotra and Veletsos presented a beam-strip model [101], and an axisymmetric model [102], in an attempt to describe the uplifting mechanism and the relevant deformation of the base plate. These models have constituted the basis of a global model for the dynamic response of an uplifting tank, presented in a subsequent publication of Malhotra and Veletsos [103]. Recently, Bohra *et al.* [104] and Spritzer and Guzey [105] investigated the response of liquid storage tank subjected to seismic loading and compared the uplifting amplitude of the tank structure with available design standards. Furthermore, Taniguchi *et al.* [106] calculated the uplifting displacement using a simplified analysis and compared the results with measurements from tank pulling-out length of anchor bolt of an anchored tank. In most of the above publications, the welded connection between the unanchored tank shell and the base plate has been identified as the critical location during uplifting, where maximum plastic deformation occurs, as shown

schematically in **Figure 44**. Therefore, in the case of severe seismic action with repeated uplifting, this connection would be subjected to several cycles of inelastic deformation of alternate sign, leading to possible failure in the form of low-cycle fatigue cracking.

The present study is motivated by the mechanical response of fillet-welded base-plate-to-tank-wall connection in unanchored liquid storage tanks subjected to seismic loading. Recently, the low-cycle fatigue of this fillet-welded connection has been examined experimentally by Cortes *et al.* [107], through a series of tests on medium-scale plated welded joint, representing the base plate to tank shell connection. Experimental results have been presented in terms of plastic rotation of the connection an approach also adopted in the provisions of two relevant design documents, namely the European standard EN 1998-4 [108] and the New Zealand design recommendations NZSEE [109]. The main finding from the experimental investigation of Cortes *et al.* [107], is that the deformation limits proposed in EN 1998-4 [108] and in the NZSEE [109], in terms of plastic rotation of the connection, are conservative. More recently, Prinz and Nussbaumer [110] reported an analytical work on the fatigue behavior of liquid-storage tanks with emphasis on shell-to-base plate connections. They used the test results from [107] to validate their models, examined the effects of base-plate radial tension, and also concluded that the rotation capacity of the connection can be quite larger than the one described in [108] [109]. In a subsequent publication, Prinz and Nussbaumer [111] reported a series of additional experiments on the low-cycle fatigue capacity of the shell-to-base connection, aimed at expanding the research findings of Cortes *et al.* [107], and concluded that the fatigue fracture originated in the base material away from the weld heat affected zone. Furthermore, they verified the argument that the rotation capacity of the fillet-welded connection is larger than the one specified by current code limits. More recently, Prinz and Nussbaumer [112] investigated experimentally the effects of the radial base-plate welds on the fatigue capacity of tank shell-to-base connections during uplift. Despite the influence of the radial weld on the base-plate ductility of the fillet welded connection, all tested joints indicated a fatigue resistance far greater than the current deformation limit stated in [108] and [109].

However the good performance of the fillet welded, noticed in previous publications [107] [110] [111], with respect to the provisions of the available design documents [108] [109]. It may not be possible for a directly relation of the reported experimental results with tank uplifting in a real seismic event, since the reported rotation is a “global”

measure of deformation, and it depends on the experimental set-up and cannot describe tank uplifting in a reliable manner. On the other hand, a strain-based approach, considering the local strain developed at the base plated at the vicinity of the weld toe, offers a more "universal" approach, which can be directly used in a fatigue assessment of the connection in the course of a seismic analysis of uplifting tanks. Such an analysis is described in detail by Vathi and Karamanos [113].

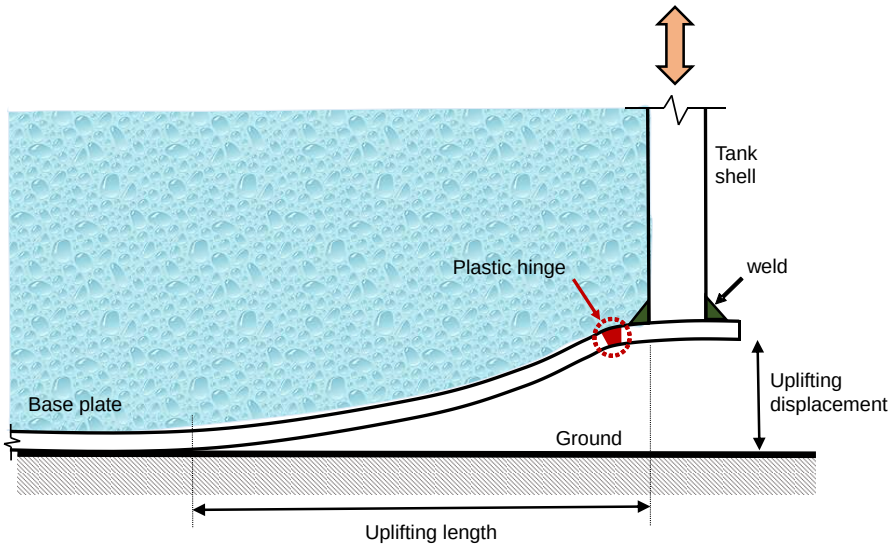

Figure 44. Schematic representation of uplifting mechanism in unanchored liquid storage tanks; fillet welded connection may fail due to low-cycle fatigue that may occur at the weld toe of the connection.

4.2 Specimens, experimental set-up and instrumentation

Eight (8) tests on welded shell-to-base connections have been performed to examine their behavior under low-cycle fatigue. The experiments have been conducted at the Laboratory of Mechanics and Strength of Materials at the University of Thessaly. The dimensions of the L-joint welded specimens were selected considering a typical liquid storage tank, made of S275J2 steel grade for the base plate and S355J2 for the shell plate [114]. The diameter of the tank is equal to 54.864m and the total height of the tank shell is equal to 15.6m. The tank has been designed according to EN14015 standard [115], resulting to a base plate of 8 mm and bottom shell plate thickness 30mm, whereas the fillet weld throat at the base plate-to shell connection is 5.6mm. The specimens have been

extracted from large-scale 500-mm-wide welded connections shown in **Figure 45**, which have been manufactured exactly as in real tank application. It is also noted that a series of those 500-mm-wide specimens have also been tested under repeating loading conditions, as described in [116]. Each specimen is 25-mm-wide consisting of a 8-mm-thick steel strip (representing the tank base plate), fillet-welded to a 30-mm-thick strip (representing the tank shell plate), and is subjected to repeated constant-amplitude uplift displacement, using a special-purpose experimental set-up shown in **Figure 46**. The set-up consists of the following parts: part A, which represents the ground, part B, which is a fixed support that allows for gradual bending of the base-plate, and part C, which has been used for applying load on the specimen. The total load capacity of the actuator is equal to 100 kN.

Figure 45. General view of a typical specimen, extracted from the large-scale welds.

Displacement-controlled repeated loading on the L-joint specimens have been performed by applying an upward displacement at Part C as shown in **Figure 46**a, while Part A remains fixed and represents the ground surface, while part B also remains fixed imposing the same boundary condition of the uplifting tank strip. Strain gauges have been attached close to weld region to measure local strains. In **Figure 47** representative specimens with the attached strain gauges are depicted. The locations of the strain gauges

have been selected according to the estimated level of strain, given the fact that the laboratory data acquisition system is capable of measuring up to 6% strain. **Figure 46**b depicts the deformed shapes of the specimen, whereas **Table 4** presents an overview of the testing program. In addition to strains, an important parameter monitored during experiments is the rotation θ, also measured in previous experimental studies [107]-[111]. **Figure 48** demonstrates the calculation of rotation θ in the present study, and its value is presented in **Table 4**, where l_0 is the length of the "base" plate subjected to bending.

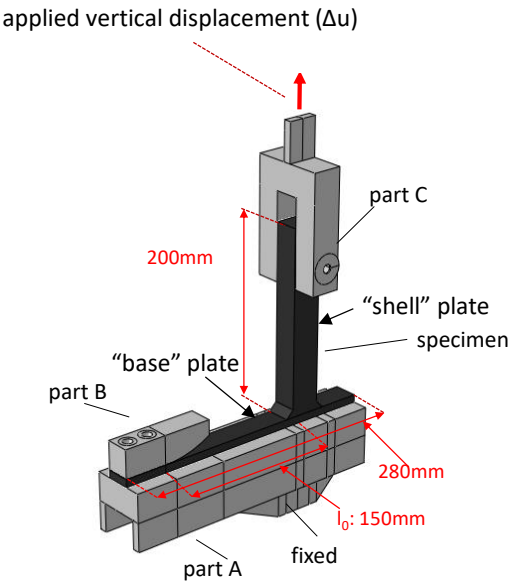

. (a)

(b)

Figure 46. Experimental setup: (a) specimen part and experimental set-up; (b) deformed specimen at uplifting (Δu) is equal to 35mm.

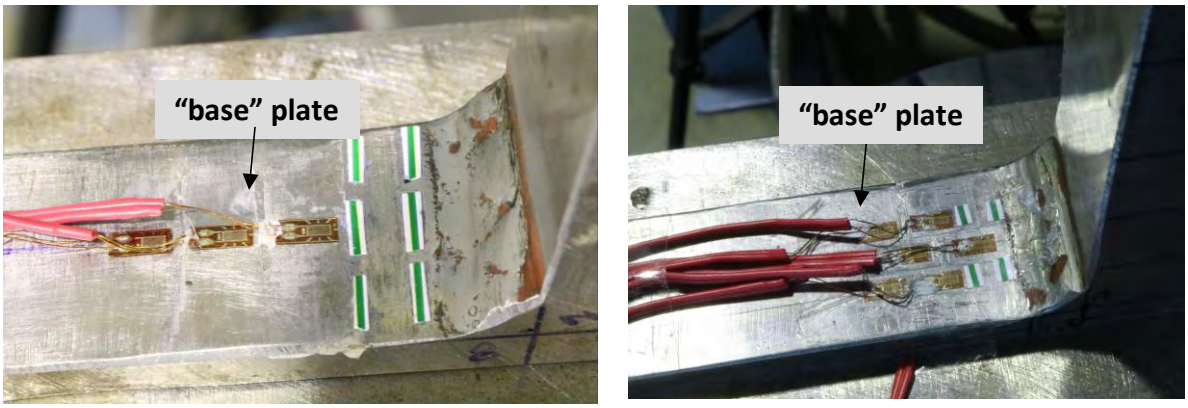

Figure 47. Instrumentation of test specimens with strain gauges at the vicinity of the weld.

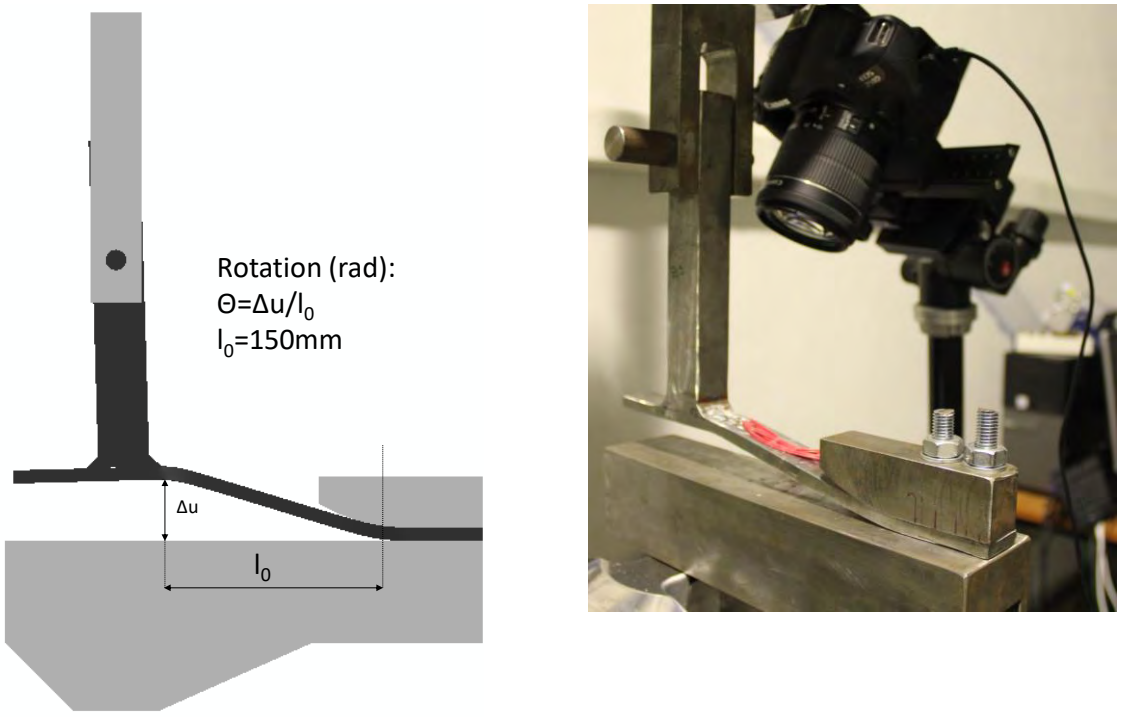

(a) (b)

Figure 48. (a) Definition of the "uplifting rotation" θ; (b) experimental set-up for time-laps acquisition.

Table 4. Summary of experimental results on fillet-welded connections.

specimen	Displacement Δu (mm)	Rotation θ (rad)	Peak load (KN)	N_1	N_{20}	N_f
B2	25.0	0.17	3.19	65	121	139
B5	27.5	0.19	3.34	7	57	70
B1	30.0	0.20	3.45	33	89	96
B3	32.5	0.22	3.77	22	76	92
A3	35.0	0.24	3.41	24	51	54
A4	35.0	0.24	3.65	24	57	65
A5	37.5	0.26	3.96	1	24	31
A2	40.0	0.27	3.82	3	34	36

Material tests have been performed in order to determine the material properties of the base plate. In **Figure 49**, tensile and cyclic material stress-strain curves are depicted. The two cyclic tests were performed under strain-controlled conditions at 1% and 2%

respectively. The yield stress of the base plate is equal to 340 MPa and the tensile strength is equal to 475 MPa.

Metallographic analysis was performed on selected transverse cross sections of the L-joints before testing. Specimen preparation included cutting with Struers ‘‘Accutom 2’’, grinding with SiC papers 120, 320, 500, 800 and 1000 grit, polishing with diamond paste of 3 and 1 μm diameter, followed by etching with a solution of 30% HNO3 in distilled water for the macrostructure and with Nital 3% for the microstructure. A typical weld macrostructure is shown in **Figure 50**, where the weld metal (WM), the Heat affected Zone (HAZ) and the base metal (BM) are highlighted. The weld appeared free of macro-defects, showing a smooth transition from the WM to the HAZ and the BM. The microstructure of each area is depicted in **Figure 51**. The BM consists of a banded ferrite and pearlite microstructure, the WM consists of “widmanstätten” and acicular ferrite along with carbides. In the HAZ (heat-affected-zone) the grain growth area exists next to the WM (weld-metal), while near the BM (base-metal) the fully grain refinement area is observed.

Microhardness measurements have been performed in two of the metallographic specimens according to EN 1043-1 standard [117], using a load of 2 kgf on Vickers scale, and the results are presented in **Table 5**. All hardness measurements are within the range of 160-452HV2. The higher values were measured in the coarse grain size HAZ3 located next to the WM.

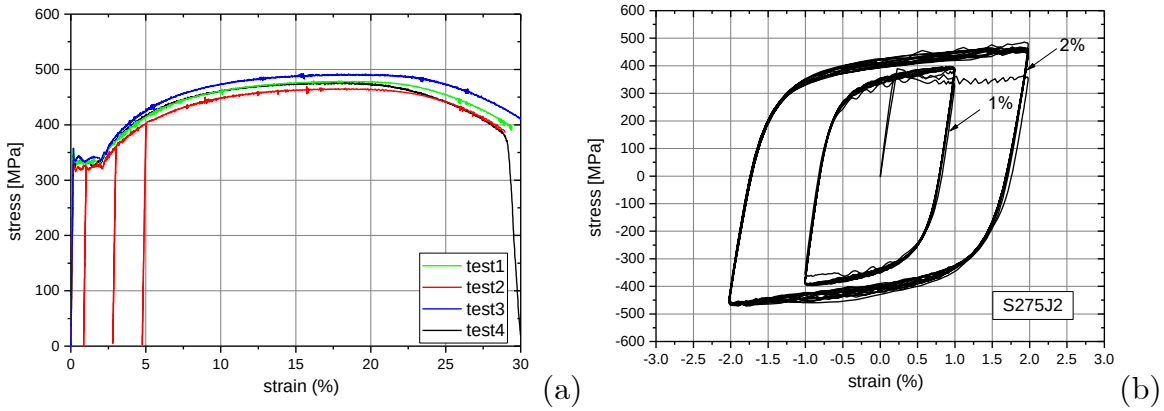

Figure 49. Stress-strain curves for S275J2 steel grade; uniaxial tests on steal strips extracted from the base plate: (a) monotonic tests; and (b) cyclic tests.

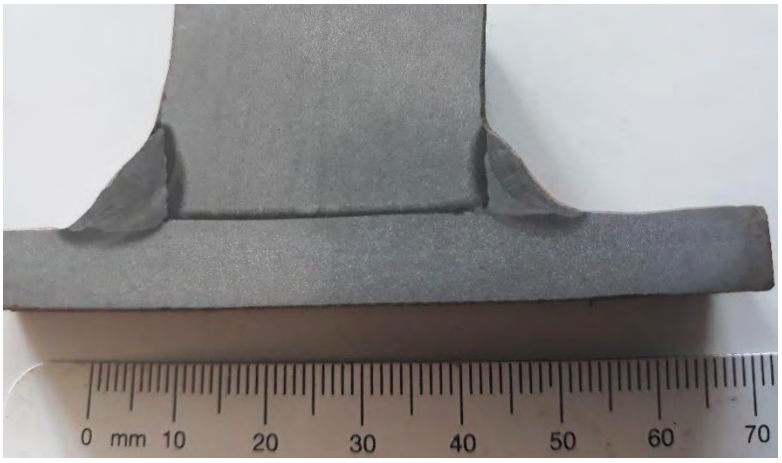

(a)

(b)

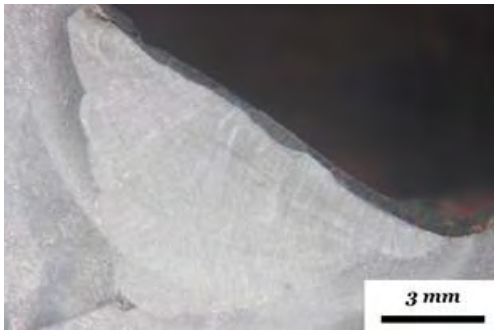

(c)

Figure 50. (a) Macrostructure of a typical L-joint welded specimen; (b), (c) detail the macrostructure, showing the WM, HAZ and BM.

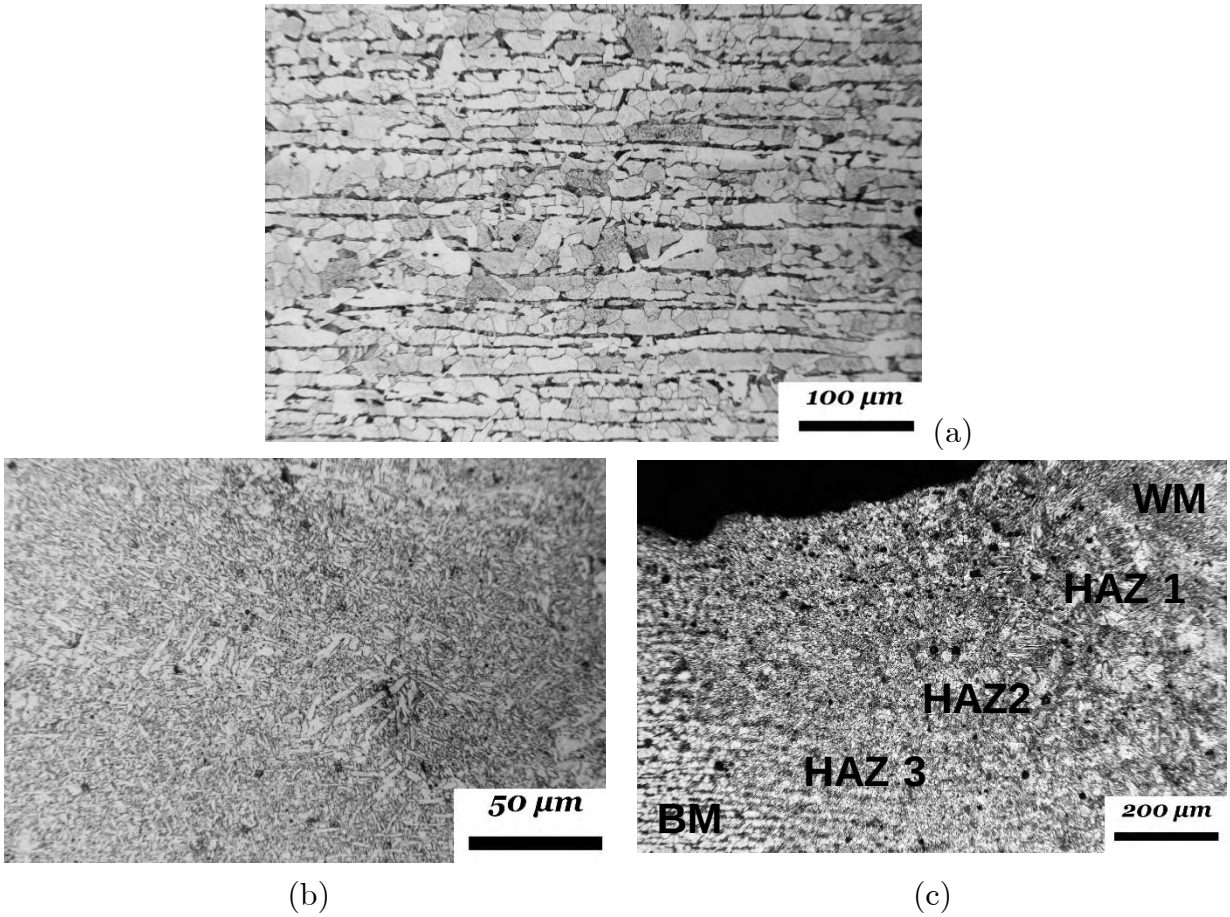

Figure 51. Microstructure of (a) BM, (b) WM, (c) HAZ at the weld toe: coarse grain (HAZ1), partial grain refinement in HAZ2, and fully grain refinement in HAZ3.

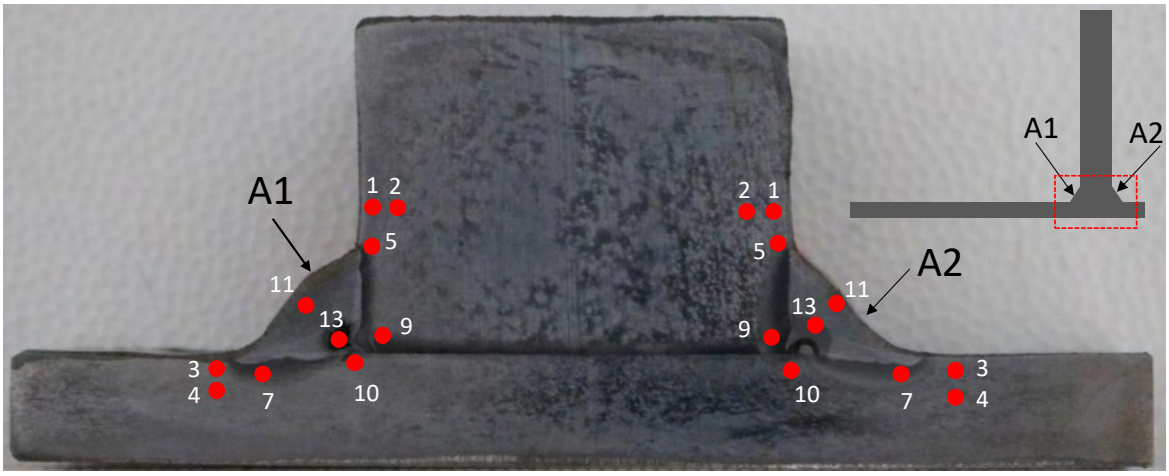

Figure 52. Areas of microhardness testing with individual indentations (1-11).

Table 5. Micro-hardness measurements (HV_2.)

	Specimen 1		Specimen 2	
Position	A1	A2	A1	A2
1	201	201	170	182
2	207	206	165	185
3	288	226	224	215
4	213	214	188	181
5	459	422	356	434
7	289	299	260	284
9	338	452	295	297
10	267	266	257	244
11	305	274	285	295
13	292	302	275	205

4.3 Experimental results

The results from the fatigue experiments are summarized in **Table 4**. The table presents the applied amplitude Δu, the corresponding uplifting rotation θ, the maximum load applied in each test, and the number of cycles corresponding to the following stages: (a) at the first visible crack N_1, (b) at the stage where the applied load drops 20% with respect to the maximum load of the first cycle N_{20}, and (c) at failure N_f, which is defined as the stage of total separation of the "shell" from the "base".

The global response of the specimens is presented first, in terms of load-displacement of the L-joint. In those load-displacement diagrams, the first 20 cycles are plotted with solid line while the dash-dot line refers to the cycle at which 20% reduction of maximum load of the first cycle occurs. The final cycle of the test-corresponds to failure and is also plotted in each figure. Moreover, time laps of crack propagation in some representative specimens are presented as obtained by the camera. **Figure 48** depicts the experimental set-up using the camera, in order to take the photos of the time-laps. Time-laps have also been used in order to identify the first visible crack at the upper side of the specimen. In **Figure 53** to **Figure 54**, the force-displacement diagrams for all the experiments are presented. The experimental results show that the value of N_{20} is more than twice the number of cycles corresponding to first crack detection N_1. This means that the L-joint

welded connections under consideration are capable of sustaining a substantial number of cycles until the structural response deteriorates, well beyond the stage of first crack detection.

All specimens failed due to fatigue cracks initiated and propagated at the vicinity of the weld toe at the "base plate", leading to total separation of the "shell" form the "base". **Figure 55** depicts the force reduction recorded during the tests defined as the maximum force of each cycle normalized by the maximum force of the first cycle. This force reduction is plotted with respect to the normalized fatigue cycles (N/N_f). All specimens failed when the maximum load has reduced by an amount ranging from 45% to 70% of the maximum load recorded in the first cycle. Moreover, the results indicate that, in all experiments, the maximum force decreases by 20% when more than 80% of the total fatigue life is reached. Nevertheless, after that stage the capacity of the connection reduces rapidly in all specimens. In the specimens subjected to smaller displacement ($\Delta u<32.5$mm) the force on the welded connection seems to stabilize at near failure at approximately 60% reduction of maximum force, while in specimens subjected to higher amplitude of displacement ($\Delta u\geq 32.5$mm), the force reduction is more abrupt.

The experimental results show that the presence of weld defects may reduce significantly the structural performance. **Figure 56** shows a picture of specimen B5. In this specimen, the initial geometry of the weld is not smooth and a small imperfection has been detected at the weld toe, which may be the reason for the short fatigue life of this specimen, compared with other specimens subjected to larger displacement (e.g. specimen B1). For the case of specimen A5, subjected to displacement amplitude equal to 37.5 mm, a crack has been detected since the beginning of the test, because of the presence of an initial imperfection at the weld-toe leading to fatigue crack growth at that region.

Figure 57 presents the crack propagation for specimen A5, and in **Figure 58** crack evolution until the through thickness stage is shown. Furthermore, **Figure 59** presents the crack growth for specimen B1. In this specimen, the maximum load drops 20% after 89 cycles, which is more than 2.5 times the number of cycles corresponding to first crack detection ($N_1=33$). Specimen A2 was subjected to displacement amplitude 40 mm, the largest displacement amplitude considered in the present experimental program. In that experiment, crack initiation was observed at the third cycle, whereas total failure (separation) occurred after 36 cycles. The force-displacement diagram shows that after 34 cycles the maximum load had been reduced by 20%, which means that despite the early

crack initiation detected, the specimen has been capable of resisting a significant number of cycles until a significant drop of the load is observed.

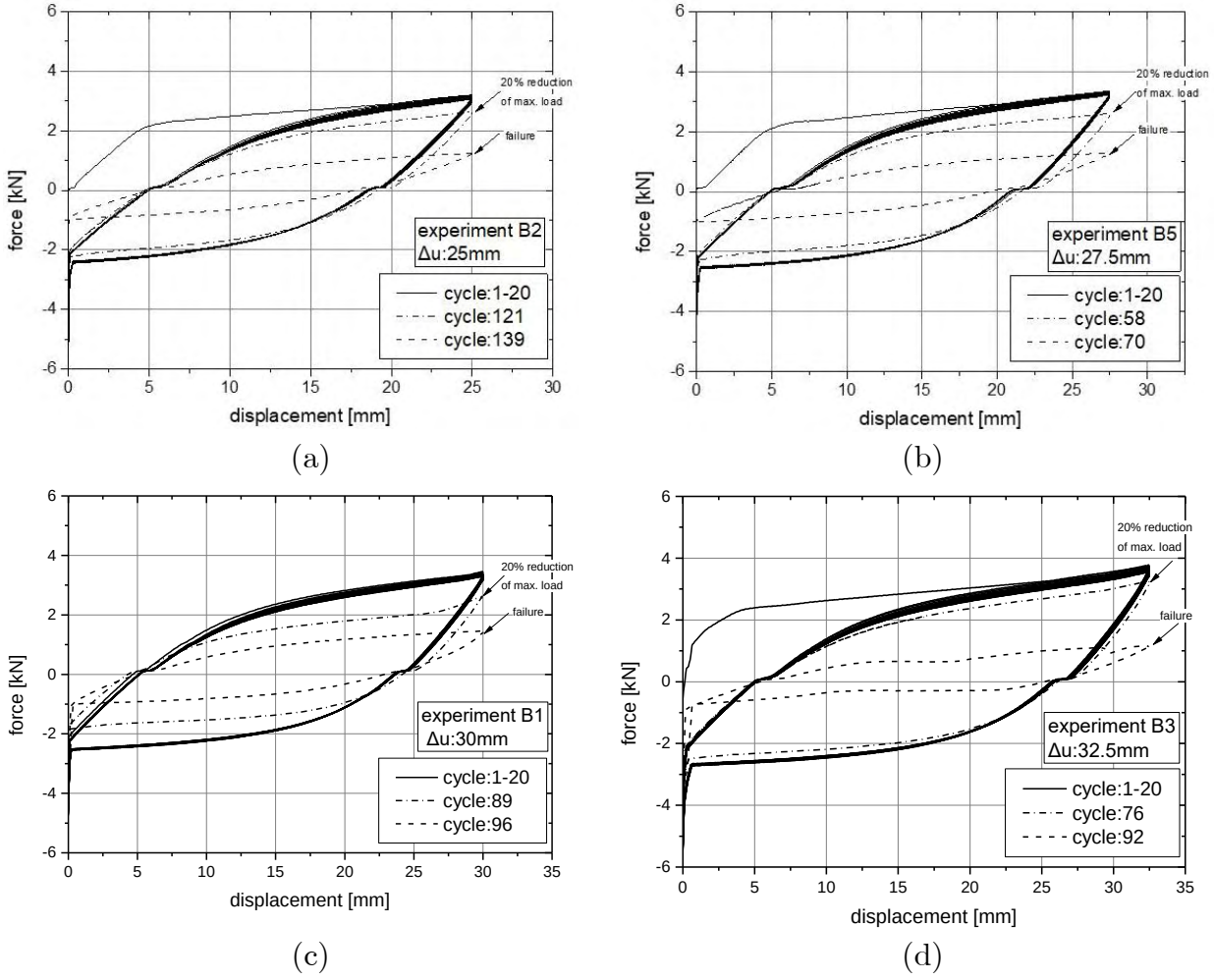

Figure 53. Force–displacement diagram for experiment; (a) B2 (Δu=25mm), (b) B5 (Δu=27.5mm), (c) B1 (Δu=30.0mm), (d) B3 (Δu=32.5mm).

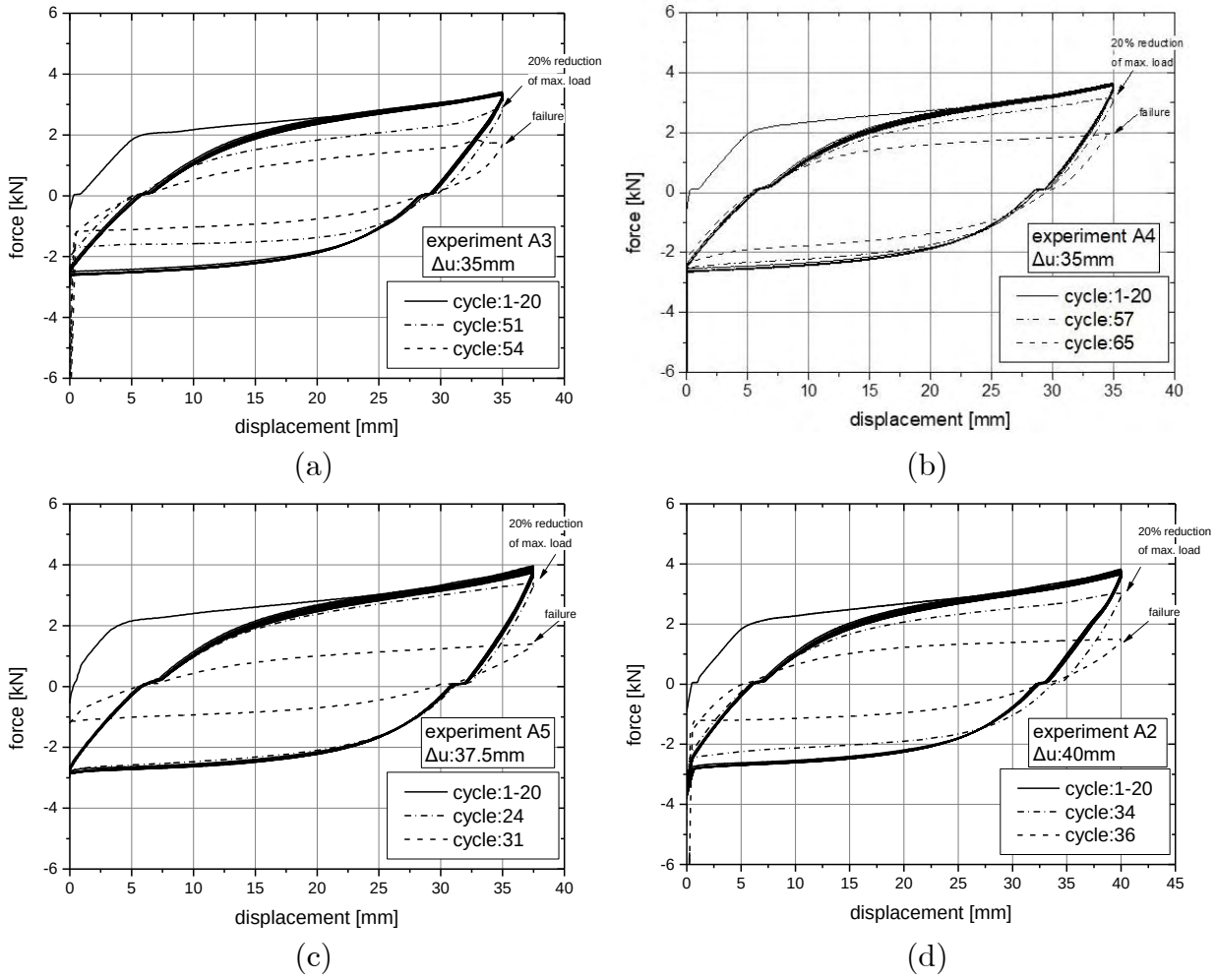

Figure 54. Force–displacement diagram for experiment; (a) A3 (Δu=35mm), (b) A4 (Δu=35mm), (c) A5 (Δu=37.5mm), (d) A2 (Δu=40mm).

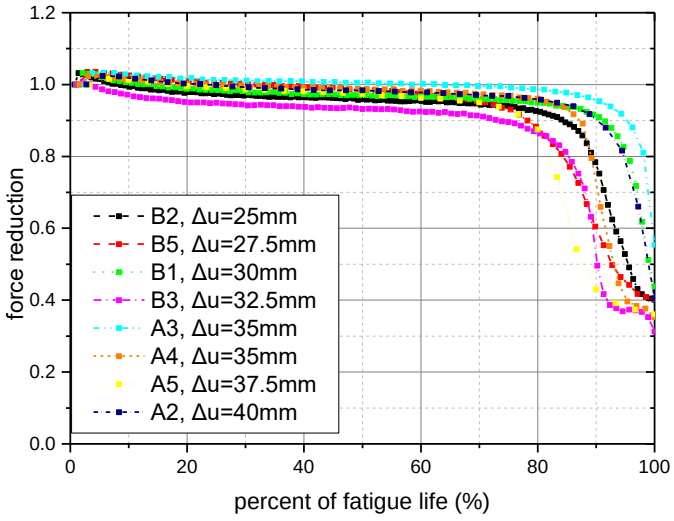

Figure 55. Normalized force–cycle diagram.

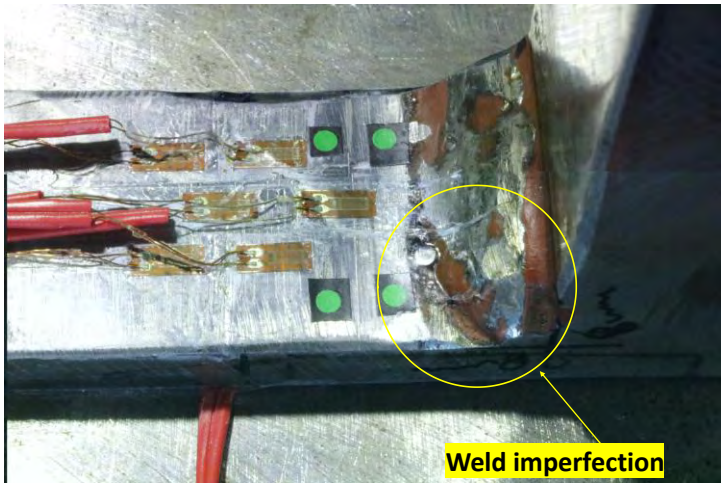

Figure 56. Specimen B5 before the test, showing the weld imperfection.

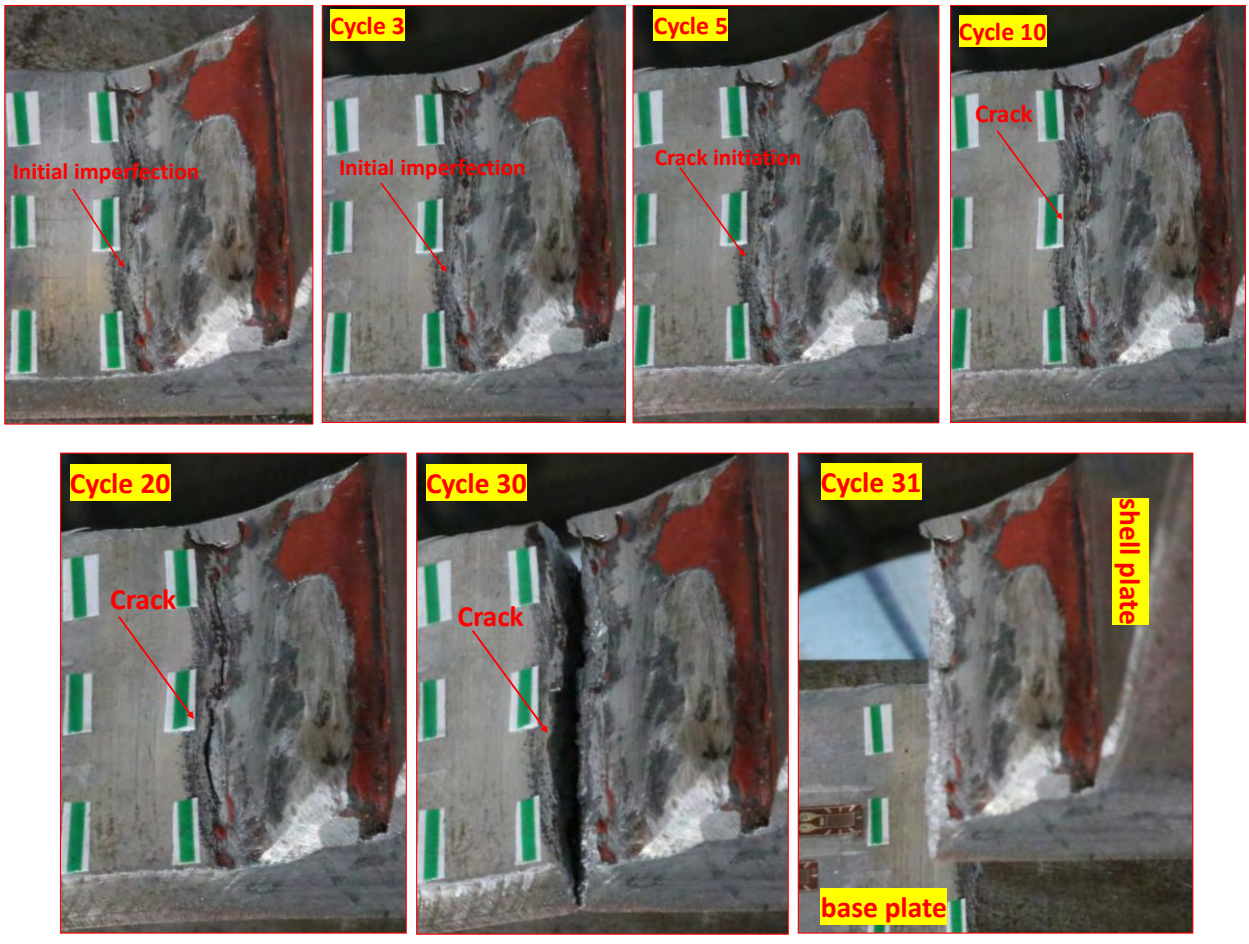

Figure 57. Crack evolution in the surface of specimen A5 (displacement amplitude Δu = 37.5 mm)

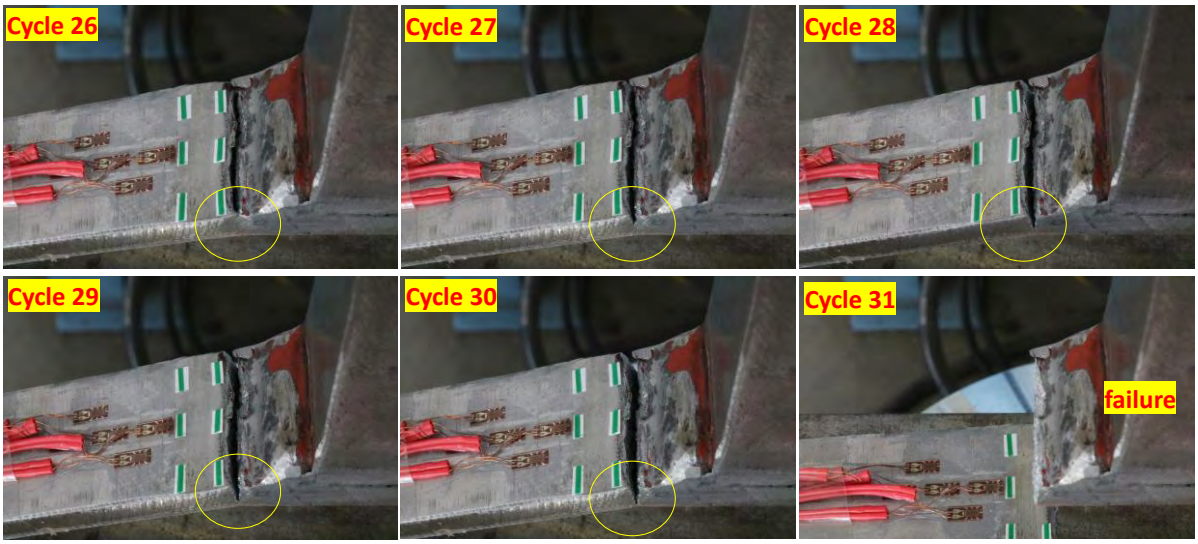

Figure 58. Crack development through the thickness of the "base plate" in specimen A5 (displacement amplitude Δu=37.5 mm).

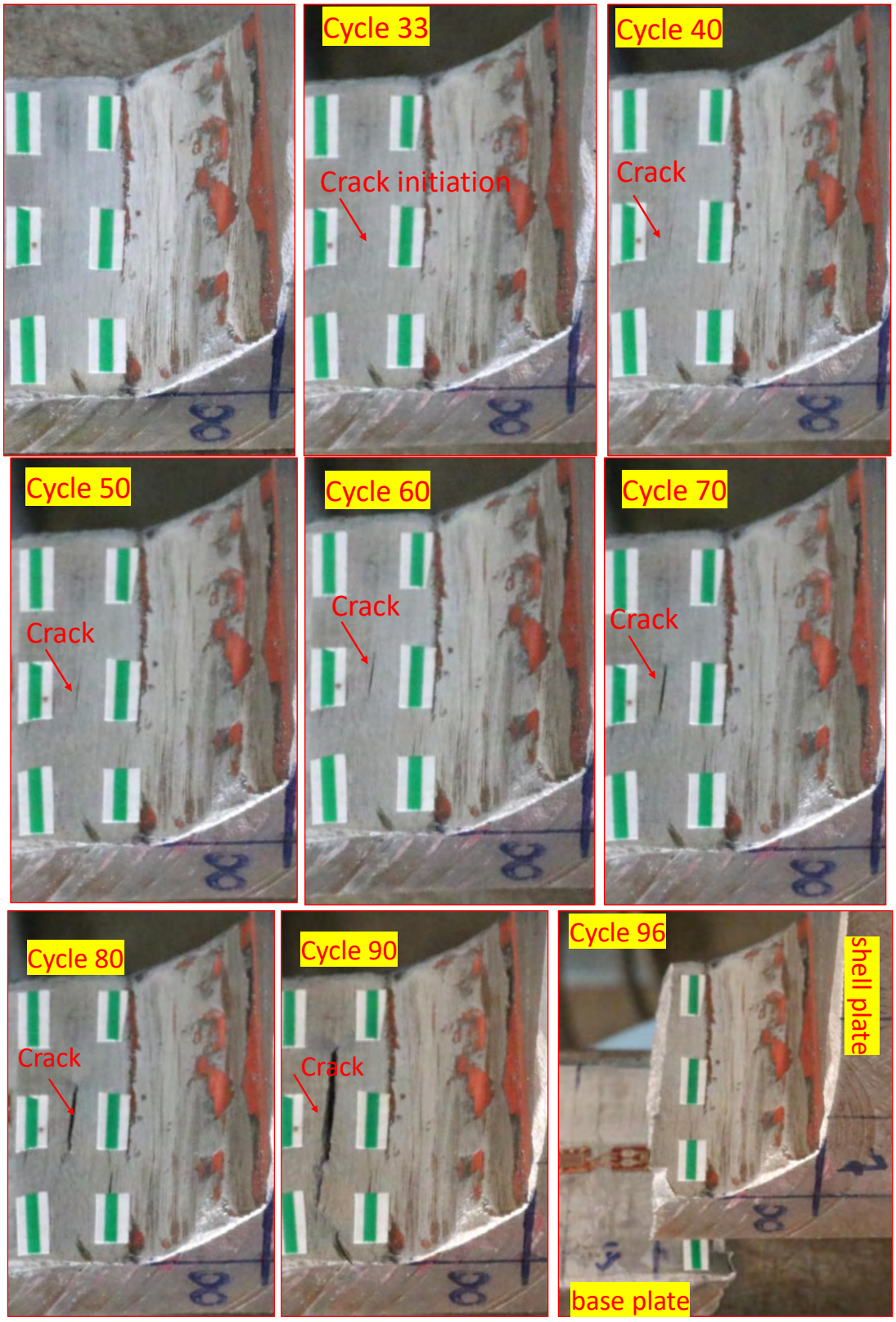

Figure 59. Crack development at the top surface of specimen B1 (displacement amplitude Δu=30 mm).

After the completion of the LCF (low-cycle-fatigue) tests, optical inspection of all failed segments has been performed under stereoscope, followed by a thorough metallographic investigation, which focused in the vicinity of the crack initiation site. It is worth noting that the position of crack initiation, observed in each L-joint tested, using the time lapse captured by the camera (**Figure 48Figure 48**), was used for the extraction of specimens for optical inspection. It was found out that the fatigue cracks were either located entirely in the base metal in three specimens (B1, B2, A3) or within the HAZ in the other specimens (B3, B5, A2, A4, A5). In addition, several secondary fatigue cracks evolved parallel to the main crack. In specimens B2, B5, A2, A5 the secondary cracks were detected only at the bottom plate surface, while in all other specimens secondary cracks were located on both surfaces as illustrated for specimen B1 in **Figure 60**. The through-thickness crack path is depicted in **Figure 61**a exactly at the initiation site for specimen B1 and clearly indicates that the main fatigue crack initiates and propagates entirely within the base metal, while several secondary fatigue cracks were revealed both at the upper and the bottom surface of the base metal (**Figure 61** b and **Figure 61** c). All secondary cracks propagate parallel to the main crack and are confined within a "zone" 2.68-mm-wide at the upper surface and 4.11-mm-wide at the bottom surface. In **Figure 62** the through-thickness crack path at the initiation site for specimen B3 is presented. In this case, the main fatigue crack begins at the weld toe within the HAZ and propagates through the base metal until the final fracture occurs.

The corresponding results for specimen A2 are provided in **Figure 63**. The main crack initiates at location between the coarse and the fine grain HAZ, while secondary micro cracks were observed at both surfaces within the base metal, and propagated parallel to the fracture surface. Indicative Microhardness imprints and the relevant Microhardness values are depicted in **Figure 63**c. The microstructure adjacent to the fracture surface is depicted in **Figure 64**. The crack path follows the ferrite and perlite bands of the base metal, producing a scalloped fracture surface with local plastic deformation areas.

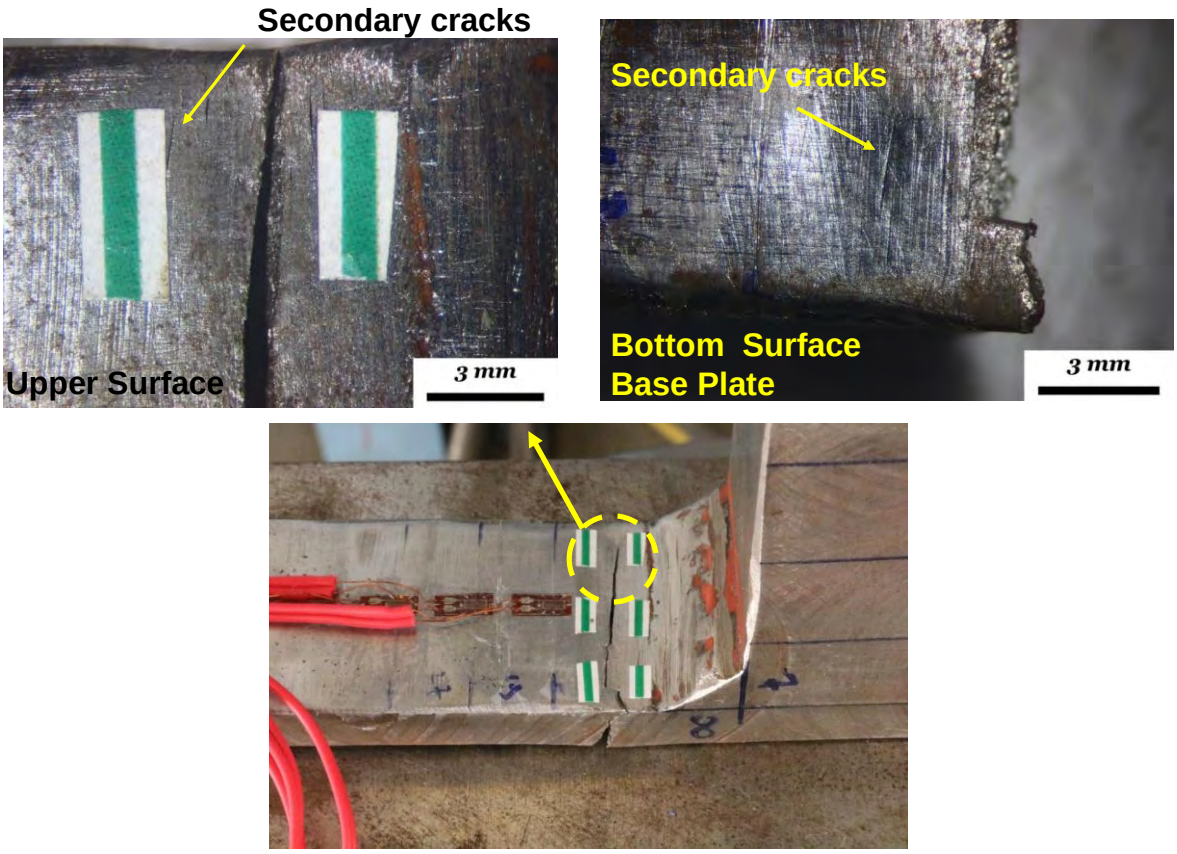

Figure 60. Secondary fatigue cracks in specimen B1 (displacement amplitude Δu=30 mm), both in the upper and bottom surface of the base plate.

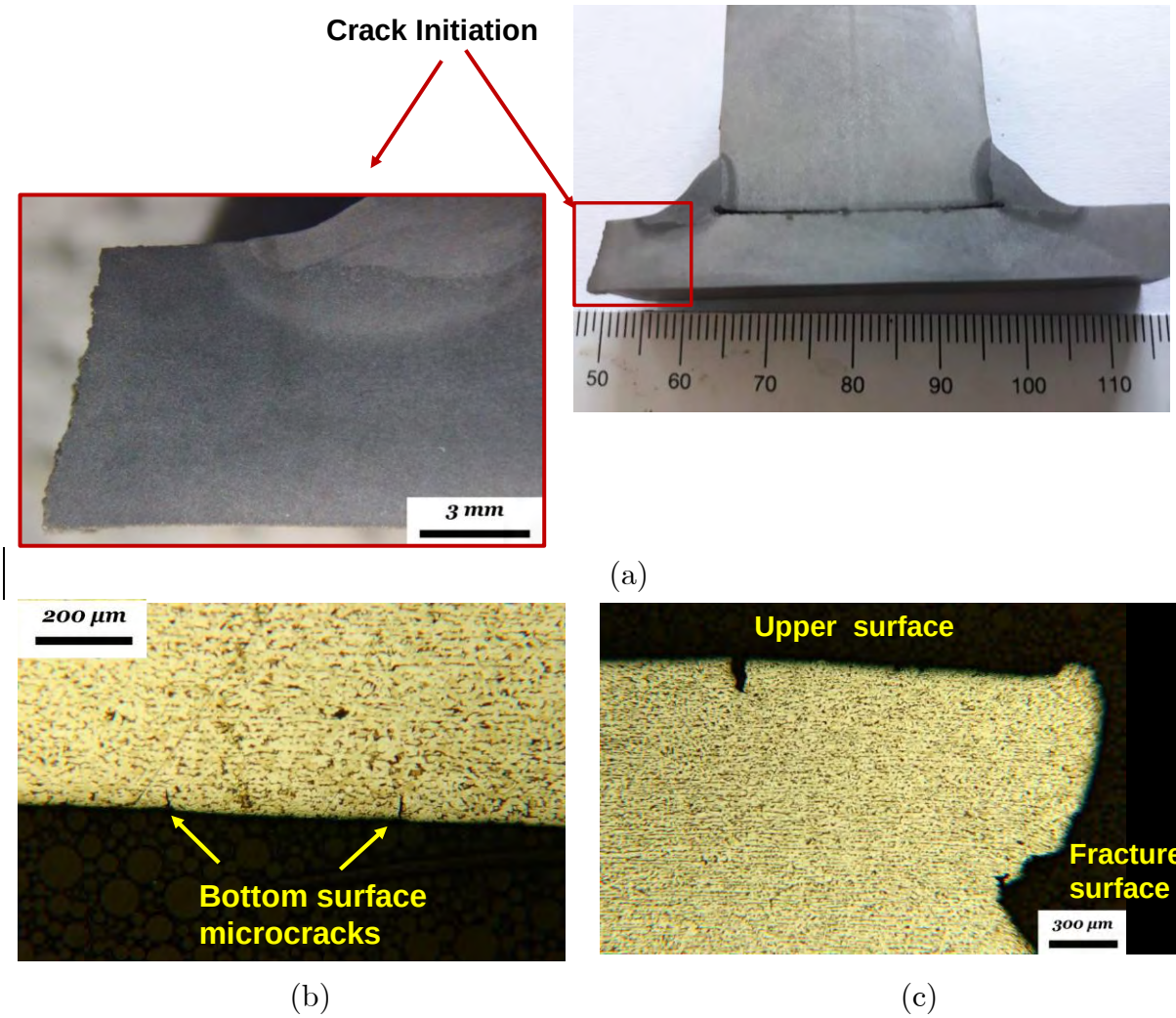

Figure 61. (a) Macrostructure of specimen B1 (transverse cross section at the crack initiation site shown in **Figure 60**, at loading cycle 33); (b) & (c) microstructure at the upper and bottom surface associated with secondary fatigue cracks.

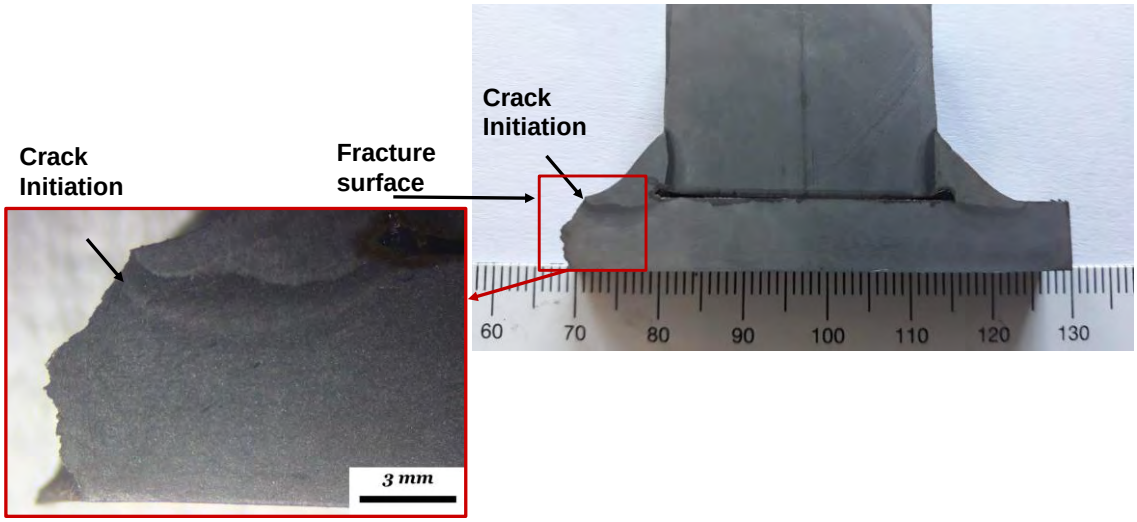

Figure 62. Macrostructure of specimen B3 (displacement amplitude Δu=32.5 mm): transverse cross section at the crack initiation site; detailed of macrostructure at the crack initiation region.

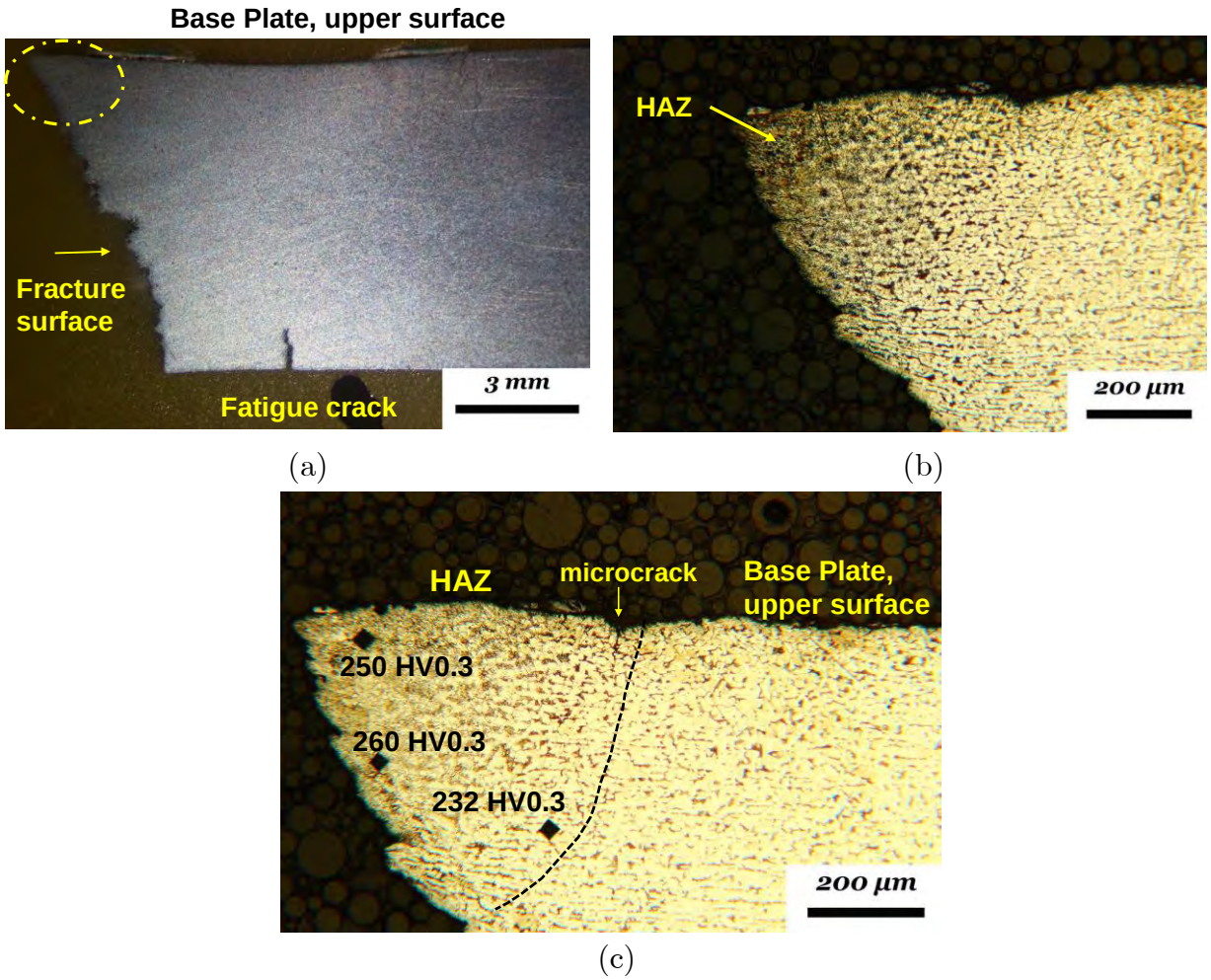

Figure 63.(a) Macrostructure of specimen A2 (displacement amplitude Δu=40 mm) at the initiation site; (b) microstructure at the fatigue initiation site; (c) closer view of 26(b).

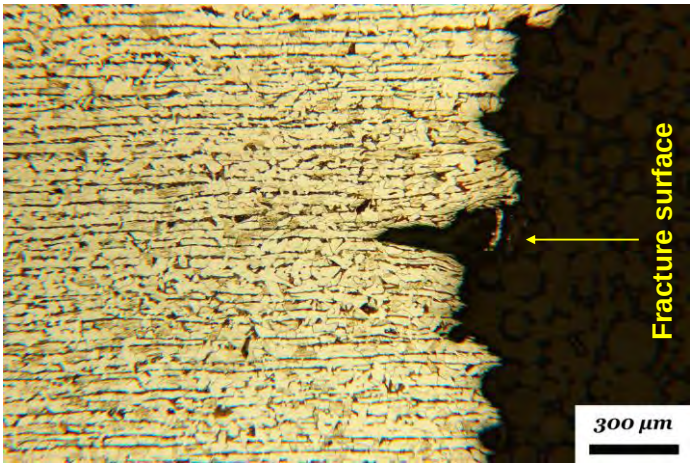

Figure 64. Microstructure adjacent to the fracture surface (specimen B1).

4.4 Finite element modeling

The experiments presented in section 4.3 are supported by numerical simulations, which complement the test measurements. More specifically, the laboratory data acquisition system is capable of recording strains up to 6%, which may not be adequate for recording the strains induced near the weld toe during the test. Therefore, the strain values are computed numerically, so that they are used for performing a fatigue assessment analysis. A three-dimensional model is developed in general-purpose finite element program ABAQUS/Standard, which uses eight-node linear "brick" elements with reduced integration, denoted as C3D8R in ABAQUS. **Figure 66** depicts the finite element and its parts. A preliminary mesh-sensitivity analysis has been performed for the number of elements to be used across the plate thickness. Based on the results of this preliminary analysis, 16 elements have been employed across the base plate thickness. In **Figure 67**, a detail of the meshed numerical model is depicted showing that the gap between the shell and the base plate due to the fillet weld connection is taken into account. Only the geometry of weld is taken into account. The residual stresses created during welding process have been neglected, since part of them have been relieved during the extraction of the examined specimens from the larger specimen shown in **Figure 45**. Furthermore, in low cyclic fatigue conditions, the influence of the residual stresses on fatigue behavior is not dominant. The boundary conditions used in the simulation are those imposed in the experiments, as described in section 4.2. The bounding surface constitutive model described in Chapter 2 has been used, which takes into account both the plastic plateau and the Bauschinger effect.

A major feature in carbon steels, which also appears in the steel material of the present connection, is the abrupt change of slope in the stress–strain curve after initial yielding, associated with very low hardening up to about 2% strain, referred to as "plastic plateau". With continuing deformation, hardening appears as shown in **Figure 65**. To model this feature, the initial size and position of the YS is assumed identical to the size and position of the BS. In addition, a low hardening modulus with constant value for the initial yielding of the BS is assumed for simulating the plastic plateau, whereas an exponential function is employed for representing the hardening region after the plastic plateau, relating the YS size with the equivalent plastic strain of the current plastic loading. During reverse plastic loading, the two surfaces have already established a distance δ, because the yield surface shrinks, while the bounding surface expands, so that the hardening function of eq. (8) is activated, and the Bauschinger effect is modelled.

To calibrate the material model, stress-strain curves have been used from tests on S275J2 steel strip specimens presented in section 4.2. In **Figure 65**a, the tensile stress-strain experimental curve and the corresponding numerical fitting is presented. Furthermore, **Figure 65**b depicts the stress-strain curve and the corresponding numerical fitting for the cyclic strain-controlled tests. It is important to underline that the same parameters obtained from the above calibration process have been used for simulating the fatigue loading experiments.

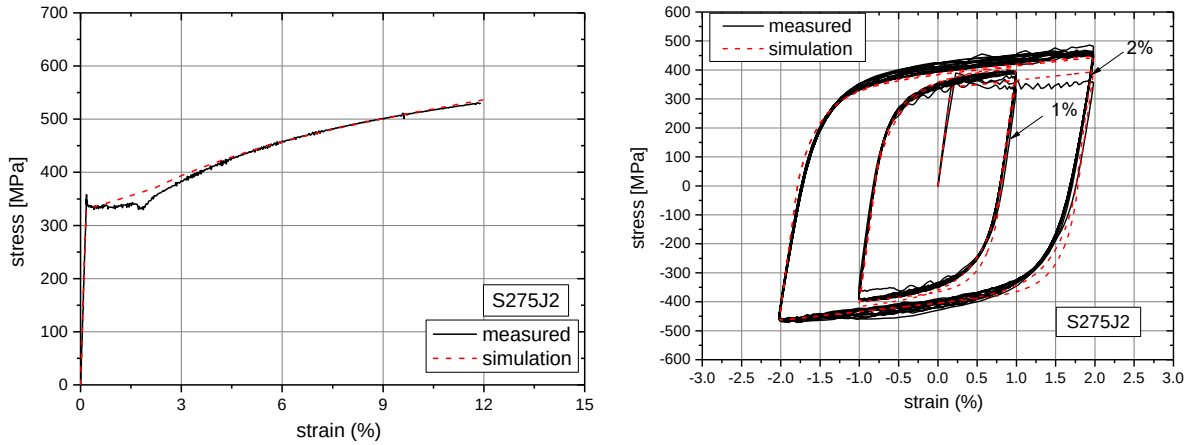

(a) (b)

Figure 65. Calibration of material model for the S275J2 steel of the base plate: (a) tensile material test; (b) cyclic strain-controlled material test.

Table 6. Summary of material parameter values for S275 J2 steel material.

Isotropic hardening parameters [yield surface]	σ_y (MPa)	350
	Q (MPa)	-110
	b	300
Isotropic hardening parameters [bounding surface]	σ_b (MPa)	350
	Q_b (MPa)	80
	b_b	50
Hardening function parameters	$\bar{H}$ (MPa)	1,200
	a (MPa)	55,000
	d	2
	n	0.1
	m	4

The validation of the numerical model is performed by comparing the numerical results with strain measurements obtained from the experiments at specific locations located at the base plate as shown in **Figure 47**. **Figure 68** depicts the deformed shape of the specimen. In **Figure 69** to **Figure 71** the force-strain diagrams for three different experiment (Δu: 25mm, 27.5mm, 30mm) are presented. For each experiment, the model is validated using the recording of two or more strain gauges. In those figures, the exact location of the measurements is also shown. The results show that the model is capable of predicting the structural response of the L-joints, in terms of both the load-displacement behavior and the local strains at the critical region.

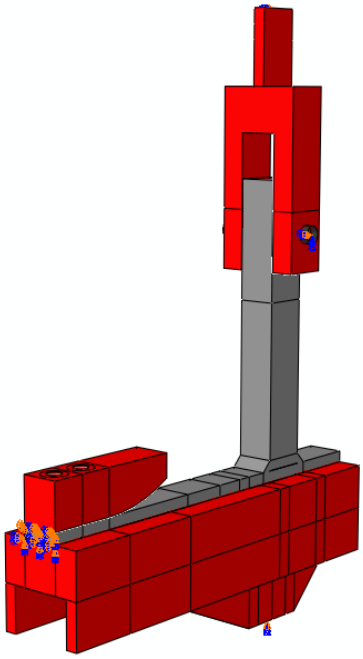

Figure 66. Numerical model of the fillet-welded connection, simulating the procedure followed in the experiments.

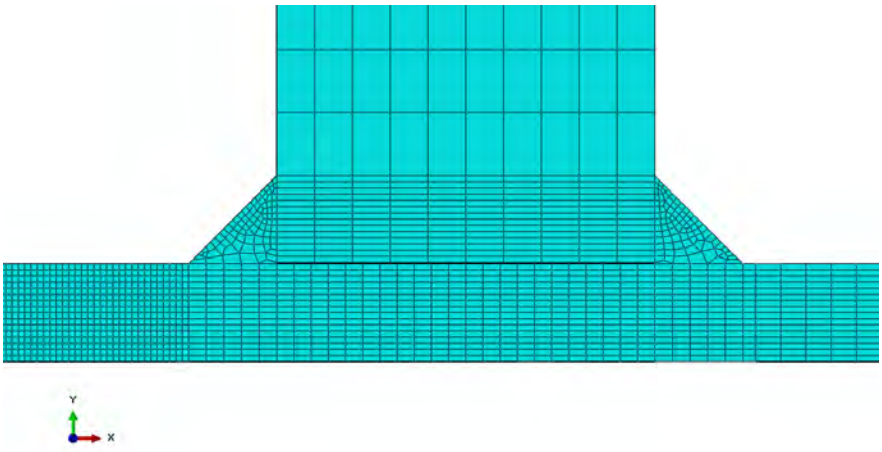

Figure 67. Detail of the meshed numerical model at the weld area; the model accounts for the exact geometry of the fillet welded connection; the bottom edge of the "shell" plate is not connected to the bottom plate.

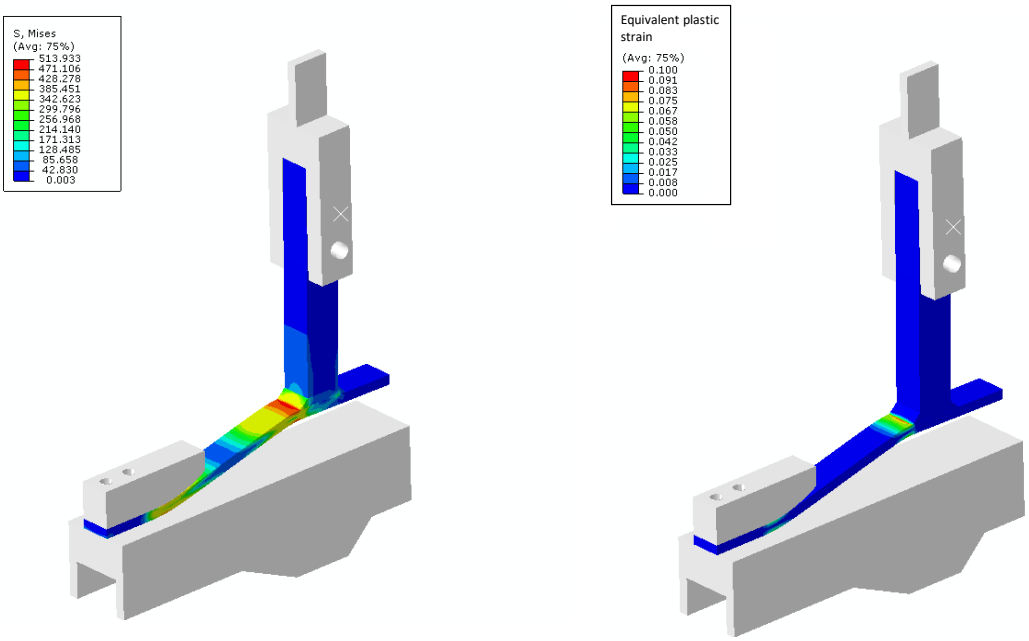

(a) (b)

Figure 68. Deformed shape of fillet-welded specimen obtained from the finite element model, showing the distribution of (a) von Mises stress and (b) equivalent plastic strain.

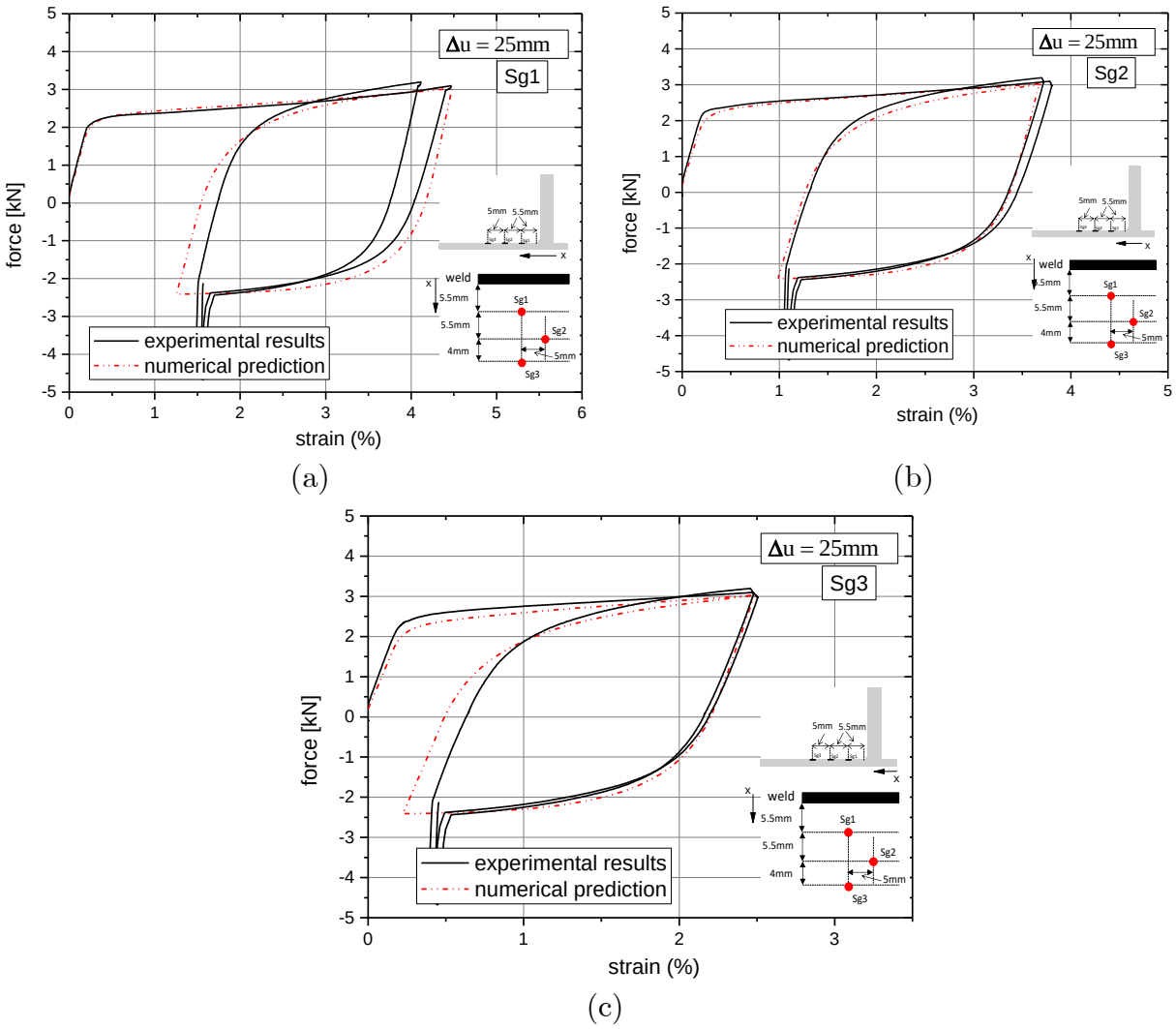

Figure 69. Force-strain diagram for Δu equal to 25mm at strain gauge; (a) Sg1, (b) Sg2, (c) Sg3.

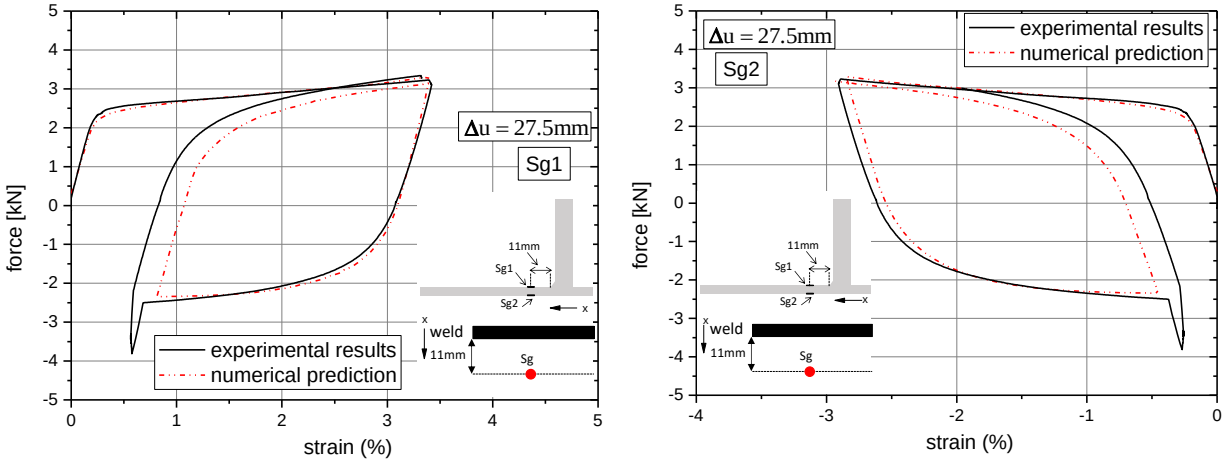

(a) (b)

Figure 70. Force-strain diagram for Δu equal to 27.5mm; (a) Sg1, (b) at strain gauge Sg2; negative value of strain refer to compression because of the strain gauge location.

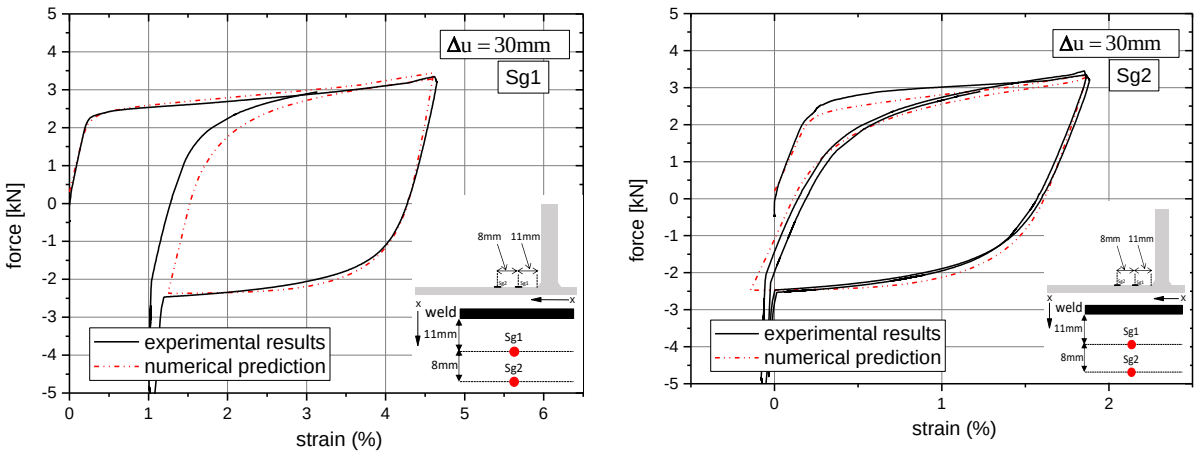

(a) (b)

Figure 71. Force-strain diagram for Δu equal to 30mm; at strain gauge (a) Sg1, (b) Sg2.

4.5 Fatigue analysis

Using the validated finite model presented in section 4.4, the strain range $\Delta\varepsilon$ and the maximum strain ε_{max} at the toe of weld are calculated in all specimens, using the following procedure: the strain range Δε and the maximum strain ε_{max} are calculated numerically at different locations along the path perpendicular to the weld toe shown in **Figure 72** and, subsequently, the calculated Δε or ε_{max} strain values are linearly extrapolated to the weld toe, to obtain the so-called "hot-spot" values.

Figure 73 to **Figure 75** present the strain range $\Delta\varepsilon$ and the maximum strain ε_{max} values obtained from the numerical analysis and the above extrapolation procedure, with respect to the number of cycles to failure (N_f) recorded in the corresponding experimental tests. The results in **Figure 73** show that the difference of maximum strain value with the corresponding strain range value decreases as the displacement amplitude increases. In **Figure 74** and **Figure 75** the results from specimens (A5, B5) with initial imperfections (defects) are denoted with red dots. Moreover, in those figures an analytical expression for the strain range $\Delta\varepsilon$ and the maximum strain ε_{max} with respect to the number of cycles to failure N_f is developed using a standard curve-fitting procedure. In **Figure 75** the extrapolated values of $\Delta\varepsilon$ and ε_{max} strain in each specimen are plotted with respect to the number of cycles at which the maximum load decreases by 20% with respect to the one in the first cycle (N_{20}). The results show that despite the very high levels of strains developed at the vicinity of the fillet-weld connection (10%), the connection is capable of sustaining a significant number of cycles before failure. It is also important to mention that the strain-based to fatigue life curves can be used directly in a fatigue assessment of the connection in the course of a seismic analysis of uplifting tanks, as described in detail by Vathi and Karamanos [113].

A deformation parameter used in several studies and adopted in relevant standards [108] [109] is the rotation of the connection during uplift. The global rotation of the connection "θ" is used in the present study, defined in **Figure 48**. This rotation is similar to the one reported in previous experiment [107],[110]-[112]. Moreover, a plastic rotation ("θ_p") is also employed, defined as the inelastic part of the relative rotation of two cross-sections at distance "L_p" equal to twice the plate thickness, shown in **Figure 76**. The values of rotation θ and θ_p for each case are reported in **Table 4**, and **Figure 77** depicts the two angles with respect to the number of cycles. The results show that, during the uplifting tests, the level of plastic rotation θ_p can be higher than the limit of 0.2 rad stated in design documents [108],[109], but the connection is capable of sustaining a significant number of cycles before failure. Nevertheless, it is the author' opinion the value of rotation depends on the specific case (real case or laboratory) under consideration and may not offer ra reliable measure for assessing the fatigue strength of the connection.

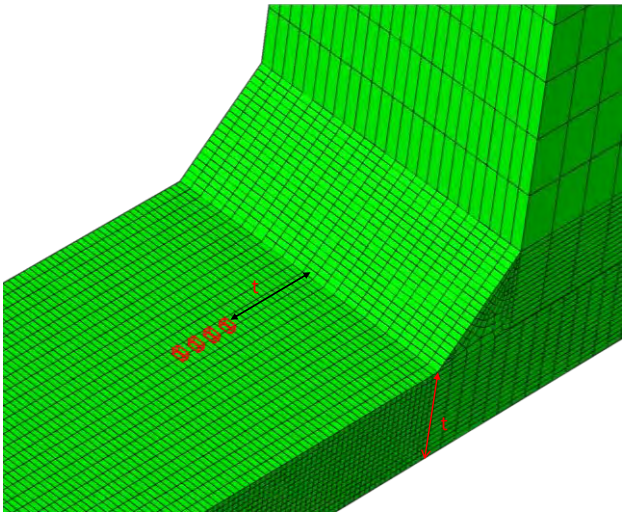

Figure 72 Element path used for strain extrapolation to the weld toe.

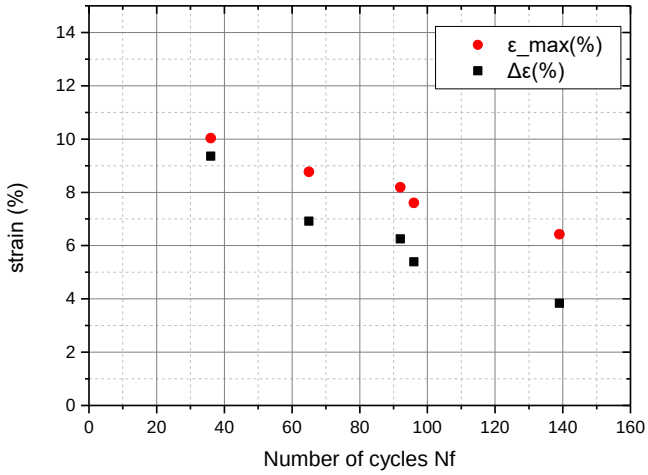

Figure 73. Strain-range ($\Delta\varepsilon$) and maximum strain (ε_{max}) with respect to the number of cycles to failure N_f.

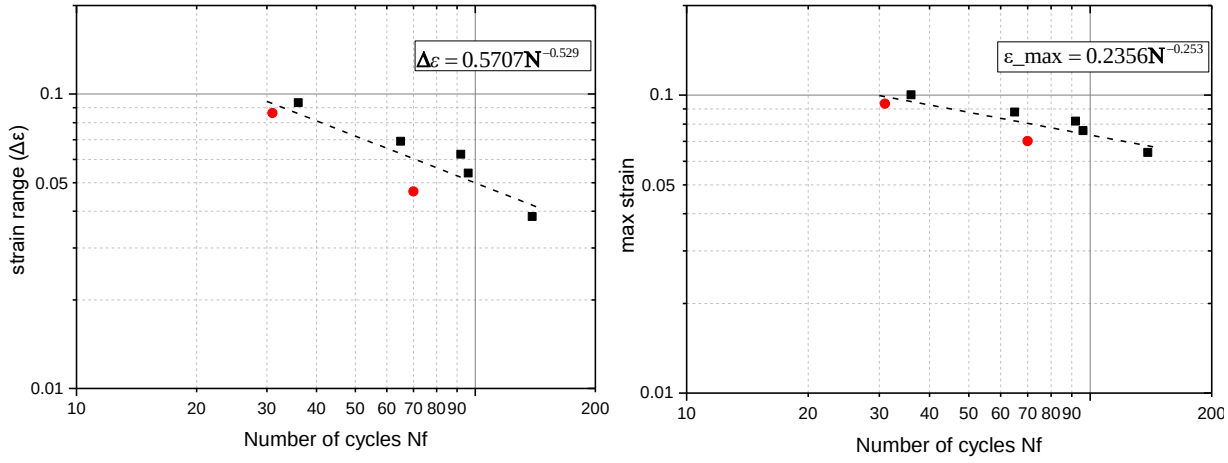

(a) (b)

Figure 74. (a) Strain range ($\Delta\varepsilon$) and (b) Maximum strain (ε_{max}) with respect to the number of cycles to failure N_f.

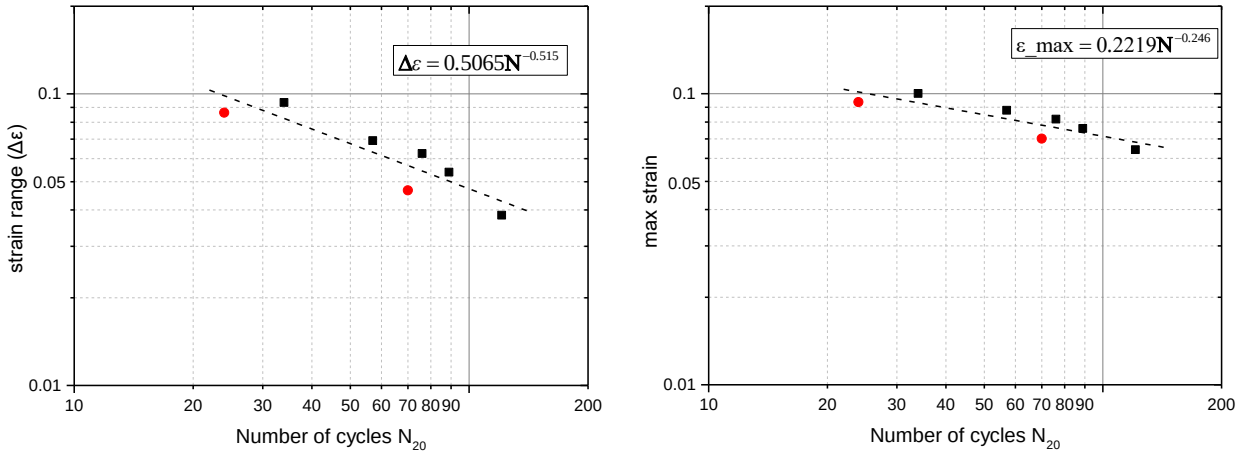

Figure 75. (a) Strain range ($\Delta\varepsilon$) and (b) maximum strain (ε_{max}) with respect to the number of cycles N_{20}, corresponding to 20% reduction of connection strength.

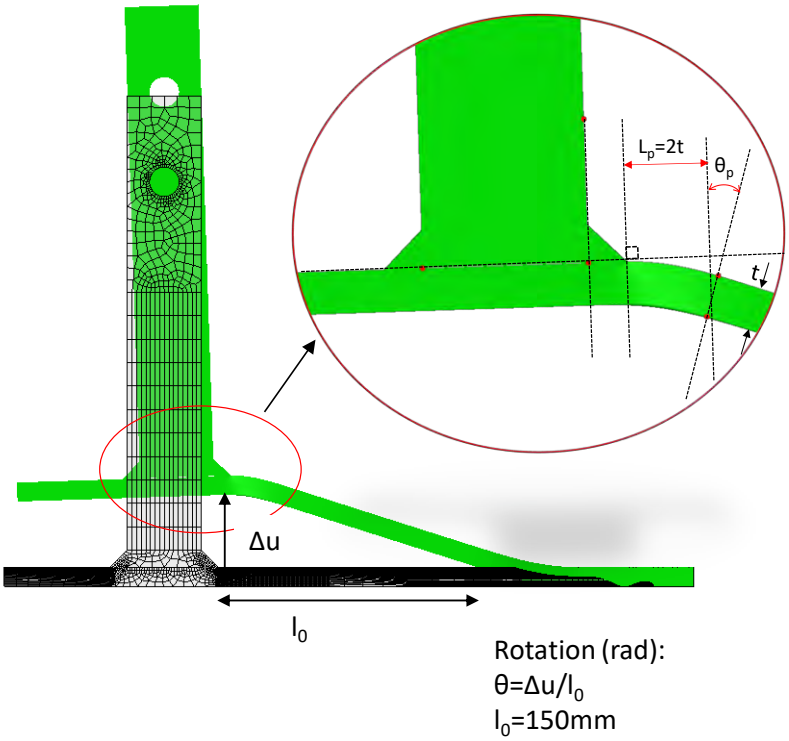

Figure 76. Definition of total rotation θ and plastic rotation θ_p.

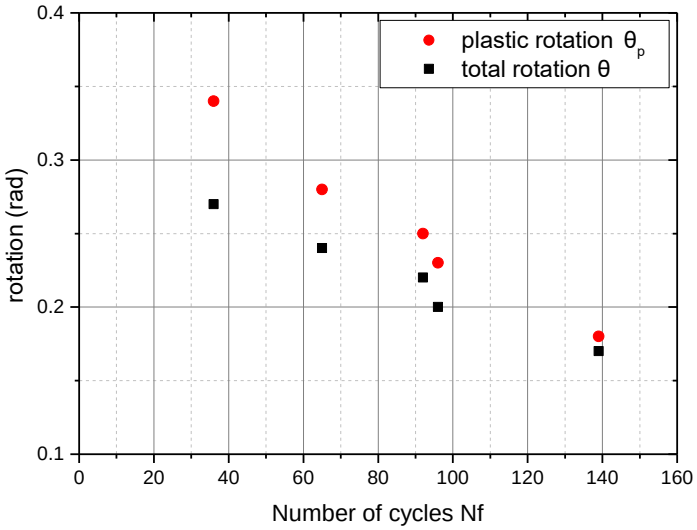

Figure 77. Rotation and plastic rotation of the connection with respect to the number of cycles to failure N_f; only non-defected specimens are shown in this graph.

4.6 Conclusions

The present chapter describes an experimental program on the low-cycle fatigue resistance of fillet-welded plate connections, supported by numerical simulations. The study is motivated by the seismic response of unanchored steel tanks, subjected to strong cyclic loading, which could lead to failure of the welded base-plate-to-shell connection in the form of low-cycle fatigue due to repeated uplift. Fillet-welded specimens, representing this connection, have been tested under repeated constant-amplitude loading using a special-purpose experimental set-up, in order to determine the relationship between the strain developed at the weld toe and the corresponding number of cycles to failure. Material tests on strip specimens have been performed in order to characterize the material of the base plate. Micro-hardness measurements have been conducted at the weld connection and stereo-optical microscopy has also been employed to identify the presence of defects at the connected region. Inspection of the failed specimens has also been performed, indicating that the fatigue cracks are located entirely in the base metal or in the HAZ (heat affected zone). Moreover, several microcracks have been observed at the critical location during the inspection, the average value of width of the "zone" where microcracks are visible is 2.68 mm wide at the upper surface and 4.11mm wide at the bottom surface.

The welded joint response has also been simulated numerically using rigorous finite elements that employ the cyclic-plasticity material model, presented in Chapter 2. The

numerical simulation of the experimental procedure reported in this study, complements the experimental data and predicts the strains induced near the weld toe during the test, given the fact that the data acquisition system is not capable of recording strains higher than 6%. The material model is calibrated using material tensile tests and cyclic strain-controlled tests from strip specimens extracted from the plates under consideration. Using the calibrated parameters, the experimental results have been predicted quite accurately in terms of both global response and local strains. Based on the experimental and numerical results, fatigue curves have been developed, providing the number of cycles to failure for a given maximum strain or a strain range. The results show that, despite the high level of strain developed at the vicinity of the weld (calculated up to 10% in the few cases), the fillet-welded joints under consideration are capable of sustaining a significant number of cycles before failure. Furthermore, comparing the level of deformation induced in the specimens with the corresponding limits specified by relevant design provisions, it is concluded that these design provisions are quite conservative.

Finally, it is important to underline the contribution of the constitutive model employed in the simulations for predicting the mechanical behavior of the joint. The model, upon its calibration through appropriate material tests (monotonic and cyclic), has been capable of describing quite accurately inelastic material response under repeated plastic deformation of alternate sign, and offers an efficient and reliable tool for analyzing steel structural components under severe cyclic loading.

Chapter 5 – Summary and Conclusions

The present dissertation aims at the development of an efficient numerical implementation of a bounding-surface (two-surface) model for cyclic plasticity, suitable for simulating the mechanical response of metal structural members and components, subjected to strong cyclic loading. The model is implemented in a finite element environment and its integration follows an elastic-predictor/plastic-corrector scheme. All steps of the numerical integration algorithm are presented in detail allowing for its implementation in a material-user subroutine for a finite element software. Some special features of the model are addressed and discussed to elucidate its capabilities in simulating accurately steel material response. An important issue refers to the relative position of the two surfaces during the integration process, and their possible contact within strain the increment under consideration. This constitutes an essential issue for defining the hardening modulus and it is taken into account in a rigorous manner. Furthermore, the sensitivity of cyclic response on some key material parameters is presented. In particular, a modification on the hardening modulus is proposed, which improves the model capabilities in predicting strain accumulation under non-symmetric stress-controlled conditions. Simulations of small-scale tests from mild steel and high-strength steel have also been performed, which demonstrate the efficiency of the model and its capability to describe both stress-controlled and strain-controlled tests using the same set of material parameters.

In the second part of the study, the numerical simulation of steel piping elbow performance, subjected to strong cyclic loading conditions, has been presented. The elbows have been modeled rigorously using nonlinear finite elements and the cyclic-plasticity material model based on the bounding-surface concept, presented in the first part of the dissertation. The work is supported by experimental data on elbow specimens subjected to in-plane cyclic bending, under several levels of internal pressure. The constitutive model has been calibrated using small-scale strain-controlled and stress-controlled material tests from strip specimens extracted from elbows fabricated from the same heat. Using the calibrated material parameters of the model, the experimental results of large-scale laboratory tests have been simulated accurately and very good predictions on the value of local strain and its accumulation over the loading cycles at the critical elbow location are obtained. This very good comparison between experimental and numerical results

demonstrates the capability of the constitutive model under consideration in predicting the inelastic response of steel piping components under strong cyclic loading and the rate of strain ratcheting, as well as its suitability for large-scale computations. An extensive analysis is performed in order to elucidate the effect of internal pressure on elbow response with emphasis on local strain accumulation at different elbow locations. It was concluded that, for all cases examined, the flank location is critical in terms of maximum strain value and its evolution rate. Furthermore, the hoop strain range at the flank, and the corresponding ratcheting rate are higher than the corresponding axial strain range and ratcheting rate, which is consistent with the location and orientation of failure pattern observed experimentally. The results also indicate that the amplitude of axial strain at the flank and the intrados is similar, while the strain level at the elbow extrados is significantly lower. Moreover, the results show that, as the level of internal pressure increases the ratcheting rate increases, and the strain amplitude decreases. Finally, considering three different pipe schedules, the effect of elbow thickness on the ratcheting rate and on strain amplitude has been investigated. The results indicate that, for the case of zero internal pressure, the effect of thickness on the ratcheting rate is negligible, while for the case of internally-pressurized elbows this effect is more pronounced.

In the third part of the study, an experimental program on the low-cycle fatigue resistance of fillet-welded plate connections is presented, supported by numerical simulations. The study is motivated by the seismic response of unanchored steel tanks, subjected to strong cyclic loading, which could lead to failure of the welded base-plate-to-shell connection in the form of low-cycle fatigue due to repeated uplift. Fillet-welded specimens, representing this connection, have been tested under repeated constant-amplitude loading using a special-purpose experimental set-up, in order to determine the relationship between the strain developed at the weld toe and the corresponding number of cycles to failure. Material tests on strip specimens have been performed in order to characterize the material of the base plate. Micro-hardness measurements have been conducted at the weld connection and stereo-optical microscopy has also been employed to identify the presence of defects at the connected region. Inspection of the failed specimens has also been performed, indicating that the fatigue cracks are located entirely in the base metal or in the HAZ (heat affected zone). Several microcracks have been observed at the critical location during the inspection, the average value of width of the

"zone" where microcracks are visible is 2.68 mm wide at the upper surface and 4.11mm wide at the bottom surface.

The welded joint response has also been simulated numerically using rigorous finite elements that employ the cyclic-plasticity material model, presented in the first part of the dissertation. The numerical simulation of the experimental procedure reported in this study, complements the experimental data and predicts the strains induced near the weld toe during the test, given the fact that the data acquisition system is not capable of recording strains higher than 6%. The material model is calibrated using material tensile tests and cyclic strain-controlled tests from strip specimens extracted from the plates under consideration. Using the calibrated parameters, the experimental results have been predicted quite accurately in terms of both global response and local strains. Based on the experimental and numerical results, fatigue curves have been developed, providing the number of cycles to failure for a given maximum strain or a strain range. The results show that, despite the high level of strain developed at the vicinity of the weld (calculated up to 10% in the few cases), the fillet-welded joints under consideration are capable of sustaining a significant number of cycles before failure. Furthermore, comparing the level of deformation induced in the specimens with the corresponding limits specified by relevant design provisions, it is concluded that the design provisions are quite conservative.

The contributions of the present dissertation can be summarized as follows:

- ✓ The main contribution of the dissertation refers to the efficient numerical implementation of the "two-surface plasticity model" in a user material subroutine (UMAT), accounting for all the features (plastic plateau, Bauschinger effect, ratcheting etc.) appeared when the material is well within its inelastic regime, and it offers an efficient simulation tool for predicting the inelastic-cyclic response of metal components.
- ✓ An enhanced function for the hardening modulus is proposed for improving the ratcheting predictions of the model, and the special features that characterize the cyclic behavior of carbon steel material (i.e. plastic plateau, Bauschinger effect) are rigorously implemented in the numerical model.
- ✓ Experimental results from large-scale tests are accurately predicted using material parameters, calibrated by small-scale material tests extracted from the large-scale specimens.

- ✓ The cyclic response of steel pipe elbows has been studied using the numerical model under consideration, and the effect of internal pressure and wall thickness on local strain range and accumulation at various locations have been discussed in detail. The response has been found to be in very good agreement with experimental results performed elsewhere.
- ✓ Using the present numerical model, the low-cycle fatigue of L-joint has been examined both experimentally and numerically, motivated by the response unanchored tank subjected to seismic excitation.
- ✓ Strain-based curves for the low-cycle fatigue strength of fillet-welded plated joints have been developed, which can be used for the design purposes. In particular, they can be used for the seismic design of the base-to-shell welded connection in unanchored liquid storage tanks.

Finally, it is important to underline the contribution of the advanced constitutive model employed in the simulations for predicting the mechanical behavior of the both steel pipe elbows and L-joint connections, and offers an efficient and reliable tool for analyzing steel structural components under severe cyclic loading. As a result, the model can constitute the basis for a coupled plasticity-damage model, in order to predict the number of cycles to failure, which constitutes an issue for further consideration in a future investigation.

References

[1] Mahin, S.A., Popov, E.P. and Zayas, V.A., 1980, "Seismic Behavior of Tubular Steel Offshore Platforms" *Offshore Technology Conference,* OTC-3821-MS, Houston, Texas.

[2] Ravikiran, A., Dubey, P.N, Agrawal, M.K., Reddy, G.R., Singh, R.K., Vaze, K.K., 2015. "Experimental and Numerical Studies of Ratcheting in a Pressurized Piping System Under Seismic Load", *Journal of Pressure Vessel Technology*, ASME, Vol. 137, pp. 031011-1-7.

[3] Martinez, M., Brown,G., 2005. "Evolution of Pipe Properties During Reel-Lay Process: Experimental Characterization and Finite Element Modeling*", In: Proc. of the24th International Conference on Offshore Mechanics and Arctic Engineering*, Halkidiki, Greece.

[4] Manouchehri, S., Howard, B., Denniel, S., 2008. "A Discussion of the Effect of the Reeled Installation Process on Pipeline Limit States", In: Proc. of the 18th International Offshore and Polar Engineering Conference, Vancouver, Canada.

[5] Hassan, T., Kyriakides, S., 1992a. "Ratcheting in Cyclic Plasticity, Part I Uniaxial Behavior", *International Journal of Plasticity*, Vol. 8, pp. 91-116.

[6] Bari, S., Hassan, T., 2000. "Anatomy of Coupled Constitutive Models for Ratcheting Simulation", *International Journal of Plasticity*, Vol. 16, pp. 381-409.

[7] Bauschinger, J., 1881. "Ueber die Veraenderung der Elasticitaetgenze und des Elasticitaetmodulus Verschiedener Metalle", *Civilingeneur*, Vol. 27, pp. 289–348.

[8] Prager, W., 1956. "A New Method of Analyzing Stresses and Strains in Work Hardening Plastic Solids", *Journal of Applied Mechanics*, ASME, Vol. 23, pp. 493–496.

[9] Armstrong, P.J., Frederick, C.O., 1966. "A Mathematical Representation of the Multiaxial Bauschinger Effect", *CEGB Report No. RD/B/N* 731.

[10] Guionnet, C., 1992. "Modeling of Ratcheting in Biaxial Experiments", *Journal of Engineering Materials and Technology*, ASME, Vol. 114, pp. 56-62.

[11] Chaboche, J.L., 1986. "Time-Independent Constitutive Theories for Cyclic Plasticity", *International Journal of Plasticity*, Vol. 2, pp. 149-188.

[12] Chaboche, J.L., Dang-Van, K., Cordier, G., 1979. "Modelization of the strain memory effect on the cyclic hardening of 316 stainless steel", *Proceedings of the 5th International Conference on SMiRT*, Div. L, Berlin, Germany.

[13] Chaboche, J.L., 1991. "On some modifications of kinematic hardening to improve the description of ratcheting effects", *International Journal of Plasticity,* Vol. 7, pp.661-678.

[14] Chaboche, J.L., 1994. "Modeling of Ratcheting: Evaluation of Various Approaches", *European Journal of Mechanics, A/Solids*, Vol. 13, pp. 501-518.

[15] Ohno, N., Wang, J.-D., 1993. "Kinematic Hardening Rules with Critical State of Dynamic Recovery, part I and II", *International Journal of Plasticity*, Vol. 9, pp. 375-403.

[16] Hassan, T., Rahman, M., 2015. "Constitutive Models in Simulating Low-Cycle Fatigue and Ratcheting Responses of Elbow", *Journal of Pressure Vessel Technology*, ASME, Vol 137, pp. 031002-1-12.

[17] Islam, N., Hassan, T., 2016, "Improving Simulations for Low Cycle Fatigue and Ratcheting Responses of Elbows", *Proceedings of the ASME 2016 Pressure Vessels and Piping Conference*, PVP2016-63353, Vancouver, British Columbia, Canada.

[18] Dafalias,Y.F., Kourousis, K.I., Saridis, G.J., 2008. "Multiplicative AF Kinematic Hardening in Plasticity", *Int J Solids Structures*, Vol 45 pp. 2861–80.

[19] Agius, D., Kourousis, K.I., Wallbrink, C., 2018. "A Modification of the Multicomponent Armstrong–Frederick Model with Multiplier for the Enhanced Simulation of Aerospace Aluminium Elastoplasticity", *International Journal of Mechanical Sciences*, Vol 144 pp. 118-133.

[20] Ucak, A. Tsopelas, P., 2011. "Constitutive Model for Cyclic Response of Structural Steels with Yield Plateau", *Journal of Structural Engineering, ASCE*, pp. 195-206.

[21] Ucak, A. Tsopelas, P., 2012. "Accurate Modeling of the Cyclic Response of Structural Components Constructed of Steel with Yield Plateau", *Journal of Structural Engineering, ASCE*, Vol 35, pp. 195-206.

[22] Chatzopoulou, G., Karamanos, S.A., Varelis, G. E., 2016. "Finite Element Analysis of UOE Manufacturing Process and its Effect on Mechanical Behavior of Offshore Pipes", *International Journal of Solids and Structures*, Vol. 83, pp. 13-27.

[23] Hu, F.X., Shi, G., Shi, Y.J., 2018. "Constitutive Model for Full-Range Elasto-Plastic Behavior of Structural Steels with Yield Plateau: Formulation and Implementation", *Eng. Structutres*, Vol.71, pp. 1059–1070.

[24] Hu, F.X., Shi, G., Shi, Y.J., 2016. "Constitutive Model for Full-Range Elasto-Plastic Behavior of Structural Steels with Yield Plateau: Calibration and Validation", *Eng. Structutres*, Vol.118, pp. 210-227.

[25] Lee, C.H., Chang, K.H., Do, B.N.V., 2016. "Numerical Investigation on the Ratcheting Behavior of Pressurized Stainless Steel Pipes under Cyclic in-Plane Bending", *Marine Structures*, Vol.49, pp. 224-238.

[26] Burlet H, Cailletaud G., 1986. "Numerical techniques for cyclic plasticity at variable temperature". *Eng Comput*; Vol:3 pp. 143-153.

[27] Rahmatfam, A., Zehsaz, M., Chakherlou, T.N., 2019. "Ratcheting Assessment of Pressurized Pipelines under Cyclic Axial Loading: Experimental and Numerical Investigations", *International Journal of Pressure Vessels and Piping*, Vol.176, pp. 1-9.

[28] Foroutan, M., Ahmadzadeh, G.R, Varvani-Farahani, A., 2018. "Axial and Hoop Ratcheting Assessment in Pressurized Steel Elbow Pipes Subjected to Bending Cycles*", Thin-Walled Structures*, Vol.123, pp. 317-323.

[29] Ahmadzadeh, G.R. Varvani-Farahani, A., 2016. "A Kinematic hardening rule to investigate the impact of loading path and direction on ratcheting response of Steel Alloys", *Mech. Mater.* Vol. 101, pp. 40–49.

[30] Mroz, Z., 1967. "On the Description of Anisotropic Work Hardening", *Journal of the Mechanics and Physics of Solids*, Vol. 15, pp. 163-175.

[31] Iwan, W. D., "On a Class of Models for the Yielding Behavior of Continuous and Composite Systems", *Journal of Applied Mechanics*, ASME, Vol. 34, 1967, pp. 612-617.

[32] Bari, S., Hassan, T., 2001. "Kinematic Hardening Rules in Uncoupled Modeling for Multiaxial Ratcheting Simulation", *International Journal of Plasticity*, Vol. 17, pp. 885-905.

[33] Dafalias, Y.F., Popov, E.P., 1976. "Plastic Internal Variables Formalism of Cyclic Plasticity", *Journal of Applied Mechanics*, ASME, Vol. 43, pp. 645-650.

[34] Krieg, R.D., 1975. "A Practical Two-Surface Plasticity Theory", *Journal of Applied Mechanics*, ASME, Vol. 42, pp. 641–646.

[35] Drucker, D.C., Palgen, L., 1981. "On Stress-Strain Relations Suitable for Cyclic and Other Loadings", *Journal of Applied Mechanics*, ASME, Vol. 48, pp. 479-485.

[36] Tseng, N.T., Lee, G.C., 1983. "Simple Plasticity Model of the Two-Surface Type", *Journal of Engineering Mechanics*, ASCE, Vol. 109, pp. 795-810.

[37] Shen, C., Tanaka, Y., Mizuno, E., Usami, T., 1992. "A Two-Surface Model for Steels with Yield Plateau", *Structural Eng./Earthquake Eng.*, Vol. 8, No.4, pp.179-188.

[38] Shen, C., Mamaghani, I.H.P., Mizuno, E., Usami, T., 1995. "Cyclic behavior of structural steels II: Theory", *Journal of Engineering Mechanics,* Vol. 121, pp.1165-1172.

[39] Hassan, T., Corona, E., Kyriakides, S., 1992a. "Ratcheting in Cyclic Plasticity, Part II Multiaxial Behavior", *International Journal of Plasticity*, Vol. 8, pp. 117-146.

[40] Hassan, T., Kyriakides, S., 1994a. "Ratcheting of Cyclically Hardening and Softening Materials, Part I uniaxial behavior", *International Journal of Plasticity*, Vol. 10, pp. 149-184.

[41] Hassan, T., Kyriakides, S., 1994b. "Ratcheting of Cyclically Hardening and Softening Materials, Part II: multiaxial behavior", *International Journal of Plasticity*, Vol. 10, pp. 185-212.

[42] Andrianopoulos, K.I, Papadimitriou, A.G., Bouckovalas, G.D.,2010. "Explicit Integration of Bounding Surface Model for the Analysis of Earthquake Soil Liquefaction", *International Journal for Numerical and Analytical Methods in Geomechanics*, Vol. 34, pp. 1586–1614.

[43] Papadimitriou, A.G., Chaloulos, Y.K., Dafalias, Y.F., 2018. "A Fabric-Based Sand Plasticity Model with Reversal Surfaces Within Anisotropic Critical State Theory", *Acta Geotechnica*, pp. 1-25.

[44] Doghri, I., 1999. "Fully implicit integration and consistent tangent modulus in elasto-plasticity", *International Journal for Numerical Methods in Engineering*, Vol. 36, pp. 3915-3932.

[45] Sawyer, J. P. G., Wang, C. H., Jones, R., 2001. "An Implicit Algorithm Using Explicit Correctors for the Kinematic Hardening Model with Multiple Back Stresses", *International Journal for Numerical Methods in Engineering*, Vol. 50, pp. 2093-2107.

[46] ABAQUS. Simulia, Abaqus Theory Guide, Version 6.14, Dassault Systèmes, 2014.

[47] ANSYS Academic Research Mechanical, Release 18.1

[48] Montans, F.J., 2000. "Implicit Algorithms for Multilayer J2-Plasticity", *Computer Methods in Applied Mechanics and Engineering,* Vol. 189, pp.673 –700.

[49] Montans, F.J. 2001. "Implicit multilayer J2-plasticity using Prager's translation rule", *International Journal for Numerical Methods in Engineering*; Vol. 50, pp. 347–376.

[50] Montans, F.J., Caminero, M.A., 2007. "On the Consistency of Nested Surfaces Models and their Kinematic Hardening Rules", *International Journal of Solids and Structures*, Vol. 44, pp. 5027-5042.

[51] Khoei, A.R., Jamali, N., 2005. "On the Implementation of a Multisurface Kinematic Hardening Plasticity and its Applications", *International Journal of Plasticity*, Vol. 21, pp. 1741–1770.

[52] Varelis, G.E., 2013. "Numerical Simulation of Steel Member Response Under Strong Cyclic Loading" PhD. Thesis, University of Thessaly, Greece.

[53] Varelis, G. E., Karamanos, S. A., and Gresnigt, A. M., 2013, "Steel Elbow Response Under Strong Cyclic Loading.", *Journal of Pressure Vessel Technology*, ASME, Vol. 135, No.1, Article Number: 011207.

[54] Varelis, G. E., and Karamanos, S. A., 2015, "Low-Cycle Fatigue of Pressurized Steel Elbows Under In-Plane Bending.", *Journal of Pressure Vessel Technology*, ASME, *Vol.* 137, No.1, Article Number: 011401.

[55] Seyed-Ranjbari, M., 1986. "Further Development, Multiaxial Formulation, and Implementation of the Bounding Surface Plasticity Model for Metals", Ph.D. dissertation, University of California, Davis.

[56] Bursi, O. S. *et al.*, 2012. "Design and Integrity Assessment of High-Strength Tubular Structures for Extreme Loading Conditions", *Final report, HITUBES RFCS project,* European Commission, Brussels, Belgium (also available in http://bookshop.europa.eu).

[57] Pappa, P. *et al.*, 2013. "Structural Safety of Industrial Steel Tanks, Pressure Vessels and Piping Systems under Seismic loading", *Final report, INDUSE RFCS project,* European Commission, Brussels, Belgium (also available in http://bookshop.europa.eu).

[58] Rodabaugh, E. C. and George, H. H., 1957, "Effect of Internal Pressure on the Flexibility and Stress Intensification Factors of Curved Pipe or Welding Elbows.", *Transactions of the ASME*, Vol. 79, pp. 939-948

[59] Dodge, W. G. and Moore, S. E., 1972. "Stress Indices and Flexibility Factors for Moment Loadings on Elbows and Curved Pipe". Oak Ridge National Lab, ORNL-TM-3658, Tennessee.

[60] American Society of Mechanical Engineers, 2010a, *Power Piping*, B31.1, ASME Code for Pressure Piping, New York, NY.

[61] American Society of Mechanical Engineers, 2010b, *Process Piping*, B31.3, ASME Code for Pressure Piping, New York, NY.

[62] Suzuki, K., 2006. "Earthquake Damage to Industrial Facilities and Development of Seismic Vibration Control Technology–Based on Experience from the 1995 Kobe Earthquake", *Journal of Disaster Research*, Vol. 1, No.2.

[63] Paolacci, F., Reza, M. S., Bursi, O. S., 2011. "Seismic Design Criteria of Refinery Piping Systems", *Conference on Computational Methods in Structural Dynamics and Earthquake Engineering*, COMPDYN, Corfu, Greece.

[64] Karamanos, S.A., 2016. "Mechanical Behavior of Steel Pipe Bends: An Overview", *J. Pressure Vessel Technology*, Vol. 138(4), pp 04120315-1-15.

[65] Gresnigt, A. M., 1986, "Plastic Design of Buried Steel Pipelines in Settlement Areas," *Heron*, Vol. 31(4), pp. 3–113.

[66] Tan, Y., Matzen, V. C., and Yu, L. X., 2002, "Correlation of Test and FEA Results for the Nonlinear Behavior of Straight Pipes and Elbows", *Journal of Pressure Vessel Technology*, Vol. 124, pp. 465–475.

[67] Karamanos, S. A., Tsouvalas, D., and Gresnigt, A. M., 2006., "Ultimate Bending Capacity and Buckling of Pressurized 90 Deg Steel Elbows", *Journal of Pressure Vessel Technology*, Vol. 128(3), pp. 348–356.

[68] Balan, C. and Redektop, D., 2005. "The Effect of Bidirectional Loading on Fatigue Assessment of Pressurized Piping Elbows with Local Thinned Areas*", International Journal of Pressure Vessels and Piping*, Vol. 81, pp. 235-242.

[69] Beaney, E. M., 1989. "Plasticity on Resonant Pipework Vibration", *Proceedings of International Conference on Pipework Engineering and Operation,* I.Mech.E, C376/002, pp. 281-290.

[70] Beaney, E. M., 1991. "Measurement of Dynamic Response and Failure of Pipework", *Strain*, pp. 89-94.

[71] Moreton, D.N., Yahiaoui, K., Moffat, D.G., 1996. "Onset of Ratchetting in Pressurized Piping Elbows Subjected to In-Plane Bending Moments", *International Journal of Pressure Vessel and Piping*, Vol. 68, No. 1, pp. 73-79.

[72] Yahiaoui, K., Moffat, D.G., Moreton, D.N., 1996. "Response and Cyclic Strain Accumulation of Pressurized Piping Elbows Under Dynamic In-Plane Bending", *Journal of Strain Analysis for Engineering Design*, Vol. 31 (2), pp. 135-151.

[73] Slagis, G. C., 1997. "Evaluation of Seismic Response Data for Piping, W*elding Research Council*, Bulletin No. 423, pp. 1-162

[74] Slagis, G. C., 1998, "Experimental Data on Seismic Response of Piping Components," *Journal of Pressure Vessel Technol.*, Vol. 120(4), pp. 449–455.

[75] Fujita, K., Shiraki, K., Kitaide, K., and Nakamura, T., 1978, "Vibration Damage Experiment of the Curved Pipes (Elbows) Relating to Seismic Ultimate Strength," *Trans. Jpn. Soc. Mech. Eng.*, Vol. 44(386), pp. 3437–3445 (in Japanese).

[76] Fujiwaka, T., Endou, R., Furukawa, S., Ono, S., and Oketani, K., 1999, "Study on Strength of Piping Components Under Elastic-Plastic Behavior Due to Seismic Loading," *ASME PVP conference*, 387, pp. 19–25.

[77] Yoshino, K., Endou, R., Sakaida, T., Yokota, H., Fujiwaka, T., Asada, Y., and Suzuki, K., 2000. "Study on Seismic Design of Nuclear Power Plant Piping in Japan—Part 3: Component Test Results", *ASME PVP conference*, Vol. 407, pp. 131–137.

[78] DeGrassi, G., Hofmayer, C., Murphy, A., Suzuki, K., and Namita, Y., 2003. "BNL Nonlinear Pre-Test Seismic Analysis for the NUPEC Ultimate Strength Piping Test Program," T*ransactions of the 17th International Conference on SMiRT*, Prague, Czech Republic, Paper K25.

[79] Suzuki, K., Namita, Y., Abe, H., Ichihashi I., Suzuki K., Sakakida T., Sato T., Yokota, H., 2003. "Seismic Proving Test of Ultimate Piping Strength", Transactions of the 17th International Conference on Structural Mechanics in Reactor Technology (SMiRT 17) *Conference*.

[80] Chen, X., Gao, B., Chen, G., 2006. "Ratcheting Study of Pressurized Elbows Subjected to Reversed In-Plane Bending", *Journal of Pressure Vessel Technology*, Vol. 128, pp 525-532.

[81] Hassan, T., Rahman, S. M., and Bari, S., 2015. "Low-Cycle Fatigue and Ratcheting Responses of Elbow Piping Components", *International Journal of Pressure Vessels and Piping*, Vol 137, pp.031010-1-12.

[82] Nakamura, I., Kasahara, N., 2017. "Excitation Tests on Elbow Pipe Specimens to Investigate Failure Behavior Under Excessive Seismic Loads", *Journal of Pressure Vessel Technology*, Vol. 139, pp 061802-1-11.

[83] Ravi Kiran, A., Reddy, G. R., Dubey, P. N. and Agrawal, M. K., 2017. "Fatigue-Ratcheting Behavior of 6 in Pressurized Carbon Steel Piping Systems Under Seismic Load: Experiments and Analysis". *Journal of Pressure Vessel Technology*, Vol. 139, Article No. 061801.

[84] Ravi Kiran, A., Reddy, G. R., Agrawal, M. K., 2018. "Experimental and Numerical Studies of Inelastic Behavior of Thin Walled Elbow and Tee Joint Under Seismic Load", *Thin-Walled Structures*, Vol. 127, pp. 700–709.

[85] Labbé P., B., Reddy, G., R., Mathon, C., Moreau, F., Karamanos, S., A., 2016. "The OECD-NEA Programme On Metallic Component Margins Under High Seismic Loads (MECOS)", Proceedings of the ASME 2016 Pressure Vessels and Piping Conference, PVP2016- 63119, Vancouver, British Columbia, Canada.

[86] Sollogoub P., 2016. "The OECD-NEA Programme On Metallic Component Margins Under High Seismic Loads (MECOS): Towards New Criteria", Proceedings of the ASME 2016 Pressure Vessels and Piping Conference, PVP2017-6551, Waikoloa, Hawaii, USA.

[87] Chaboche, J. L., 1989, "Constitutive Equations for Cyclic Plasticity and Cyclic Viscoplasticity," *International Journal of Plasticity*, Vol. 5(3), pp. 247–302.

[88] Abdel-Karim, M., and Ohno, N., 2000, "Kinematic Hardening Model Suitable for Ratchetting with Steady-State," *International Journal of Plasticity*, Vol. 16(3–4), pp. 225–240.

[89] Chen, X., and Jiao, R., 2004, "Modified Kinematic Hardening Rule for Multiaxial Ratcheting Prediction," *International Journal of Plasticity*, Vol. 20(4–5), pp. 871–898.

[90] American Society of Mechanical Engineers, 2007, *Factory-Made Wrought Butt-welding Fittings*, B16.9, ASME Code for Pressure Piping, New York, NY.

[91] Karvelas, C., Stathas, N., Strepelias, E., Palios, X., Chatzopoulou, G., Bousias, S., Karamanos S. A., 2019., "Strong Cyclic Loading of an Industrial Piping System", *2nd International Conference on Natural Hazards & Infrastructure*, ICONHIC 2019, Chania, Crete, Greece.

[92] Maddox, S. J., (2018). "Status Review on Fatigue Performance of Fillet Welds", *Journal of Offshore Mechanics and Arctic Engineering,* ASME, Vol. 130, pp. 031006-1-10.

[93] Schjødt-Thomsen J., Andreasen, J. H., (2018). "Low Cycle Fatigue Behaviour of Welded T-Joints in High Strength Steel", *Engineering Failure Analysis*, Vol. 93, pp. 38-43.

[94] Corigliano, P., Crupi, V., Fricke, W., Friedrich, N., Guglielmino, E., (2015). "Experimental and numerical analysis of fillet-welded joints under low-cycle fatigue loading by means of full-field techniques", *Journal of Mechanical Engineering Science,* Vol. 229 (7), pp. 1327–1338.

[95] Corigliano, P., Crupi, V., Fricke, W., Guglielmino, E., (2015). "Low-Cycle Fatigue Life Prediction of Fillet-Welded Joints In Ship Details", *18th International Conference on Ships and Shipping Research,* Lecco, Italy.

[96] Peek, R. (1988). "Analysis of unanchored liquid storage tanks under lateral loads", *Earthquake Engineering and Structural Dynamics*, Vol 16, No. 7, pp. 1087-1100

[97] Natsiavas, S., Babcock, C.D. (1988). "Behavior of unanchored fluid-filled tanks subjected to ground excitation", *Journal of Applied Mechanics*, ASME, Vol. 55, No. 3, pp. 654-659.

[98] Wozniak, R. S. and Mitchell, W. W., (1978). "Basis of seismic design provisions for welded steel oil storage tanks", *Session on Advances in Storage Tank Design*, API 43rd mid-year meeting, Toronto, Canada.

[99] Leon, G. S., and Kausel, E. A. M., (1986). "Seismic analysis of fluid storage tanks," *Journal of Structural Engineering*, ASCE, Vol. 112 (1), pp. 1-18.

[100] Fischer, F. D., Rammerstorfer, F. G., Schreiner, W., (1989). "The extensible uplifted strip", *Acta Mechanica,* Vol. 80, pp 227–257.

[101] Malhotra, P. K., and Veletsos, A. S., (1994). "Beam Model for Base-uplifting Analysis of Cylindrical Tanks," *Journal of Structural Engineering,* ASCE, Vol. 120, No. 12, pp. 3471-3488.

[102] Malhotra & Veletsos 1 Malhotra, P. K., and Veletsos, A. S., (1994). "Uplifting Analysis of base plates in cylindrical tanks," *Journal of Structural Engineering*, ASCE, Vol. 120, No. 12, pp. 3489-3505.

[103] Malhotra & Veletsos 2 Malhotra, P.K., and Veletsos, A. S., (1994). "Uplifting Response of Unanchored Liquid-Storage Tanks," *Journal of Structural Engineering*, ASCE, Vol. 120, No. 12, pp. 3525-3547.

[104] Bohra, H., Azzuni, E., Guzey, S., (2019). "Seismic Analysis of Open-Top Storage Tanks with Flexible Foundation, *Journal of Pressure Vessel Technology*, ASME, Vol. 141, pp. 041801-1-15.

[105] Spritzer, J.M., Guzey, S., (2017). "Nonlinear Numerical Evaluation of Large Open-Top Aboveground Steel Welded Liquid Storage Tanks Excited by Seismic Loads, *Thin-Walled Structures*, Vol. 119, pp. 662–676.

[106] Taniguchi, T., Yoshida, Y., Hatayama, K., (2018). "Applicability of the Simplified Analysis and Relevant Calculations to Evaluating Uplift Displacement of Unanchored Tanks", *Proceedings of the Pressure Vessels and Piping Conference*, ASME, Prague, Czech Republic.

[107] Cortes G, Nussbaumer A, Berger C, Lattion E. (2011). "Experimental determination of the rotational capacity of wall-to-base connections in storage tanks", *Journal of Constructional Steel Research*, Vol. 67, pp. 1174–84.

[108] EN1998-4 (2006). *Eurocode 8: Design of structures for earthquake resistance, part 4: Silos, Tanks and Pipe lines*. European Committee for Standardization, Brussels, Belgium.

[109] NZSEE (2009). *Seismic Design of Storage Tanks* New Zealand National Society for Earthquake Engineering; Wellington, New Zealand

[110] Prinz, G. S., Nussbaumer, A., (2012). "Fatigue analysis of liquid-storage tank shell-to-base connections under multi-axial loading", *Eng. Struct.* Vol. 40, No. 7, pp. 75–82.

[111] Prinz, G. S., Nussbaumer, A. (2012). "On the low-cycle fatigue capacity of unanchored steel liquid storage tank steel-to-base connections", *Bulletin of Earthquake Engineering,* Vol. 10, No. 6, pp. 1943–1958.

[112] Prinz, G. S., Nussbaumer, A. (2014). "Effect of radial base-plate welds on ULCF capacity of unanchored tank connections", *Journal of Constructional Steel Research*, Vol. 103, pp. 131-139.

[113] Vathi, M., Karamanos, S, A., (2017), "A simple and efficient model for seismic response and low-cycle fatigue assessment of uplifting liquid storage tanks", *Journal of Loss Prevention in the Process Industries*, Vol. 53, pp. 29-44.

[114] EN 1993-1-10 (2005). Eurocode 3-Design of steel structures, Part 1-10: Material toughness and through-thickness properties, European Committee for Standardization, Brussels, Belgium.

[115] EN 14015 (2004). Specification for the design and manufacture of site built, vertical, cylindrical, flat-bottomed, above ground, welded, steel tanks for the storage of liquids at ambient temperature and above, European Committee for Standardization, Brussels, Belgium.

[116] Bursi, O. S. *et al.* (2019). Component fragility evaluation and seismic safety assessment of "special risk" petrochemical plants under design basis and beyond design basis accidents, Final report, INDUSE-2-SAFETY RFCS project, European Commission, Brussels, Belgium (also available in http://bookshop.europa.eu).

[117] EN 1043-1 (1996). Destructive tests on welds in metallic materials- Hardness testing -Part 1: Hardness test on arc welded joints European Committee for Standardization, Brussels, Belgium.